The role of temperature in processes controlling weathering rates of carbonate lithologies and volcanic systems

Dissertation
zur Erlangung des Doktorgrades der Naturwissenschaften
an der Fakultät für Mathematik, Informatik und Naturwissenschaften
Fachbereich Geowissenschaften
der Universität Hamburg

vorgelegt von
Gibran Romero Mujalli
Aus
San Felix, Venezuela

Hamburg, 2019

Accepted as Dissertation at the Department of Earth Sciences

Day of oral defence:	30.04.2019
Reviewers	Prof. Dr. Jens Hartmann Dr. Thorben Amann
Chair of the Subject Doctoral Committee	Prof. Dr. Dirk Gajewski
Dean of Faculty of MIN:	Prof. Dr. Heinrich Graener

Table of Contents

Summary

The chemical weathering is a natural mechanism that releases nutrients from minerals and consumes CO_2 through the process. Two main lithological classes that have the highest observed weathering fluxes on Earth, carbonate and volcanic rocks, represent important components in the carbon cycle. Carbonate rocks, one of the main C reservoir in Earth's upper terrestrial lithosphere, weather relatively fast and have a rapid response to climate change. On the other hand, volcanoes, besides representing an important natural CO_2 emission to the atmosphere, present the highest natural silicate weathering fluxes in Earth. Weathering processes in Earth System Models are often scaled with runoff relationships or the Arrhenius equation for chemical kinetics. However, other mechanisms that might be relevant for controlling weathering rates are neglected at the global scale. The aim of this work is to explore processes, previously neglected, that can control global weathering rates in carbonate lithologies and volcanic systems: (i) the role of temperature on controlling global weathering rates of carbonate minerals; and, (ii) the role of elevated temperature processes beneath volcanic areas in total weathering fluxes. Global spring and river water datasets draining carbonate lithologies are studied to understand the influence of temperature and soil CO_2 on carbonate weathering intensity and achieve a better weathering rate estimation at the global scale, with focus on calcite-carbonate sedimentary rocks. Results show that carbonate weathering at global scale can be quantified implementing thermodynamic equations and considering the partial pressure of CO_2 in the soil profile, where the deepening of the weathering front in carbonate lithologies, mostly located in tropical regions, reduces the weathering rates significantly. Furthermore, to address the hydrothermal contribution to weathering fluxes, natural waters from Aso caldera, one of the most actives volcanoes in Japan, are analysed to quantify mixing processes with volcanic gases by determining stable isotopes of carbon and sulphur and applying Se:S molar ratios. The latter represents a new parameter to distinguish mixing between sulphate from deep fluids and sulphate from water percolating soils. Approximately half of the total observed weathering rates from Aso caldera is found to be related to dissolution of primary minerals with strong acids (mainly sulphuric acid) of magmatic origin, suggesting that dissolution of minerals below the volcanic crater is a relevant process influencing regional weathering rates. The hydrothermal input on surface waters, however, is not constant over time, making global calculations difficult because the migration of deep fluids is different for each system. Weathering rates from volcanic systems is not equivalent to atmospheric CO_2 consumption because, generally, the magmatic CO_2 and SO_2 mixed in the groundwater are not accounted in the biogeochemical budgets. The results of this thesis showed that temperature, hydrology and production of acid are the main factors controlling weathering intensity in both systems. Temperature, besides its relevance describing climatic conditions, exerts the most important control on weathering processes because it influences directly the thermodynamic and kinetics of the reaction and controls soil respiration, one of the most important mechanism for production of acid in the soil profile. Future studies should consider the amount of weathering rate that is influenced by sulphuric acid, because it can unbalance the carbon cycle reducing the amount of CO_2 that is consumed through weathering reactions.

Zusammenfassung

Die chemische Verwitterung von Gesteinen ist ein natürlicher Mechanismus, der chemische Elemente aus Mineralen löst und CO_2 durch den Prozess bindet. Die zwei wichtigsten Gesteinsarten, die die höchsten beobachteten Verwitterungsflüsse auf der Erde aufweisen, sind Karbonat- und Vulkangesteine, die gleichzeitig wichtige Bestandteile des Kohlenstoffkreislaufs sind. Karbonatgesteine, eins der größten Kohlenstoffreservoire in der oberen terrestrischen Lithosphäre der Erde, lösen sich relativ schnell auf und reagieren schnell auf Klimaveränderungen. Gleichzeitig weisen Vulkangebiete, abgesehen von einem wichtigen natürlichen CO_2-Ausstoß in die Atmosphäre, die höchsten natürlichen Silikatverwitterungsraten auf der Erde auf. In Erdsystemmodellen werden Verwitterungsprozesse häufig mit Wasserabfluss oder der Arrhenius-Gleichung für die chemische Kinetik skaliert. Andere Mechanismen, die für die Reaktionsgeschwindigkeit relevant sein könnten, werden jedoch auf globaler Skala vernachlässigt. Das Ziel dieser Arbeit ist es, weitere bisher vernachlässigte Prozesse zu erforschen, die die globalen Verwitterungsflüsse von Karbonatischen und vulkanischen Einzugsgebieten steuern können: (i) die Rolle der Temperatur bei der Kontrolle der globalen Verwitterungsgeschwindigkeit von Karbonatmineralen bewerten; und (ii) die Rolle von Prozessen bei erhöhten Temperaturen unter vulkanischen Oberflächen und den Beitrag zu Gesamtverwitterungsflüssen. Globale Quell- und Flusswasser-Datensätze aus karbonatischen Einzugsgebieten werden untersucht, um den Einfluss von Temperatur und Boden-CO_2 auf die Verwitterungsintensität von Karbonaten zu verstehen und eine bessere Abschätzung der Verwitterungsgeschwindigkeit auf globaler Ebene zu erreichen, wobei der Schwerpunkt auf Sedimentgesteinen aus Calcit liegt. Auf globaler Ebene kann die Karbonatverwitterungsraten bestimmt werden, in dem thermodynamische Gleichungen angewendet werden und unter Berücksichtigung des CO_2-Partialdrucks im Bodenprofil, in welchem die Tiefenverlagerung der Verwitterungsfront in Karbonatlithologien, hauptsächlich in tropischen Gebieten, die Verwitterungsraten signifikant reduziert. Um den hydrothermalen Einfluss auf Verwitterungsflüsse zu betrachten, werden natürliche Wässer der Aso-Kaldera, einem der aktivsten Vulkane in Japan, analysiert, um Mischungsprozesse mit vulkanischen Gasen zu quantifizieren unter Berücksichtigung der stabilen Kohlenstoff- und Schwefel-Isotope und des Se:S-Verhältnisses. Letzteres stellt einen neuen Parameter dar, um die Vermischung von Sulfaten aus Tiefenwässern und Sulfaten aus Bodenwässern zu unterscheiden. Ungefähr die Hälfte der gesamten berechneten Verwitterungsraten des Einzugsgebietes der Aso-Kaldera könnten das Ergebnis der Auflösung von Primärmineralen durch starke Säuren magmatischer Herkunft (hauptsächlich Schwefelsäure) sein, was die Wichtigkeit dieses Prozesses unter dem Vulkankrater für regionale Verwitterungsraten verdeutlicht. Der hydrothermale Einfluss auf Oberflächenwässer ist jedoch nicht zeitlich konstant, was globale Berechnungen erschwert, da die Migration von Tiefenwässern in jedem System unterschiedlich ist. Außerdem sind die Verwitterungsraten von vulkanischen Gebieten nicht gleichzusetzen mit atmosphärischem CO_2-Konsum, da in der Regel das magmatische CO_2 und SO_2, welche sich in vulkanischen Gebieten im Grundwasser befinden, nicht im atmosphärischen Budget berücksichtigt werden. Die Ergebnisse zeigen, dass die Temperatur, die Hydrologie und die Produktion von Säuren die Hauptfaktoren bilden, die die Verwitterungsintensität sowohl in karbonatischen als auch Systemen kontrollieren. Die Temperatur stellt den wichtigsten Kontrollfaktor für Verwitterungsprozesse dar, da sie direkt die Reaktions-Thermodynamik und -kinetik beeinflusst und Respiration im Boden kontrolliert, einer der wichtigsten Mechanismen für die Säureproduktion im Boden. Zukünftige Studien sollten den Anteil an Verwitterungsraten, der von Schwefelsäure beeinflusst wird, berücksichtigen, weil der Kohlenstoffkreislauf nicht länger im Gleichgewicht ist, da sich der Anteil von CO_2, welcher durch Verwitterungsreaktionen gebunden wird, verringert.

List of Publications

The author of this thesis has published chapter 2 and 3 in peer-review journals, while chapter 4 was prepared to be submitted. Moreover, the author has also contributed in other publications during its doctoral studies. The publications are listed below and the author's individual contribution to the publications are described in Appendix E.

Manuscripts accepted for publication

Romero-Mujalli, G., Hartmann, J., Börker, J., Gaillardet, J. & Calmels, D., 2018. Ecosystem controlled soil-rock $p\text{CO}_2$ and carbonate weathering – Constraints by temperature and soil water content. Chemical Geology. (Chapter 2 of this thesis).

Romero-Mujalli, G., Hartmann, J. & Börker, J., 2018. Temperature and CO_2 dependency of global carbonate weathering fluxes – Implications for future carbonate weathering research. Chemical Geology. (Chapter 3 of this thesis).

Börker, J., Hartmann, J., **Romero-Mujalli, G.** & Amann, T., 2018. Terrestrial Sediments of the Earth: Development of a Global Unconsolidated Sediments Map Database (GUM). Geochemistry, Geophysics, Geosystems.

Gaillardet, J., Calmels, D., **Romero-Mujalli, G.**, Zakharova, E. & Hartmann, J., 2018. Global climate control on carbonate weathering intensity. Chemical Geology.

Börker, J., Hartmann, J., **Romero-Mujalli, G.** & Li, G., 2018. Short Communication: Aging of basalt volcanic systems and decreasing CO2 consumption by weathering. E-Surf.

Manuscripts in preparation

Romero-Mujalli, G., Hartmann, J., Hosono, T., Amann, T., Louvat, P. and Böttcher, M.E., Evaluating the contribution of high temperature fluids to surface waters using Se:SO_4^{2-} molar ratios for the Aso caldera, Japan: Implications for weathering rates of volcanic areas. (Chapter 4 of this thesis).

Chapter 1: Introduction

The carbon cycle, one of the main biogeochemical cycles in Earth system, is being significantly altered by anthropogenic emissions, which leads to relevant changes in Earth's climate according to model predictions (Friedlingstein et al., 2006; Cox et al., 2000). Most of the models, however, do not agree with intensity change because it is difficult to quantify with relatively low uncertainty (Friedlingstein et al., 2006). A clear understanding of the global carbon cycle is, therefore, imperative in predicting accurately the anthropogenic effect on Earth's climate.

The weathering process, representing physical and chemical transformation of rocks and primary minerals in the Earth's surface, is a key component in the carbon cycle, mainly because its products, which are transported to the ocean, are considered in global biogeochemical budgets (Hartmann et al., 2014b; Beusen et al., 2009; White et al., 1998; Berner et al., 1983; Lerman et al., 1975). Moreover, the chemical weathering of minerals in soils involves a reaction with CO_2, hence this process is considered as a natural sink of atmospheric CO_2 (Berner et al., 1983; Walker et al., 1981; Kempe, 1979; Mackenzie and Garrels, 1966). Although it has been extensively studied and proofed that continental weathering strongly depends on environmental parameters, such as temperature, hydrology, geomorphology and vegetation (Norton et al., 2014; Egli et al., 2008; White and Blum, 1995), global weathering rates might had been constant during glacial-interglacial scales (Von Blanckenburg et al., 2015; Foster and Vance, 2006). In the long-term global carbon cycle (i.e. longer than one million years), however, the role of silicate weathering in decreasing atmospheric CO_2 concentration is assumed to be the main control on atmospheric CO_2 and, as a consequence, Earth's climate (Li et al., 2009; Berner et al., 1983). A general silicate chemical weathering process can be represented by the following example dissolution of forsterite:

$$Mg_2SiO_{4(m)} + 4CO_{2(g)} + 4H_2O_{(l)} \rightarrow 2Mg^{2+}_{(aq)} + 4HCO^{-}_{3(aq)} + H_4SiO_{4(aq)} \qquad (1.1)$$

This process produces Mg and hydrogen carbonate ions dissolved in water. In the long-term cycle, these products are transported by continental waters to the ocean, where precipitation of carbonate minerals produces CO_2 by the following summarized chemical equation:

$$Mg^{2+}_{(aq)} + 2HCO^{-}_{3(aq)} \rightarrow MgCO_{3(m)} + CO_{2(g)} + H_2O_{(l)} \qquad (1.2)$$

The balance between Eq. 1.1 and 1.2 results in a net CO_2 consumption of 2 moles per mole of mineral. In the short-term carbon cycle (time scale less than 100 thousand years), the influence of both weathering of silicate and carbonate minerals is relevant (Berner and Berner, 2012). Carbonate minerals, mainly calcite ($CaCO_{3(m)}$), can be dissolved faster than silicate minerals and also consume atmospheric CO_2. Nevertheless, the dissolution of calcite is neglected in long-term calculations due to the precipitation of these minerals in the ocean, releasing CO_2 to the atmosphere (Berner et al., 1983). The summarized calcite dissolution-precipitation chemical equation is as follows:

$$CaCO_{3(m)} + CO_{2(g)} + H_2O_{(l)} \leftrightarrow Ca^{2+}_{(aq)} + 2HCO^{-}_{3(aq)} \tag{1.3}$$

where the reaction in the direction to the reactants is the precipitation in the ocean (similar than Eq. 1.2) and the reaction in the direction to the products is the dissolution of calcite.

1.1 Weathering rates calculations and limitations

The chemical composition of continental waters carries information about weathering rates for the specific hydrological catchment, and global carbon budgets of carbonate and silicate weathering can be estimated applying mass balance to global riverine data (Gaillardet et al., 1999). Furthermore, the lithological influence on weathering fluxes can be determined by analysing waters draining a single lithological type (Hartmann et al., 2009; Bluth and Kump, 1994; Amiotte-Suchet and Probst, 1993; Meybeck, 1987). In global calculations weathering rates are often extrapolated using runoff-relationships of determined weathering fluxes at the catchment scale (Hartmann et al., 2014b; Hartmann et al., 2009; Amiotte-Suchet and Probst, 1995).

Weathering rates of carbonate and silicate minerals may also be modelled using chemical kinetic equations, determined by experimental studies, combined with fluid mechanics. The change of concentration over time, or rate of reaction (dC_i/dt), is quantified by the following generalized kinetic equation at constant volume (Schott et al., 2012; Steefel and Lasaga, 1994):

$$\frac{dC_i}{dt} = Ak_i a_i^n (1 - \Omega) \tag{1.4}$$

where A is the reactive surface area of a mineral, a_i is the activity of chemical species i, n the order of reaction with respect to species i, Ω is the saturation index of the reaction, and k_i is the rate constant. The temperature dependence of the rate of a chemical reaction is associated to the rate constant determined by the empirical Arrhenius equation (Lasaga, 1984):

$$k = k_a e^{-\frac{E_a}{RT}} \tag{1.5}$$

k_a represents the pre-exponential factor, E_a is the activation energy of the reaction, R is the ideal gas constant and T temperature in kelvin. Equations 1.4 and 1.5, obtained from empirical studies, consider that the speed of any chemical reaction increases with temperature and decreases with activation energy. These equations, however, do not consider thermodynamic (classical thermodynamics or quantum mechanics) dependence of a chemical process, instead, they represent the thermodynamic limit with the term $(1 - \Omega)$.

The different methods to determine regional or global weathering rates consider that the dissolution of minerals is produced by the reaction with hydrogen ions from the carbonic acid, major hydrogen ion supply in the soil system (Berner et al., 1983; Walker et al., 1981). However, other acids like sulphuric acid, nitric acid, hydrochloric acid and organic acids should be taken into account because they can contribute to weathering of minerals that are, otherwise, assumed to be due to the dissolution of atmospheric CO_2 into water (Beaulieu et al., 2011; Gaillardet et al., 2011; Calmels et al., 2007; Mast and Drever, 1987; Žutić and Stumm, 1984).

Another process commonly depreciated is the influence of organisms, in the soil profile, on the weathering process. Organisms use enzymes to facilitate release of nutrients; some of these enzymes can increase significantly the dissolution of CO_2 in soil pore-water (Liu et al., 2005). Moreover, organic compounds can adsorb cations and trace elements, the latter relevant as micronutrients, and mobilize them inside the soil profile (Zuyi et al., 2000).

The kinetic equations are problematic to incorporate into global carbon cycle models because of the different rates of dissolution between minerals, which demands a significant increase on computational time. The reason of this is that numerical solution requires a relatively smaller time step for solving carbonate mineral dissolution than silicates, making the combination of different minerals unstable to solve numerically, thus the solution for the system of ordinary differential equations becomes stiff (Hellevang et al., 2013).

1.2 Hotspots of weathering fluxes

The highest weathering fluxes are located in hydrological catchments dominated by carbonate rocks and in volcanic systems (Li et al., 2016; Hartmann et al., 2014b; Hartmann et al., 2009; Amiotte-Suchet and Probst, 1995). The carbonate rocks, containing mostly calcite, cover approximately 10% of continental areas (Hartmann and Moosdorf, 2012; Dürr et al., 2005) and weather faster than silicate minerals (Brantley, 2008; Dreybrodt et al., 1996; Reddy et al., 1981). Weathering fluxes of carbonate minerals are mainly controlled by hydrology (Zhong et al., 2017), partial pressure of CO_2 (pCO_2) and temperature (Calmels et al., 2014); and its intensity is sensitive to climate (Gaillardet et al., 2018). Otherwise, physical erosion processes might not be relevant for carbonate lithologies owing to their fast dissolution kinetics (Dreybrodt et al., 1996). There remains uncertainty, however, of how environmental and climatic factors steer carbonate weathering spatially, and how climate change and land-use might influence global carbonate weathering rates over time. Furthermore, the application of thermodynamic equations on global carbonate models is limited to the availability of global pCO_2 data and the understanding of processes governing the dissolution of carbonate minerals and the transport of its products to the ocean at global scale.

On the other hand, usually primary minerals, within silicates, associated to basic rocks dissolve faster than those related to acid rocks (Drever, 1997). Furthermore, from Eq. 1.4 it can be concluded that changes on mineral surface area have an impact on mineral dissolution and precipitation rates, and at regional or global scale, this effect can be distinguished by textural properties of major lithological types. For silicate dominated lithological classes, unlike carbonate minerals, physical erosion is an additional relevant process as it supplies fresh minerals prone to CO_2 consumption (West et al., 2005).

Volcanoes, representing the most important natural source of carbon from the mantle to Earth's surface, are recognized as supporters for fertile soils since human history (Ugolini and Dahlgren, 2002), being the result of the high nutrient release rate due to weathering of volcanic and pyroclastic materials (Hartmann et al., 2014b; Hartmann et al., 2009). In inactive volcanic systems, however, the weathering intensity is much lower than in active ones (Li et al., 2016). This may be due to the constant input of fresh material by volcanoes, with relatively high surface area (Li et al., 2016; White and Brantley, 2003; Louvat and Allègre, 1998); or it can also be because of the influence of dissolution of minerals by strong acids of magmatic origin and mixing of groundwater with hydrothermal fluids (Gaillardet et al., 2011; Rad et al., 2011). However, the contribution of magmatic SO_2, one of the main volcanic gases in Japan (Aiuppa et al., 2017), on chemical fluxes is challenging to quantify because of a lack of a proxy with relatively low uncertainty for hydrothermal processes.

Selenium (Se), a trace element and essential micronutrient, presents a similar geochemical behaviour than sulphur (McNeal and Balistrieri, 1989; Shamberger, 1981). Therefore, a relatively constant Se:S ratio is expected for several natural samples (Queffurus and Barnes, 2015; Dreher and Finkelman, 1992; Deverel and Fujii, 1988). In hydrothermal systems, however, different Se:S ratios are observed and they are usually lower than in soil, river or atmospheric systems (Winkel et al., 2015; Fellowes et al., 2013; Floor and Román-Ross, 2012; Yamamoto, 1976; Suzuoki, 1964). Moreover, isotopic composition of natural samples provides information about sources, physical and chemical processes and about thermodynamic conditions of the system (Hoefs, 2009; Rye, 2005; Barnes and Allison, 1988; Deines et al., 1974). The combination of isotopic composition and ratios of chemical species provides necessary information to quantify mixing processes. Therefore, in this work the application of Se:S ratio and stable isotopes are tested to decipher the hydrothermal influence in a specific volcanic system in Japan.

1.3 Objectives

In the present study, weathering of carbonate rocks is extensively studied in order to improve current global weathering models, relevant for modelling the carbon cycle, with the use of global databases of spring and river waters. Furthermore, the hydrothermal influence on dissolution of primary minerals in volcanic systems is quantified using new parameters as proxy for hydrothermal fluids. The main objective of this study is to untangle key processes affecting global weathering from carbonate lithologies and in volcanic systems. In order to fulfil this objective the following specific tasks were defined:

1.3.1 Specific objectives:

1. To study spring water chemistry draining carbonate lithologies to understand soil properties and main mechanisms acting in weathering of carbonate minerals.
2. To study the use of equilibrium equation in modelling global weathering of carbonate minerals and to understand which processes are relevant in parameterizing weathering rates of carbonate minerals at the global scale.
3. To quantify the input of hydrothermal acids in Aso caldera, Japan, by applying Se:S molar ratios and stable isotopes of carbon and sulphur.
4. To determine the potential contribution of magmatic gases SO_2 and CO_2 on chemical weathering rates in Aso caldera, Japan.

Chapter 2: Carbonate System I

Spring water chemistry and soil pCO$_2$

This chapter has been published as: Romero-Mujalli, G., Hartmann, J., Börker, J., Gaillardet, J. and Calmels, D., 2018. Ecosystem *controlled soil-rock pCO$_2$ and carbonate weathering – Constraints by temperature and soil water content. Chemical Geology. DOI: 10.1016/j.chemgeo.2018.01.030.*

2.1 Abstract

Carbonate dissolution in soil-groundwater systems depends dominantly on pH, temperature and the saturation state of the solution with respect to abundant minerals. The pH of the solution is, in general, controlled by partial pressure of CO$_2$ (pCO$_2$) produced by ecosystem respiration, which is controlled by temperature and water availability. In order to better understand the control of land temperature on carbonate weathering, a database of published spring water hydrogeochemistry was built and analysed. Assuming that spring water is in equilibrium with the soil-water-rock-atmosphere, the soil pCO$_2$ can be back-calculated. Based on a database of spring water chemistry, the average soil-rock CO$_2$ was calculated by an inverse model framework and a strong relationship with temperature was observed. The identified relationship suggests a temperature control on carbonate weathering as a result of variations in soil-rock pCO$_2$, which is itself controlled by ecosystem respiration processes. The findings are relevant for global scale analysis of carbonate weathering and carbon fluxes to the ocean, because concentration of weathering products from the soil-rock-system into the river system in humid, high temperature regions, are suggested to be larger than in low temperature regions. Furthermore, results suggest that, in specific spring samples, the hydrochemical evolution of rain water percolating through the soil-rock complex can best be described by an open system with pCO$_2$ controlled by the ecosystem. Abundance of evaporites and pyrite sources influence significantly the chemistry of spring water and corrections must be taken into account in order to implement the inverse model framework presented in this study. Annual surface temperature and soil water content were identified as suitable variables to develop the parameterization of soil-rock pCO$_2$, mechanistically consistent with soil respiration rate findings.

2.2 Introduction

The production of carbon dioxide (CO$_2$) in soils depends mostly on microbial activity and root respiration which in turn are dependent on temperature and soil water content, parameters representing climate variability (Lellei-Kovács et al., 2016; Kuzyakov, 2006; Mielnick and Dugas, 2000; Amundson and Davidson, 1990). Soil respiration is a major component in the carbon cycle and is considered to be one of the largest biological CO$_2$ fluxes from land to the atmosphere (Raich and Potter, 1995). Nevertheless, soil CO$_2$ when dissolved in water, represents the major hydronium ion supply in the weathering system, and it is consumed through weathering reactions (Calmels et al., 2014; Berner et al., 1983; Walker et al., 1981).

Quantifying the weathering fluxes from land to the coastal zone is of interest to understand the atmospheric/soil CO$_2$ consumption potential through chemical weathering. Several authors have tried to constrain these fluxes studying the chemistry of large rivers (Gaillardet et al., 1999), using phenomenological models to determine global weathering fluxes for different types of lithological classes (Goll et al., 2014; Hartmann et al., 2014b; Hartmann, 2009; Hartmann et al., 2009; Bluth and Kump, 1994; Amiotte-Suchet and Probst, 1993), or applying mechanistic models based on kinetic equations and hydrology to quantify the weathering fluxes from soil-rock system to the rivers (Goddéris et al., 2013; Beaulieu et al., 2012; Roelandt et al., 2010; Goddéris et al., 2006). Nevertheless, the mechanistic models require as an important input the soil partial pressure of CO_2 (pCO_2), which controls the saturation state with respect to minerals and therefore the amount of minerals that can be dissolved.

The weathering of carbonate rocks is a dynamic process and variations on timescales of hours are documented, as well as fast precipitation, mainly dependent on the concentration of CO2 in the aqueous system (Calmels et al., 2014; Pu et al., 2013; Roland et al., 2013; Serrano-Ortiz et al., 2010). The fast calcite dissolution implies that equilibrium is easily reached with respect to a given pCO_2 (Dreybrodt et al., 1996; Reddy et al., 1981) without expecting fast calcite precipitation due CO_2 degassing in the spring water (Szramek and Walter, 2004). As a consequence, the alkalinity in spring water presents the spatio-temporal variation of CO_2 of its catchment source system (Calmels et al., 2014; Yoshimura et al., 2001). In that way, the concentration of chemical species resulting from carbonate weathering might be a good parameter to forecast the soil pCO_2 in a soil-carbonate rock-system.

There are, at least theoretically, two extreme models to describe carbonate dissolution. The “open system” corresponds to an infinite CO_2 reservoir that equilibrates with the dissolving solution (or sustained supply of CO_2). The “closed system” corresponds to the case where a given initial amount of CO_2 equilibrates with the solution and no further supply is provided. In both cases, CO_2 is consumed through the weathering reaction according to the chemical equations of the carbonate system until saturation with respect to calcite is reached. Although both cases should exist in reality, the soil-carbonate rock weathering system more likely operates as an open system because (i) an ongoing flux of CO_2, due to the ecosystem respiration and microbial activity, might be expected and (ii) the dissolution of calcium carbonate rocks is a relatively fast process.

The aim of this study is to back-calculate the soil-rock pCO_2 based on equilibrium equations and considering open and closed conditions for carbonate dominated lithologies, using spring water chemistry. In addition, a framework to retrieve a generalized soil-rock pCO_2 function for carbonate rock dominated areas based on land properties sensitive to climate variability is presented.

2.3 Methodology

2.3.1 Spring water chemistry and data filtering.

A spring database for carbonate lithologies was constructed based on publications where carbonates rocks are considered an important lithological class in the catchment and information of the chemistry of the water was available (Fig. 2.1). The database is composed of 671 data points from 26 different publications and sampling locations are located approximately between latitudes 20° and 60° N. For each sample point an estimate of the coordinates was determined. $\delta^{13}C$ data, when reported, was included in the database (Supplement Information can be found online in: https://doi.org/10.1016/j.chemgeo.2018.01.030) because it can be used to determine the source of CO_2, degassing processes and to identify the influence of redox processes.

Some studies reported water chemistry data from hot or cold springs where CO_2 from deep sources and hydrothermal processes is likely (Kohfahl et al., 2008; Yoshimura et al., 2004; Yoshimura et al., 2001; Chiodini et al., 1999; Herman and Lorah, 1987). In this case, the $p\mathrm{CO_2}$ in the soil-rock system is not representative of the soil CO_2 produced by the ecosystems. Therefore, filtering of data is needed in order to select samples with ideal conditions characteristic of the interactions between the Ca-carbonate rock, water and the ecosystem. In addition, sulphide oxidation and gypsum dissolution may change the alkalinity of the solution interacting with carbonate. If silicates are present in the catchment, they may add excess alkalinity. In order to minimize the influence of evaporites, sulphide oxidation processes or hydrothermal processes the following filtering criteria were applied:

(i) $([Ca^{2+}] + [Mg^{2+}])$/Alkalinity molar ratio < 0.9, in order to discard the extreme values shown in Fig. 2.2a, where these cations may be related to a source other than carbonate minerals by soil CO_2.

(ii) $[Ca^{2+}]/[SO_4^{2-}]$ molar ratio should be > 10 (Fig. 2.2b), to discard samples affected by sulphide oxidation and sulphate mineral dissolution.

(iii) $[Ca^{2+}]/[Na^{+}]$ molar ratios should be > 12, in order to minimize the effect silicate weathering (Fig. 2.2c), based on Gaillardet et al. (1999) relations and data analysis reported therein.

(iv) $[Ca^{2+}]/[Mg^{2+}]$ molar ratio should be larger than 1, to minimize contribution of other carbonate minerals than calcite and silicate minerals (Fig. 2.2d), and to be able to apply equilibrium equations for calcite dissolution system.

(v) The charge balance error (CBE) should be < 10%, to exclude points with high uncertainty associated to the reported water chemistry data. CBE was calculated by the following equation:

$$CBE = \frac{\sum_{p=1}^{n} Ce_p - \sum_{j=1}^{m} Ce_j}{\sum_{p=1}^{n} Ce_p + \sum_{j=1}^{m} Ce_j} * 100 \tag{2.1}$$

Where Cep and Cej represent the concentration in equivalent of cation p and anion j, respectively. A more rigorous condition for CBE was not necessary to apply because the deviation due seasonality is larger.

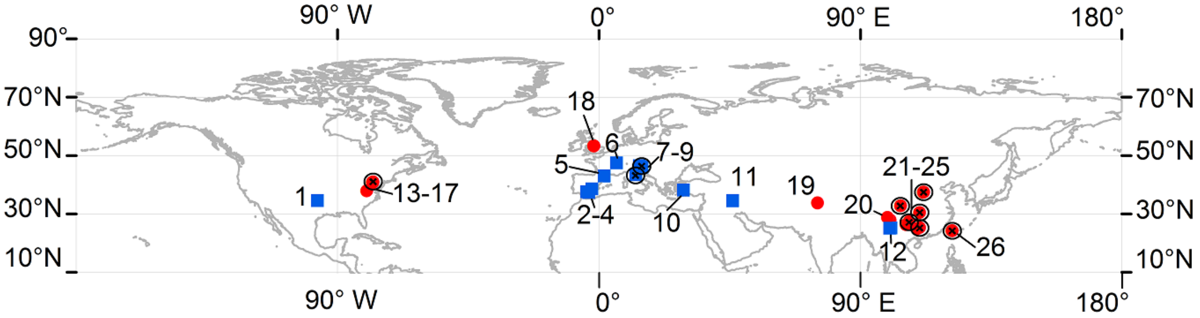

Figure 2.1. Global distribution of the spring samples considered in the present study. Blue squares represent publications which fulfil the conditions proposed in the methodology, red circles correspond to publications with no measurements satisfying the conditions, and the black X marks stand for publications where $\delta^{13}C$ measurements in

water were reported. 1 = Abongwa and Atekwana (2015). 2 = López-Chicano et al. (2001). 3 = Kohfahl et al. (2008). 4 = Moral et al. (2008). 5 = Dandurand et al. (1982). 6 = Calmels et al. (2014). 7 = Chiodini et al. (1999). 8 = Kanduč et al. (2012). 9 = Szramek et al. (2011). 10 = Özkul et al. (2010). 11 = Karimi et al. (2005). 12 = Huang et al. (2015). 13 = Herman and Lorah (1987). 14 = Jacobson and Langmuir (1970). 15 = Langmuir (1971). 16 = Deines et al. (1974). 17 = Jacobson and Langmuir (1974). 18 = Smith and Wood (2002). 19 = Jeelani et al. (2011). 20 = Pu et al. (2013). 21 = Zhao et al. (2015). 22 = Zaihua et al. (1997). 23 = Yoshimura et al. (2004). 24 = Long et al. (2015). 25 = Qibo et al. (2016). 26 = (Yoshimura et al., 2001).

Correction for rain water was not possible due to lack of information on the chemistry of rainwater at each sample site but given the low pH of rainwater, the input of alkalinity by rain water is negligible. Seasonality was not considered due to limitation on the dataset and because the applied data for land temperature and soil water content implemented was based on year average. The chemistry of the selected spring samples (164 in total) is dominated by [Ca^{2+}] and alkalinity, an important condition to apply simple equilibrium calculations of the system $CaCO_3$-H_2O-CO_2.

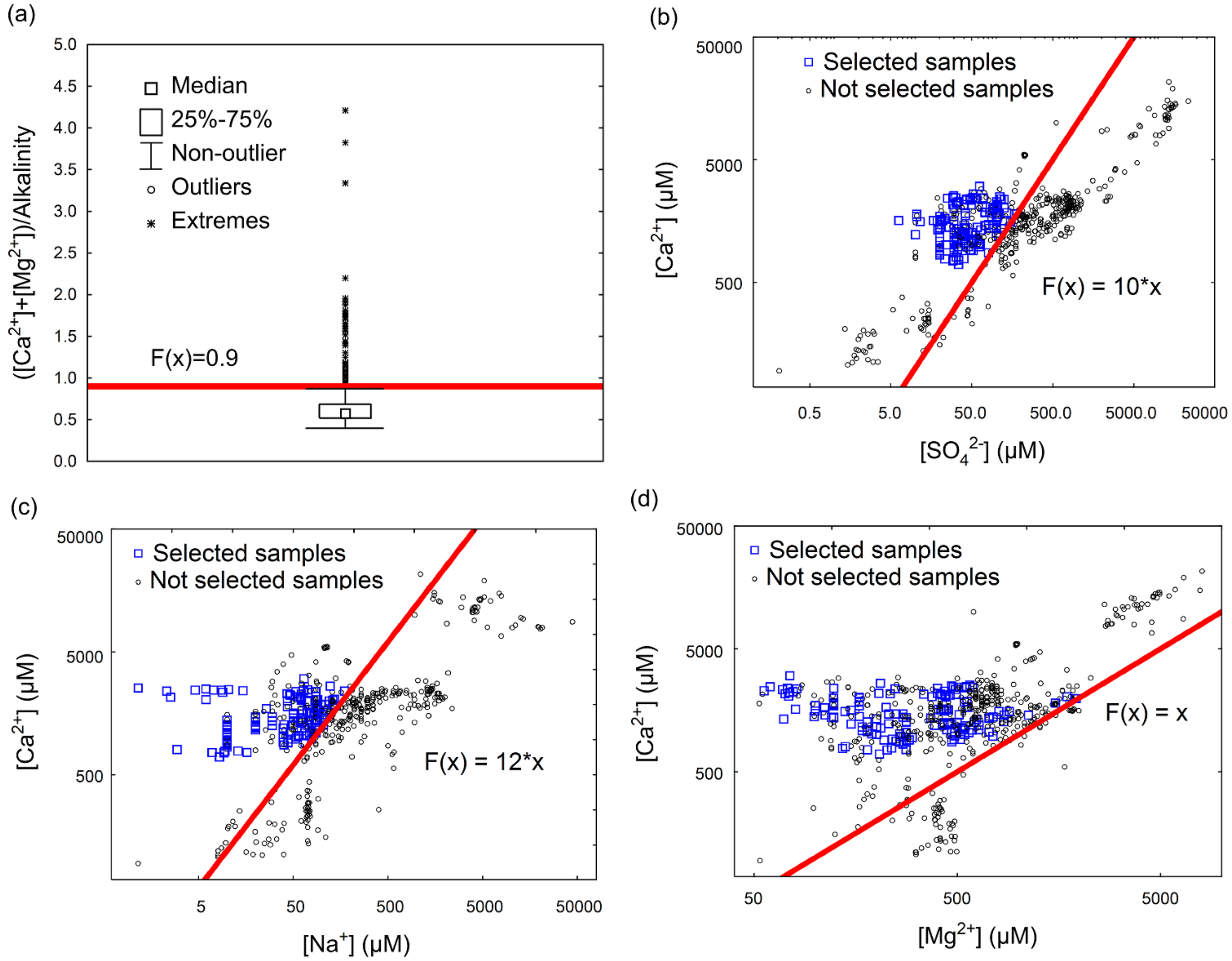

Figure 2.2. Molar ratios and relations between chemical species: Graph (a) represents the box-plot of ([Ca^{2+}] + [Mg^{2+}])/Alkalinity molar ratio; and graphs (b), (c) and (d) are logarithm scale-scatterplots for [Ca^{2+}] against [SO_4^{2-}], [Na^+] and [Mg^{2+}], respectively. *F(x)* stands for the selection criteria for each corresponding molar ratio and blue squares represent the samples which fulfil the conditions proposed in the methodology.

2.3.2 Model description.

A numerical code was constructed to calculate the $p\mathrm{CO_2}$ at equilibrium with spring samples considering the open system calcite-$\mathrm{CO_2}$-water (equilibrium equations included in the model is described in Appendix B). The inverse model calculates the $p\mathrm{CO_2}$ required to produce the alkalinity values reported in each sample at the determined temperature assuming equilibrium with calcite. Alkalinity is considered to be $[\mathrm{HCO_3^-}] + 2[\mathrm{CO_3^{2-}}] + [\mathrm{OH^-}] - [\mathrm{H^+}]$, because no other chemical species with significant contribution to alkalinity were reported in the applied dataset. The construction of this model is based on three assumptions: (i) alkalinity values in spring waters dominated by weathering of carbonate lithologies depend, mainly, on the soil-rock $p\mathrm{CO_2}$; (ii) the system is at equilibrium with calcite (saturation index = 0); and (iii) ionic balance between chemical species $[\mathrm{H^+}]$, $[\mathrm{Ca^{2+}}]$, $[\mathrm{OH^-}]$, $[\mathrm{HCO_3^-}]$ and $[\mathrm{CO_3^{2-}}]$ was considered for all samples.

Furthermore, a closed-system calculation was carried out to determine the $p\mathrm{CO_2}$ required to produce the alkalinity values reported in the spring samples. In this case, the initial dissolved $\mathrm{CO_2}$ concentration, here as $[\mathrm{CO_{2(aq)}}]_{initial}$, was calculated as the sum of the $\mathrm{CO_2}$ at equilibrium in the closed system calcite-water-$\mathrm{CO_2}$, $[\mathrm{CO_{2(aq)}}]$, plus the amount of $\mathrm{CO_2}$ which reacted with the calcite, which is equivalent to the calcium concentration, $[\mathrm{Ca^{2+}_{(aq)}}]$.

$$[CO_{2(aq)}]_{initial} = [Ca^{2+}_{(aq)}] + [CO_{2(aq)}] \tag{2.2}$$

The $p\mathrm{CO_2}$ at equilibrium with the water (water $p\mathrm{CO_2}$) was calculated using PHREEQC software and "phreeqc.dat" database (Parkhurst and Appelo, 1999) and compared with the $p\mathrm{CO_2}$ estimated applying the inverse method presented in this study.

2.3.3 Global datasets

The calculated $p\mathrm{CO_2}$ was estimated by identifying suitable functional relationships using land surface temperature and soil volumetric water content, parameters often used for modelling the soil respiration (Cartwright and Hui, 2015; Gaumont-Guay et al., 2006; Mielnick and Dugas, 2000; Epron et al., 1999). Soil volumetric water content values were taken from the European Space Agency Climate Change Initiative data portal (ESA, http://www.esa-soilmoisture-cci.org/). This data, with a spatial resolution of 0.25°, represents the daily surficial water content of soils (depth < 5cm) in volumetric units ($\mathrm{m^3\ m^{-3}}$) calculated from the degree of saturation and soil porosity, and was developed by remote sensing methods which correlate the dataset with in-situ measurement stations (Dorigo et al., 2015; Liu et al., 2012; Wagner et al., 2012). Mean annual land surface temperature values with a spatial resolution of $1\mathrm{km^2}$ were extracted from Hijmans et al. (2005). The calculated $p\mathrm{CO_2}$ was estimated using the annual mean soil volumetric water content (θ) and the global surface temperature by non-linear methods applying the Levenberg-Marquardt algorithm (functional relationships are discussed below).

2.4 Results

The compiled dataset is composed of 671 sample points representing different regions of the world where carbonate rocks dominate the catchment. Surface temperature and soil volumetric water content for the 164 selected spring samples range from 0.4 to 22.0°C and from

0.17 to 0.37m^3 m^{-3}, respectively. Subsequently, 164 sample points were selected based on the filtering method described in *section 2.3.1*, centered on ideal carbonate dissolution signatures. The selected samples have calcite saturation indices (SI) between -0.4 to 1, with a mean value of 0.2. These samples present a moderate positive linear correlation between alkalinity and surface temperature ($r^2 = 0.45$, Fig. 2.3). This relationship is lost if the data selection is not applied, highlighting the difficulty of predicting and understanding complex systems, where water chemistry is influenced by anthropogenic input and evaporite, sulphide or silicate mineral dissolution.

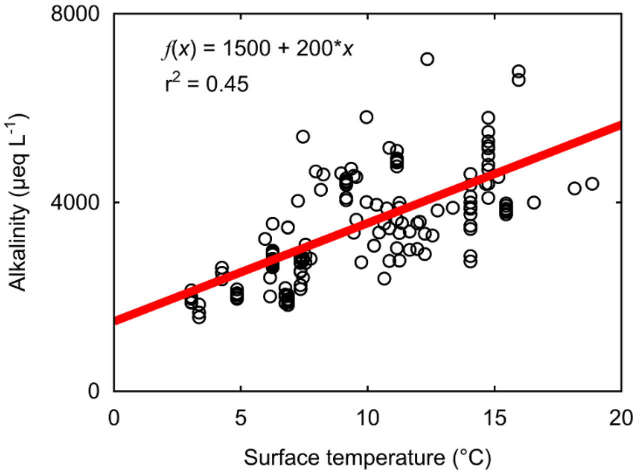

Figure 2.3. Alkalinity against mean annual surface temperature for selected data points based on the conditions explained in section 2.3.1. *f(x)* is the linear function of the correlation represented by the red line.

2.4.1 Stable carbon isotopes

Understanding the behaviour of stable carbon isotopes in spring water samples is useful to obtain information regarding the source of CO_2 and possible processes occurring in the spring water system. From 671 total spring samples, only 118 samples reported $\delta^{13}C$ values, ranging from -20.6 to -0.3‰. Consequently, this variable was not used as imperative criteria for filtering the data. Nevertheless, the relationship between $\delta^{13}C$ and alkalinity and pH allowed to distinguish at least two different groups (Fig. 2.4): a first group with relatively low values of $\delta^{13}C$ (less than -4‰) and low alkalinity (< 8000µN) and a second group with elevated values of $\delta^{13}C$ (higher than -5‰) and alkalinity values larger than 8000µN.

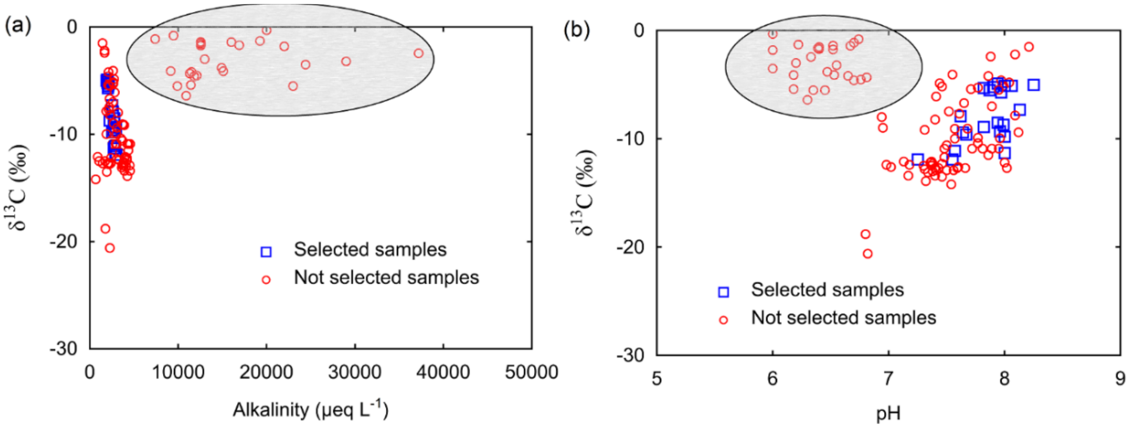

Figure 4. Scatterplots for $\delta^{13}C$ (‰) against (a) alkalinity (µeq L^{-1} or µN) and (b) pH. Selected spring samples based on section 2.3.1 are represented by blue squares, red circles stand for the excluded sample points. The grey region shows samples with significant deep source of CO_2.

Spring samples with high $\delta^{13}C$ and alkalinity may be the result of the dissolution of calcite under the influence of CO_2 from deep sources, or reaction of calcite with strong acids (Li et al., 2008; Yoshimura et al., 2004; Yoshimura et al., 2001), as implied by a generally lower pH values in Fig. 2.4b. Therefore, the $\delta^{13}C$ was used as a minor condition to exclude samples possibly influenced by deep CO_2 or hydrothermal processes. The resulting selected spring water samples present a good relationship between $\delta^{13}C$ and alkalinity (Fig. 2.4a), where high values of $\delta^{13}C$ are related to the lowest values of alkalinity reported in these spring samples. This may imply that the isotopic composition of soil CO_2 was controlled by biological respiration and microbial oxidation of organic matter ($\delta^{13}C$ approximately -25‰ for C3 plants), and atmospheric CO_2 ($\delta^{13}C$ between -9 and -8‰), as suggested by Cerling et al. (1991) where low respiration rate leads to higher $\delta^{13}C$ for soil CO_2. Moreover, the high values of $\delta^{13}C$ in spring samples also may imply a significant degassing of CO_2 from the springs before sampling (Deines et al., 1974).

The $\delta^{13}C$ of selected spring samples behaves as predicted by models of calcite dissolution under open and closed system conditions if degassing is considered (Deines et al., 1974). However, in order to differentiate between closed and open system conditions the isotopic composition of the initial CO_2 (soil CO_2) has to be known because it represents the initial condition in the calculations.

2.4.2 Calculated pCO_2

The soil-rock pCO_2 obtained by applying the inverse method (section 2.3.2) is different from the spring water pCO_2 (Fig. 2.5), calculated with PHREEQC using “Phreeqc.dat” database and the equilibrium method (Parkhurst and Appelo, 1999). Spring water pCO_2 represents the pCO_2 at equilibrium with the pH and alkalinity of the spring water at the time the water sample was taken. The soil-rock pCO_2 considering an open system condition is similar to the spring water pCO_2 values (Fig. 2.5a). Oversaturated samples show higher soil-rock pCO_2 values than spring water pCO_2, and undersaturated solutions plot on the 1:1 line (Fig. 2.5a) because the saturation index with respect calcite (SI) is near 0. When a closed system condition is considered, the soil-rock pCO_2 values are much higher than the spring water pCO_2 (Fig. 2.5b), but again oversaturated samples show on average elevated pCO_2 values. These differences, based on the calcite saturation index (SI), are the result of considering equilibrium with calcite (SI of 0) in the soil-rock system with the inverse method (see method in section 2.3.2). The available $\delta^{13}C$ data may imply that degassing of CO_2 in spring water is relevant in some cases. If degassing takes place, the calculated equilibrium pCO_2 for the spring water decreases while increasing the saturation with respect to calcite. However, precipitation of calcite may not occur always immediately because the degassing rate of CO_2 is significantly higher than the precipitation rate of calcite (Dreybrodt et al., 1996). Hence, the soil-rock pCO_2 should be calculated applying the inverse method presented in this study (considering SI = 0) using the chemical composition of spring samples rather than calculating the pCO_2 at equilibrium with the spring water.

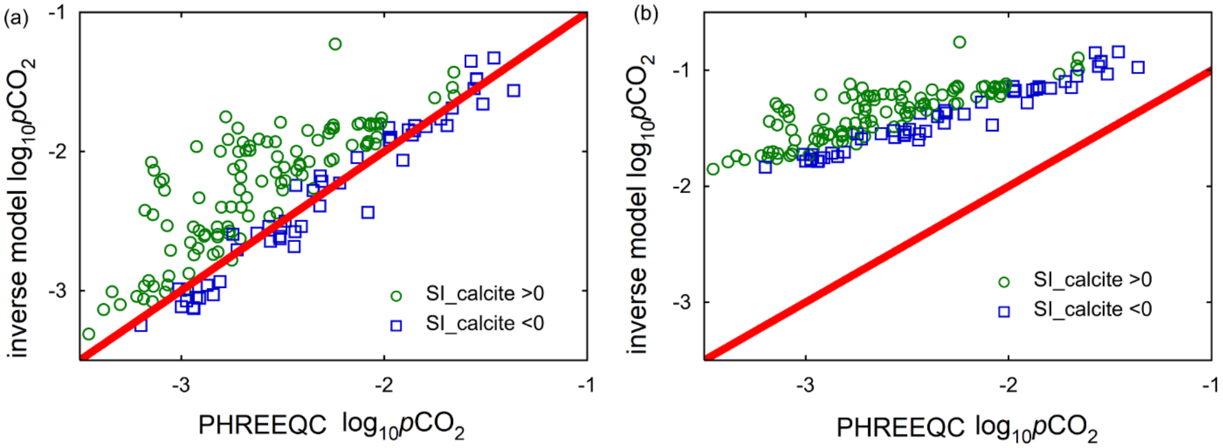

Figure 2.5. Relation between calculated pCO_2 applying the inverse method (section 2.3.2) and water pCO_2 calculated by PHREEQC software (PHREEQC $\log_{10}pCO_2$) using "Phreeqc.dat" database (Parkhurst and Appelo, 1999), for (a) Open system condition and, (b) closed system condition. Red line represents the 1:1 relation.

The soil-rock pCO_2 under closed conditions ranges from 0.014 to 0.18atm, and is thus clearly higher than open system conditions which range from 0.00049 to 0.059atm (Fig. 2.6). The soil-rock pCO_2 considering an open system fits in the range proposed by Yoshimura et al. (2001) for soil pCO_2 for average Japanese soils (Fig. 2.6), unlike the closed system pCO_2, which shows even higher values than would be expected for humus soil conditions (Yoshimura et al., 2001). The closed condition presents high values of pCO_2 at low temperature (near 3°C); where less soil respiration is expected due to a decrease in biological activity. This implies that the underground production of CO_2 related to $CaCO_3$-H_2O-CO_2 system should lead to a partial pressure of approximately 0.01atm, if a closed system is considered. However, the minimum value of pCO_2 calculated considering an open system (0.00049atm) is close to atmospheric pCO_2, which is comparable to results from respiration models (Lellei-Kovács et al., 2016; Suseela et al., 2012; Frisia et al., 2011; Cerling et al., 1991).

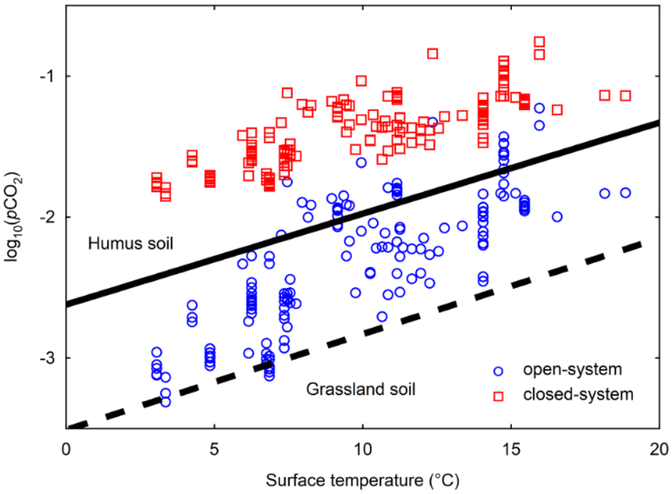

Figure 2.6. Calculated partial pressure of CO_2 against temperature with the introduced inverse method for open- (blue circles) and closed-system (red squares) conditions at equilibrium with calcite. Solid and dashed black lines are limits for soil pCO_2 for average Japanese humus and grassland soils, respectively, taken from Yoshimura et al. (2001). The results for the closed system conditions are located above what would be expected for humus soil conditions.

To further investigate the role of controlling variables on the calculated soil-rock pCO_2, a function (Eq. 2.3) depending on temperature and soil volumetric water content (θ), variables commonly used in soil respiration models to explain soil respiration rates (Banerjee et al., 2016; Mielnick and Dugas, 2000), is fitted with the objective to introduce another dimension on the controls of soil-rock pCO_2 for open system conditions. The dependency of soil respiration on soil volumetric water content is commonly represented as a polynomial function, presenting low respiration fluxes for both low and high values of soil volumetric water content. Soil respiration, generally, has maximum rates for soil volumetric water contents between 0.2 and 0.4m^3 m^{-3} (Banerjee et al., 2016; Ilstedt et al., 2000). In addition, temperature controls biological activity and thus influences soil pCO_2. Soil respiration is often described as being directly proportional to temperature (Lellei-Kovács et al., 2016; Lloyd and Taylor, 1994). Therefore, the function developed to calculate the logarithm of the partial pressure of CO_2 in the soil ($\log_{10}pCO_2$) is represented by the following equation and based on findings from Fig. 2.7:

$$log_{10}pCO_2 = \frac{e^{(b_1\theta)+(\frac{b_2}{\theta})}}{(b_3 + e^{b_4 T})} + log_{10}pCO_{2atm} \tag{2.3}$$

where θ represents the mean annual volumetric water content (v/v); T is the mean annual surface temperature in degrees Celsius, $\log_{10}pCO_{2atm}$ is the logarithm of partial pressure of CO_2 in the atmosphere (a value of -3.4 was considered in this work); b_1, b_2, b_3 and b_4 are fitted constants with average values of -3.0 ± 0.7, -0.25 ± 0.04, 0.09 ± 0.03 and -0.34 ± 0.05, respectively. A random distribution of residuals is observed, indicating that the regression is not biased by the distribution of applied variables (Fig. 2.8). The standard deviation of the function calculated by residuals is ± 0.3 ($\log_{10}pCO_2$), resulting in an interval of ± 0.6 ($\log_{10}pCO_2$) for the 90% confidence level of the fitted function. The R^2 between calculated soil-rock pCO_2 by the inverse method and the estimated pCO_2 by the fitted function is 0.67, and thus significantly higher than the linear correlation between alkalinity and surface temperature with $r^2 = 0.45$, which does not consider soil volumetric water content.

The lower limit in Eq. (2.3) is considered to be the pCO_2 concentration in the atmosphere, where soil respiration is low and atmospheric CO_2 diffuses from the atmosphere into the soil (Dörr and Münnich, 1980). Furthermore, a maximum threshold for soil pCO_2 is established based on the spring water chemistry, which may represent the limit of biological activity. However, it is not possible to predict pCO_2 at higher land temperatures (> 20°C) due to the absence of data. Therefore, global applications might be limited by the range of temperature (3 to 19°C) and soil volumetric water content (from 0.17 to 0.37m^3 m^{-3}) in the applied dataset for the development of the function. The function may also be only applicable for catchments dominated by carbonate rocks, until further studies confirm the identified pattern.

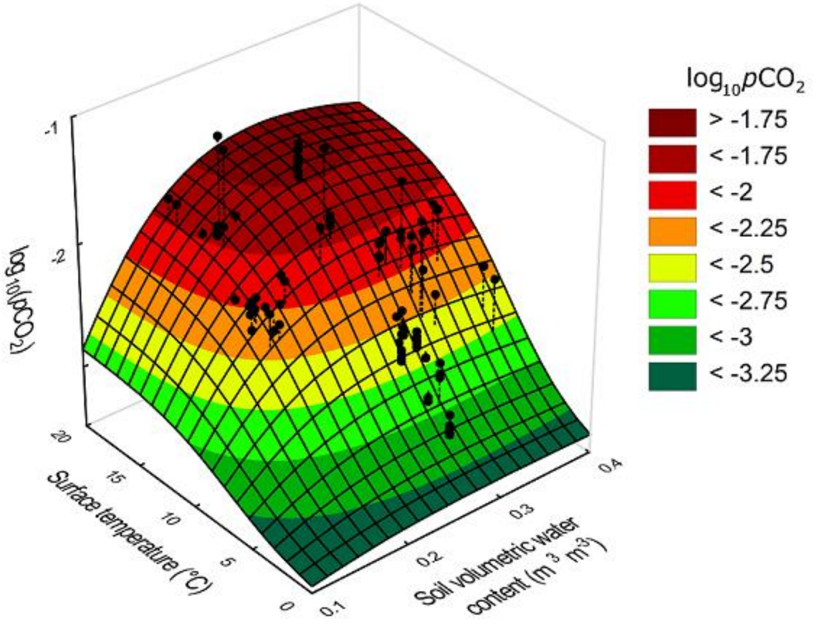

Figure 7. Fitted function representing the soil pCO_2 (Eq. 2.3) depending on mean annual surface temperature (°C) and mean annual volumetric water content (m^3 m^{-3}). Black points represent the calculated pCO_2 based on the inverse method (section 2.3.2). Coloured regions represent different values of $\log_{10}pCO_2$.

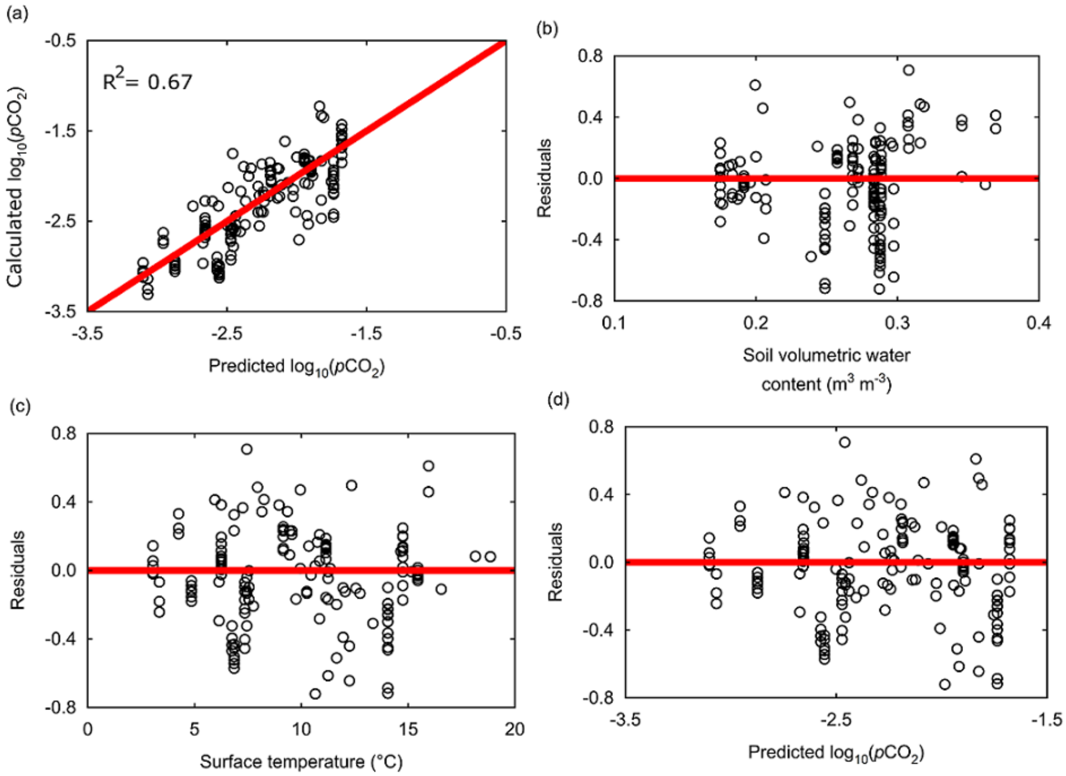

Figure 2.8. Predicted pCO$_2$ against calculated pCO$_2$ values and residuals plots for the new parameterization of pCO$_2$ (Eq. 2.3). (a) Calculated pCO$_2$ against predicted pCO$_2$ values, (b) residuals against soil volumetric water content, (c) residuals against surface temperature, and (d) residuals against predicted pCO$_2$ values. The red line represents the condition in which residuals are equal to zero. The partial pressures of CO$_2$ are expressed as decimal logarithm of atmosphere. Residuals were calculated as: Observed values - Predicted values.

2.5 Discussion

This work shows that spring water samples can be used to estimate an average soil-rock pCO$_2$, considering open system conditions. The proposed model-framework can be used to estimate alkalinity fluxes out of the soil-rock system using climate relevant parameters like temperature and soil water content, which are forcing factors on soil respiration rates and thus CO$_2$ production. With this it is possible to link alkalinity exported from a soil-rock system into a river system with climate forcing. This framework can be improved if more data from climate regions are included, for which now a gap exist.

Data selection was an imperative step in order to apply the presented inverse soil-rock pCO$_2$ calculation method. For instance, relevant dissolution of evaporite, sulphide and silicate minerals would result into different values as estimated based on an ideal calcium carbonate system with respect to alkalinity concentrations and CO$_2$-consumption. In a system at equilibrium with gypsum, calcite, water and CO$_2$ the alkalinity concentrations are approximately 40% lower than in a pure calcite-water-CO$_2$ system (Fig. 2.9), because of the common ion effect, where Ca^{2+} concentration depends on dissolution of both minerals. The presented analysis framework can, however, be enhanced by further relevant processes or above named mineral groups, which influence the alkalinity production, if sufficient constraints can be implemented. But this demands that the sources of sulphate (gypsum versus sulphide) need to be known to account for the different effects of both mineral groups (sulphur isotopes are one measure to achieve this). In addition, $\delta^{13}C$ isotope data can be employed to constrain processes like degassing, contribution of deep CO_2 sources, or the role of ecosystem composition and its contribution to the CO_2-budget.

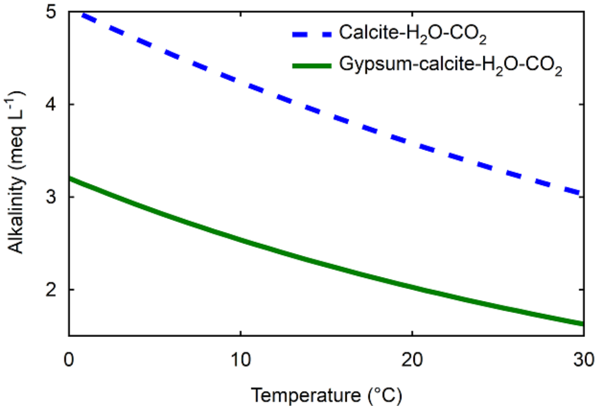

Figure 2.9. Alkalinity against temperature for Calcite-H_2O-CO_2 (blue dash line) and Gypsum-Calcite-H_2O-CO_2 (green line) systems at constant $\log_{10}pCO_2$ value of -2. Results were obtained using the software PHREEQC with “Phreeqc.dat” database (Parkhurst and Appelo, 1999).

The spring water chemistry in karst regions may be developed under different system conditions (open, closed and semi-open conditions) and with influence of different CO_2 sources (Fig. 2.4). However, results based on the filtered data suggest a dominance of open system conditions (Fig 2.6). However, previous studies have found spring water samples from karstic areas which might have developed under semi-open system conditions (van Geldern et al., 2015; Calmels et al., 2014).

2.5.1 Parameterization for estimating soil-rock pCO_2

The dissolution of soil-rock CO_2 into water was considered to be the only hydronium ion contributor for carbonate weathering reactions in the presented analysis framework, without taking into account the contribution of organic acids to the acidification of soils, relevant in organic-rich soils (Thorley et al., 2015). However, soil biological activity promotes CO_2 respiration and hence chemical weathering caused by carbonic acid. In addition, in the soil system, without considering organic acids, the rate-determining process of carbonate weathering is the dissolution of CO_2 in water, which is regulated by the action of the carbonic anhydrase (CA) enzyme in soils (Liu et al., 2005). Furthermore, carbonate weathering can be enhanced by reacting with sulphuric acid. This acid may be produced naturally by the oxidation of sulphide minerals, or related to anthropogenic sources (Wang et al., 2015; Torres et al., 2014; Beaulieu et al., 2011; Li et al., 2008).

Temperature and soil volumetric water content are parameters characteristic of climate conditions, because they play an important role in the budgets of land energy and water balance (Seneviratne et al., 2010). Additionally, the increase in the volumetric water content directly affects microbial activity in the soil, while reducing gaseous and liquid diffusion rates and limiting the supply of oxygen and other gases (Banerjee et al., 2016; Blagodatsky and Smith, 2012). On the other hand, lower values of soil volumetric water content limit the growth rate of plants and the biological activity in the soil (Ilstedt et al., 2000). These conditions explain the shape of the estimated soil-rock $p\mathrm{CO_2}$ by using land surface temperature and soil water content as predictors for open system conditions (Fig. 2.7), exhibiting a maximum $p\mathrm{CO_2}$ value in soils with volumetric water content between 0.2 and $0.4\mathrm{m^3\ m^{-3}}$. The relatively good correlation of soil-rock $p\mathrm{CO_2}$ solely with temperature (Fig. 2.6) demonstrates that soil-rock $p\mathrm{CO_2}$ is highly sensitive to climate variability. Thus, it is possible to estimate the soil-rock $p\mathrm{CO_2}$ only by temperature, when water availability is not a limiting variable, as found by Schwendenmann and Veldkamp (2006) in tropical forests, where the $\mathrm{CO_2}$ was highly correlated with temperature. The compilation used in this work misses values for low and high water contents and high annual land temperatures (higher than 20°C), and it remains therefore unclear if with new data the $p\mathrm{CO_2}$ function based on water content and temperature would result in different $p\mathrm{CO_2}$ values than calculated here.

The soil-rock $p\mathrm{CO_2}$ calculated in this work is representative of depths where weathering reactions occur in carbonate lithologies, because it was calculated after applying a data filtering in order to exclude spring samples under the influence of $\mathrm{CO_2}$ from deep sources and hydrothermal processes. Therefore, the soil-rock $p\mathrm{CO_2}$ functions presented in this work represent the $p\mathrm{CO_2}$ of interest for weathering reactions comparable to other functions such as the one reported by Brook et al. (1983), in which the soil $\mathrm{CO_2}$ at different depths was correlated with actual annual evapotranspiration (AET) and atmospheric $p\mathrm{CO_2}$ ($p\mathrm{CO_{2atm}}$) by the following equation:

$$log_{10}(pCO_2) = log_{10}(pCO_2atm) + 2.09(1 - e^{-0.00172AET}) \tag{2.4}$$

As there exist not many approaches to estimate global patterns of soil $p\mathrm{CO_2}$, the values derived from this work based on Eq. 2.3 are compared for a plausibility test with results obtained using the equation presented by Brook et al. (1983). Global data for AET and annual water content was taken from the Global Land Evaporation Amsterdam Model (GLEAMv3.0). This model consists of a set of algorithms that calculate the different components of terrestrial hydrological water cycle based on satellite observations (Martens et al., 2017; Miralles et al., 2011). Results obtained applying Eq. 2.3 based on this work shows the imprint of temperature and soil water content. For cold regions, low soil $p\mathrm{CO_2}$ are predicted while some humid areas close to the equator show highest soil $p\mathrm{CO_2}$ values (Fig. 2.10a). Soil $p\mathrm{CO_2}$ in arid areas are lower than in humid tropical areas due to low water content values. The soil $p\mathrm{CO_2}$ map obtained using equation 2.4 after Brook et al. (1983) with AET as predictor (Fig. 2.10b) shows a similar spatial pattern as results from Eq. 2.3. However, differences are observed in low temperature regions and deserts. The function from Brook et al. (1983) was created comparing mean annual values of actual annual evapotranspiration with soil $\mathrm{CO_2}$ measured during the growing seasons. This implies that in low temperature regions Eq. 2.4 may overestimate the real mean annual values. Frisia et al. (2011) found that soil $p\mathrm{CO_2}$ from the *Grotta di Ernesto* region, classified as mesothermic-humid climate, can decrease significantly during the winter season (< 5°C) reaching values close to atmospheric $p\mathrm{CO_2}$. This behaviour is not represented by Eq. 2.4. Despite the general good agreement in the patterns and ranges of $p\mathrm{CO_2}$ at the global scale, the formulation of Eq. 2.3 may be a better approach for parameterization of the mean annual soil $\mathrm{CO_2}$ in cold regions, and it can be applied not only to represent mean annual values but to represent seasonal changes, because it will follow temperature changes and water content changes. The simple formulation for a soil pCO_2 function allows constraining the pCO_2 by climate variables without the need of a complex ecosystem model, which has advantages for the study of changes at the global scale over longer time scales for which such a function is representative.

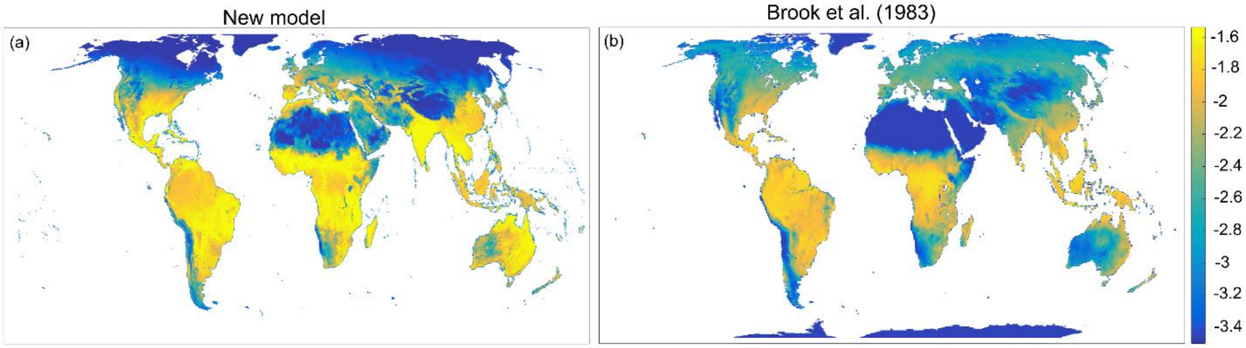

Figure 2.10. Comparison of global soil pCO_2 maps using two different equations: (a) this study, using Eq. 2.3 based on temperature and soil water content for open system conditions, and (b) Eq. 2.4 based on actual annual evapotranspiration (Brook et al., 1983). Colour bar shows $\log_{10}pCO_2$ values. Value ranges of applied data for deriving functions for predicted soil-rock pCO_2 should limit the application area. Appendix A shows the areas which have value ranges for land surface temperature and soil volumetric water content within the ranges of the dataset used in Eq. 2.3.

2.5.2 Global applications

The difference in carbonate rock-soil pCO_2 is mainly influenced by the biological activity in the soil system, which in turn depends on the temperature and water availability. As a result, the pCO_2 estimation framework developed in this work may be a good predictor for soil-rock pCO_2 at a global scale for carbonate rock systems, and possible for other systems in general. Nevertheless, the available data should be enhanced by data from karst areas in high and low temperature regions, and regions with extreme conditions for soil volumetric water content, to ascertain a valid global application (Appendix A, Fig. A.1). If the framework holds for non-carbonate rock conditions, it might be applicable to a much wider range of land areas in general. It should also be considered to enhance the model framework by further factors, which are relevant for weathering products from carbonate sedimentary rocks in general, namely evaporite, sulphide and silicate minerals.

The present framework produces a soil-rock pCO_2, which is comparable in its dependency of temperature and soil water content as implemented in soil respiration flux models, and mechanistically consistent with complex ecosystem functioning. An implementation into global weathering models would allow to represent ecosystem functioning, but would not demand the computational power of incorporating explicit results from complex ecosystem models.

In this way, it might be possible to improve current phenomenological global weathering models in order to consider the soil-rock partial pressure of CO_2 as an important constraint, because it represents a major source of acidity to the water-soil-rock system and its concentration depends on climate conditions. In parallel to the implementation of the new parameterization for soil-rock pCO_2 into global weathering models, results should be compared with measurements of CO_2 in the soil-rock system under a wide range of temperature and soil water content conditions.

2.6 Conclusions

The chemistry of spring waters in areas dominated by carbonate rocks retains a climate and ecosystem signature, suggesting dissolution of minerals under open system conditions with respect to soil-rock CO_2. Therefore, the chemistry of spring waters from catchments dominated by calcium carbonate rocks can be used to estimate the soil-rock pCO_2.

The parameterization for a soil-rock pCO_2 represents an averaged condition of the catchment of the spring waters, and it is centered on model behaviour for soil respiration fluxes. The approach can be employed in studies aimed to quantify calcite weathering fluxes from the terrestrial system into the fluvial system. The presented framework could be enhanced for global scale application to reproduce common settings including dolomite, evaporite and sulphide weathering processes, if additional data sources are compiled and available. As current phenomenological models for prediction of global carbonate weathering do not consider soil pCO_2 as a constraining variable, new approaches may consider soil-rock pCO_2 forced by climate sensitive variables to better understand the control of climate change on carbonate weathering

Chapter 3: Carbonate System II

Global carbonate weathering rates

This chapter has been published as: Romero-Mujalli, G., Hartmann, J. and Börker, J., 2018. *Temperature and CO_2 dependency of global carbonate weathering fluxes – Implications for future carbonate weathering research*. Chemical Geology. DOI: 10.1016/j.chemgeo.2018.08.010.

3.1 Abstract

Carbonate weathering and transfer of carbon towards the coastal zone is one of the relevant sinks for atmospheric CO_2, controlled by hydrology, ecosystem respiration, river water degassing, and further factors. Specifically, the connection between the soil-rock system to the river systems and instream processes affecting the weathering product rates remain under-researched. Based on constraints for soil-rock pCO_2, river pCO_2, and an identified dependence of river alkalinity on temperature, this work tested which controls should be considered at global scale to accomplish a more holistic carbonate rock weathering model. Compiled river data suggests that with increasing land temperature, above approximately 11 °C, the amount of instream alkalinity in carbonate catchments decreases due to the temperature effect on the carbonate system, while the converse holds true at lower temperatures. Latter is in accordance with calcite dissolution controlled by soil-rock pCO_2 estimates based on ecosystem respiration. In addition, the type of the weathering system (open, semi-closed to closed system with respect to CO_2) was identified to be highly relevant for global weathering estimations. Open systems seem to be the most dominant boundary condition of calcite weathering in the soil profile. Tropical areas with thick soil layers, however, cause the carbonate weathering system to shift from open to semi-closed or closed system conditions. The findings support that calcite weathering rates in the soil profile are higher than the rates to the ocean transported by rivers. Furthermore, an increase in mean land temperature does not necessarily translate into an increase of lateral weathering rates because it might have an influence on soil development, discharge, CO_2 degassing, soil respiration and calcite dissolution. All these named factors need to be addressed to be able to quantify global carbonate weathering rates and to assess the sensitivity of carbonate weathering rates on climate variability. Future works should focus on collecting more temporal river chemistry data, mainly in tropical regions, to understand the main mechanism causing the observed decrease of alkalinity concentration with temperature.

3.2 Introduction

Chemical weathering is a key component of the processes transferring chemical species from the continents to the oceans (Berner et al., 1983; Walker et al., 1981; Kempe, 1979; Mackenzie and Garrels, 1966). Numerous studies have shown that continental weathering is sensitive to environmental parameters (e.g. temperature, hydrology and vegetation) for a large variety of temporal scales (Calmels et al., 2014; Norton et al., 2014; Egli et al., 2008; White and Blum, 1995). Specifically, the weathering of carbonate minerals, one of the most abundant minerals at the Earth surface (Hartmann et al., 2012; Hartmann and Moosdorf, 2012), shows the highest weathering rates besides evaporites in comparison to most abundant lithological classes

(Moosdorf et al., 2011; Amiotte-Suchet and Probst, 1995; Bluth and Kump, 1994; Amiotte-Suchet and Probst, 1993). Carbonate weathering does not act as a sink for atmospheric CO_2 over geological timescales (Arvidson et al., 2006; Berner et al., 1983; Kempe, 1979). It impacts, however, the distribution of carbon between ocean and atmosphere at timescales below the mixing time of the ocean, shorter than 10^5 years (Martin, 2017; Berner and Berner, 2012). Although mapped sedimentary carbonate rocks cover only 10 to 14% of the terrestrial surface, excluding the area of ice shields (Hartmann and Moosdorf, 2012; Dürr et al., 2005), carbonate rock weathering contributes about 50 % to 60 % to the dissolved products from rock weathering (Gaillardet et al., 1999; Meybeck, 1987). This high proportion is because non-carbonate dominated lithological classes like mixed sediments, siliciclastic sediments, metamorphic rocks and felsic intrusive rocks contribute to carbonate weathering fluxes in addition (Hartmann et al., 2014b). Moreover, it had been estimated that carbonate weathering might be responsible for 34 % to 50 % of the global CO_2 consumption at short time scales (Hartmann et al., 2009; Gaillardet et al., 1999). One of the key processes controlling carbonate weathering rate in carbonate dominated lithologies is the partial pressure of CO_2 (pCO_2) in the soil (Calmels et al., 2014). In this system, organisms play an important role for weathering through the soil profile, concentrating the CO_2 and organic acids and providing more protons for weathering reactions (Kuzyakov, 2006).

In the past, research on global land-ocean carbonate weathering rates focused on the CO_2 uptake by chemical weathering at the global scale (Hartmann et al., 2014b; Hartmann et al., 2009; Dupré et al., 2003; Amiotte-Suchet and Probst, 1995), applying functions based on empirical relationships with runoff, temperature, and soil properties (Hartmann et al., 2014b; Bluth and Kump, 1994; Amiotte-Suchet and Probst, 1993), while others have employed mechanistic models based on kinetic theory, chemical equilibrium and hydrological models, forced by ecosystem numerical models (Goddéris et al., 2013; Beaulieu et al., 2012; Roelandt et al., 2010; Goddéris et al., 2006). Although both types of model approaches aimed to calculate the total weathering rate to the ocean, and the CO_2 consumption by chemical reactions, the two approaches have significant differences. The functions based on observed relationships, phenomenological models, are the most simple and easy to apply in global calculations, e.g. in Earth system models (Goll et al., 2014). However, the principal disadvantage with the current phenomenological models is that generally a constant alkalinity concentration for carbonate weathering is assumed, independent of the temperature and soil-rock CO_2 concentration. On the other hand, the mechanistic models are often more computationally expensive and generally applicable at the local scale (Goddéris et al., 2006), and annual calculations for carbonate weathering are limited due to fast calcite dissolution, which force to decrease the time step for each calculation, while increasing significantly the computational time (Roland et al., 2013).

Furthermore, Gombert (2002) calculated the maximum carbonate dissolution by applying simplified equilibrium equations and a soil-rock pCO_2 function based on annual evapotranspiration from Brook et al. (1983). A soil-rock pCO_2 representation for the averaged conditions in the critical zone provides the ability to address the dynamics of weathering driven by ecosystem respiration. The advantage of using equilibrium equations over kinetics is that its numerical solution reduces the computational time, comparable to those of the application of phenomenological approaches in global weathering models. However, the applied pCO_2 equation based on annual evapotranspiration (Brook et al., 1983) in Gombert (2002) has some disadvantages for low temperature regions and may not address the role of soil water content enough, which is relevant for CO_2 production in the soil system (Romero-Mujalli et al., 2018).

Carbonate dissolution is a dynamic process and variations on timescale of hours are documented as well as fast precipitation depending mainly on the concentration of CO_2 in the aquatic system (Calmels et al., 2014; Pu et al., 2013; Roland et al., 2013; Serrano-Ortiz et al., 2010). Moreover, the kinetics of the reactions involved in carbonate dissolution are fast enough to reach equilibrium in 3 h in laboratory experiments (Dreybrodt et al., 1996; Reddy et al., 1981), implying that in the critical zone (soil-rock) the system could easily reach equilibrium with respect to a given pCO_2. Consequently, the concentration of carbonate weathering products in water leaving the soil-rock-system might be calculated based on equilibrium considerations using information on the soil-rock pCO_2 (Romero-Mujalli et al., 2018).

Pu et al. (2013) studied groundwater in karstic areas and they found that the water was always over-saturated with respect to calcite, and soil CO_2 production was driving seasonal hydrochemical variations in those waters. The highest pCO_2 in water occurred during the warm season. Moreover, Calmels et al. (2014) established that the chemical weathering gradient observed in the Jura Mountains can be explained by spatial variations in the amount of CO_2 in soils. The CO_2 in soils is produced by a combination of different processes, which include microbial activity, root respiration and dissolution of carbonate by acids (Wang et al., 2015; Li et al., 2008; Kuzyakov, 2006; Edwards et al., 1973).

Difficulties while modelling global carbonate weathering may arise because: (*i*) often only calcite dissolution is considered, excluding other minerals that influence weathering fluxes (Gombert, 2002); (*ii*) global approaches do not account for carbonate weathering influenced by strong acids, like sulphuric acid, in general (Torres et al., 2017; Calmels et al., 2014; Beaulieu et al., 2011; Calmels et al., 2007; Spence and Telmer, 2005; Hercod et al., 1998); (*iii*) runoff based functions do not account for differences in soil-rock pCO_2 and temperature (Hartmann et al., 2014b; Amiotte-Suchet and Probst, 1995; Bluth and Kump, 1994); and, (*iv*) anthropogenic perturbations are not accounted in global carbonate weathering models, where application of fertilizers might impact CO_2 consumption by carbonate weathering (Perrin et al., 2008; Semhi et al., 2000).

In order to overcome such limitations and to better understand the role of the carbonate weathering in the Earth system, a set of approaches is compared and evaluated using river chemical data for catchments dominated by calcite dissolution. Approaches used are based on a river alkalinity parameterization (phenomenological approach) and equilibrium equations (mechanistic approach) to calculate the chemical weathering fluxes due to calcite dissolution from carbonate rocks, utilizing different constraining functions to estimate an annually representative partial pressure of CO_2 in the soil-rock system. The influence of additional minerals like sulphides and evaporites on generated alkalinity and calcium concentration is in further discussed, together with the question how does the abundance of open, semi-closed or closed system conditions with respect to soil CO_2 affect the generation of alkalinity fluxes.

3.3 Methods

3.3.1 Hydrochemical database

In order to evaluate calcite weathering fluxes to achieve the named objectives, the Global River Chemistry database (GLORICH) was used (Hartmann et al., 2014a), which combines hydrochemical data with catchment properties and characteristics. The GLORICH database represents over 17,000 sample stations, therefore, a data selection was an imperative step in this work to be able to study only sample stations with a dominant influence from calcite dissolution. A total of 299 sample locations were considered, representing 1798 single samples (Fig. 3.1). The selection was established for idealized conditions of calcite weathering. The following criteria needed to be fulfilled (Gaillardet et al., 2018; Romero-Mujalli et al., 2018):

(i) Samples with $[Ca^{2+}]/[SO_4^{2-}]$ molar ratios larger than 10 were selected to avoid relevant contribution from pyrite oxidation and sulphate minerals dissolution.
(ii) In order to minimize the effect of evaporite dissolution and silicate weathering, samples with $[Ca^{2+}]/[Na^{+}]$ molar ratios larger than 10 were selected, based on Gaillardet et al. (1999) relations and data analysis.
(iii) Water samples with $[Cl^{-}]/[Na^{+}]$ molar ratio < 2 were selected to minimize possible anthropogenic input.
(iv) $[Ca^{2+}]/[Mg^{2+}]$ molar ratio should be higher than 2 in water samples, to minimize contribution of other carbonate minerals besides calcite and to exclude further contribution of weathering of silicate minerals.
(v) Water samples with charge balance error (CBE) < 10 % were chosen, to exclude samples with high uncertainty in reported concentrations.

A correction for rainwater contribution was not possible to apply due to lack of knowledge of the contribution from local rainwater chemistry and dissolution of minerals other than calcite for each sampling location.

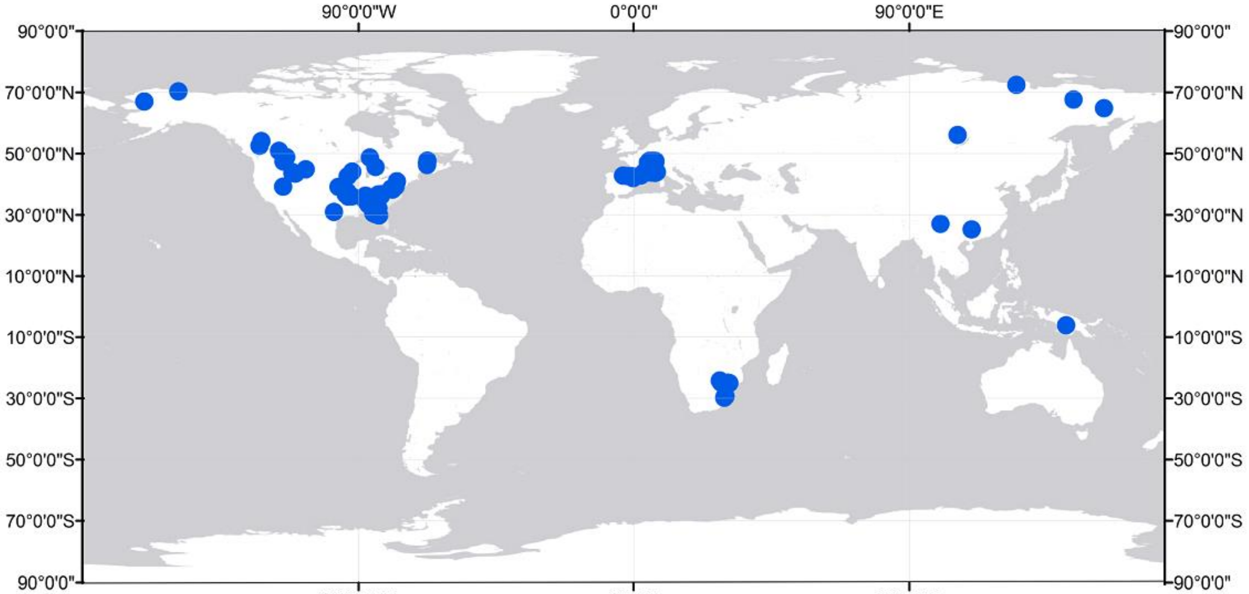

Figure 3.1. Global localization of the 299 selected GLORICH sample stations after applying conditions described in section 2.1. A total of 1798 single measurements are represented.

3.3.2 Alkalinity and pCO_2 parameterizations

In order to study controls on the river weathering rates from calcite dissolution, different approaches to estimate alkalinity were chosen (Table 3.1): (*i*) alkalinity was parameterized using a phenomenological approach and considers the observed alkalinity concentration dependence on temperature, which has a boomerang-shaped curve; and (*ii*) alkalinity was calculated by equilibrium calculations with a given pCO$_2$ and saturation index with respect to calcite (SIc; see Appendix B for details about thermodynamic calculations).

3.3.2.1 River alkalinity parameterization. The boomerang-shaped curve of alkalinity concentration in dependence of mean surface temperature identified for global rivers dominated by carbonate dissolution (Gaillardet et al., 2018) was used to represent carbonate weathering (hereafter as *river_alk*). Alkalinity was parameterized using annual land surface temperature of a catchment and implementing the non-linear Levenberg-Marquardt algorithm for the following function:

$$log_{10}river\_alk = \left(e^{b_1+b_2T+b_3T^2}\right) \tag{3.1}$$

"*river_alk*" is alkalinity in mN (or meq L^{-1}), T is mean annual land temperature (°C). The final parameters b_1, b_2 and b_3 were determined by sampling for each station 1000 times a random value based on mean values and standard deviation for reported alkalinity and temperature (Fig. 3.2) and subsequently estimating each time the b-parameters. The mean and standard deviation of b_1, b_2 and b_3 are -1.73 ± 0.08, 0.28 ± 0.02 and -0.0157 ± 0.0009, respectively. The standard deviation of Eq. 3.1 based on residuals analysis is 0.2 (logarithm of mN) for the 90% confidence level of the fitted function.

3.3.2.2 pCO_2 parameterizations. Different estimates for pCO$_2$ were applied as constraints to calculate alkalinity and calcium concentrations from calcite dissolution in equilibrium with a given pCO$_2$, either for the soil-rock system or within rivers:

1) Atmospheric pCO$_2$ (hereafter as *CO_2atm*) with a value of 0.000398atm was used as a minimum threshold for aquatic pCO$_2$ which is at equilibrium with the carbonate system and representing a minimum baseline for carbonate weathering for comparison.
2) Modelled global river water pCO$_2$ data after Lauerwald et al. (2015) was used to calculate concentrations of chemical species in equilibrium with calcite, assuming that this river CO$_2$ is derived from the soil-rock system and caused observed alkalinity concentrations in rivers. The possibility of CO$_2$ outgassing and secondary calcite precipitation in river will be discussed below. The applied river pCO$_2$ data represents global spatially-explicit estimates of river and stream pCO$_2$ for surface water stream orders of three and higher (hereafter as *global_river_CO_2*). Saturation indices with respect to calcite of 0 and 0.5 were considered to calculate concentrations of chemical species in rivers. The SIc = 0.5 was chosen based on an analysis of the filtered data and is close to the median SIc.
3) Soil pCO$_2$ was calculated after Brook et al. (1983) (hereafter as *soil_aet_CO_2*). This equation depends only on the variables annual evapotranspiration (AET) and atmospheric pCO$_2$ (*CO_2atm*). The equation (Eq. 3.2) was originally constructed using soil pCO$_2$ data from 19 locations at different depths, and is defined as:

$$log_{10}(soil\_aet\_CO_2) = log_{10}(pCO_2atm) + 2.09(1 - e^{-0.00172AET}) \tag{3.2}$$

4) In addition, the function for estimating soil $p\mathrm{CO_2}$ after Romero-Mujalli et al. (2018) was applied (hereafter as *soil_tw_CO₂*) to calculate the concentration of chemical species at equilibrium with calcite. Parameters for the equation (Eq. 3.3) were derived using the Levenberg-Marquardt algorithm for non-linear methods. This equation uses land surface temperature and soil volumetric water content as the main predictor variables for estimating an averaged soil-rock $p\mathrm{CO_2}$.

$$log_{10}(soil\_tw\_CO_2) = \frac{e^{\left(b_1\theta + \frac{b_2}{\theta}\right)}}{(b_3 + e^{b_4 T})} + log_{10}(pCO_2atm) \tag{3.3}$$

Where T is temperature in °C, θ represents the soil volumetric water content ($m^3\ m^{-3}$), pCO_2atm is the partial pressure of CO_2 (atm) in the atmosphere, and in this work a value of 0.000398atm was considered. Fitted parameters b_1, b_2, b_3 and b_4 have values of -3.0, -0.25, 0.09 and -0.34, respectively. The calculated standard deviation for this function is 0.6 ($\log_{10}p\mathrm{CO_2}$).

Table 3.1. Summary of the different settings implemented in this work to calculate global calcite weathering fluxes in rivers and from the soil-rock system at equilibrium with a specific calcite saturation index (SIc).

Nr.	Abbreviation	Estimate	Function	System	SIc	Reference
1	CO_2atm	$p\mathrm{CO_2}$	0.000398atm	Control	0	-
2	*river_alk*	Alkalinity	Eq. (3.1)	River	0	This study (Chapter 3)
3	$river\_CO_2$	pCO2	Global data	River	0 and 0.5	Lauerwald et al. (2015)
4	$soil\_aet\_CO_2$	pCO2	Eq. (3.2)	Soil-rock	0	Brook et al. (1983)
5	$soil\_tw\_CO_2$	pCO2	Eq. (3.3)	Soil-rock	0	Romero-Mujalli et al. (2018)

3.3.3 Global chemical weathering calculations

Global information in gridded format (section 3.3.4) was used to determine spatially-explicitly alkalinity or calcium concentration related to the dissolution of calcite and to calculate weathering fluxes either from the soil-rock system or in rivers (Fig. C.1 in Appendix C). The weathering fluxes are calculated by the following equation:

$$F = C_i * q \tag{3.4}$$

where, F is the alkalinity weathering flux expressed in mmol of C_i $m^{-2}\ a^{-1}$, C_i is the concentration of a chemical species produced by calcite dissolution (calculated as explained in section 3.3.2) in mmol m^{-3} (or meq m^{-3}), and q is the surface runoff in $m^3\ m^{-2}\ a^{-1}$. The alkalinity flux represents the rate of different chemical species (C_i is representing here $[HCO_3^-] + 2[CO_3^{2-}] + [OH^-] - [H^+]$).

The global alkalinity weathering rate (r) is calculated by the following equation:

$$r = \sum_{k=1}^{n} F_k A_k \tag{3.5}$$

where *A* is the area of carbonate sedimentary rocks (SC) in m^2, subscript *k* stands for specific grid-cell, and *n* is the total number of grids in the map. Global weathering rate can be translated to CO_2 consumption (mol C a^{-1}) by using the stoichiometric relations (Eq. B.13), where mole of CO_2 consumed is equivalent to mole of Ca^{2+} in solution.

The obtained alkalinity rates were compared with approaches applying two runoff based phenomenological models (Amiotte-Suchet and Probst, 1995; Bluth and Kump, 1994).

Amiotte-Suchet and Probst (1995) calculate alkalinity rates depending on runoff by:

$$F_{SP} = 3.1692 * q \tag{3.6}$$

where F_{SP} is the alkalinity flux in meq alkalinity m^{-2} a^{-1} and q is the runoff in mm^3 mm^{-2} a^{-1}. This approach considers a constant alkalinity concentration.

The equation from Bluth and Kump (1994) is defined as:

$$F_{BK} = \frac{10^{4.521}(0.1 * q)^{0.934}}{1000} \tag{3.7}$$

where F_{BK} is the alkalinity flux in meq alkalinity m^{-2} a^{-1}. Eq. 3.7 considers a small dilution effect for high runoff values.

3.3.4 Global datasets

The applied global runoff dataset (Fekete et al., 2002) combines observed river discharge information with a water balance model to increase accuracy. The calculations were performed for areas with sedimentary carbonate rocks (SC) as mapped in the GLIM database (Hartmann and Moosdorf, 2012). The global mean annual surface temperature was extracted from Hijmans et al. (2005). Global annual evapotranspiration (AET) in mm a^{-1} and the soil volumetric water content (θ) in m^3 m^{-3} data from the Global Land Evaporation Amsterdam Model (GLEAMv3.0) were used, which consist of a set of algorithms that calculate the different components of terrestrial evaporation based on satellite observations (Martens et al., 2017; Miralles et al., 2011). Global calculations were performed implementing a global resolution of 20km per grid cell.

3.4 Results

About half of the alkalinity from carbonate weathering represents the CO_2 sink due to weathering, applying the selection procedure for data used in the analysis (section 3.3.1). Alkalinity is approximately equal to half the concentration of calcium plus magnesium. As in general only low magnesium concentrations relative to calcium are abundant in the selected samples, alkalinity is used to represent the dissolution of calcite in the further discussion. A detailed analysis of calcium concentrations in rivers and its relation to environmental factors is given in an accompanying publication (Gaillardet et al., 2018).

3.4.1 Temperature and magnesium dependency of river alkalinity

The identified alkalinity concentration in rivers dominated by dissolution of calcium carbonates can be described by a Gaussian function in dependence of land surface temperature (Fig. 3.2). The highest alkalinity concentration is found for temperate climate conditions with a land surface temperature of approximately 11°C.

The used alkalinity approach (Eq. 3.1) is applicable to represent the general temperature dependency of calcite dissolution products found in rivers. However, the presented mean function has a relatively high uncertainty as marked by the red lines due to the large scattering of the mean alkalinity data (Fig. 3.2).

If different selection criteria for the Ca^{2+}/Mg^{2+} molar ratios are used, the effect of Mg^{2+} concentration on the observed scattering of alkalinity becomes evident (Fig. 3.2). Controls on dissolution processes of abundant magnesium rich minerals, like dolomite or silicates, and possibly effects on in-stream carbonate precipitation, produce a different alkalinity pattern than the one indicated by the dissolution of calcite. Choosing water samples with a lower relative magnesium concentration ($[Ca^{2+}] > 2[Mg^{2+}]$ and $[Ca^{2+}] > 5[Mg^{2+}]$) results in a better relationship between calculated and observed mean values for alkalinity, and a tighter boomerang-shaped curve (Fig. 3.2c-f), than water samples with relatively high Mg^{2+} concentration (Fig. 3.2a-b). The best fit for (Fig 3.2c) the case $[Ca^{2+}] > 2[Mg^{2+}]$ is used in further to describe the observed behaviour of alkalinity in dependence on temperature.

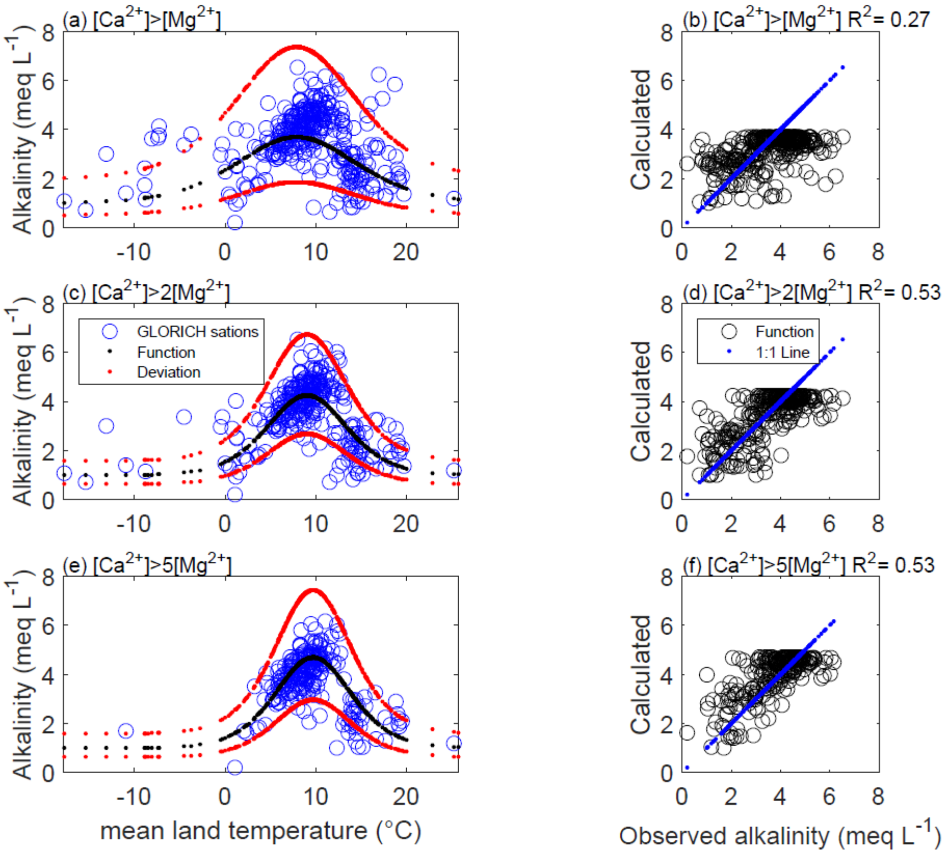

Figure 3.2. Effect of magnesium on the construction of the function (Eq. 3.1) for: (a) and (b) condition of $[Ca^{2+}]/[Mg^{2+}] > 1$; (c) and (d) condition of $[Ca^{2+}]/[Mg^{2+}] > 2$; and, (e) and (f) condition of $[Ca^{2+}]/[Mg^{2+}] > 5$. Plots (a), (c) and (d) are

alkalinity (mN or meq L^{-1}) against mean annual land temperature (°C); and (b), (d) and (f) scatterplots represent the relationship between calculated (Eq. 3.1) and observed alkalinity. Given alkalinity are the mean per sampling location, using 299 catchments.

3.4.2 Temperature and CO_2 control on dissolution of calcite

Applying thermodynamic equations for the system $CaCO_3$-CO_2-H_2O suggest that at constant $p\mathrm{CO_2}$ the concentration of dissolved calcite is indirectly proportional to temperature. Hence, calculated alkalinity reproduces this behaviour when a constant atmospheric CO_2 of 0.000398atm is considered as a baseline scenario for the discussion (*CO_2atm* setting; Fig. 3.3f).

Applying different $p\mathrm{CO_2}$ scenario constraints to calculate river alkalinity due calcite dissolution (scenarios: estimated river $p\mathrm{CO_2}$, Fig. 3.3b; $p\mathrm{CO_2}$ estimated by annual evapotranspiration, Fig. 3.3c; or $p\mathrm{CO_2}$ estimated by surface land temperature and soil water content Fig. 3.3d) does not reproduce the observed alkalinity dependency on temperature based on observations (Fig. 3.3a and e) for the given temperature range.

The closest pattern to the observed alkalinity is the approach using temperature and soil water content to estimate an average soil-rock $p\mathrm{CO_2}$ (*soil_tw_CO_2*; Fig. 3.3c). For this approach chemical concentrations from calcite dissolution are calculated before the water discharges into rivers, because this approach was derived based on spring water samples in karst areas (Romero-Mujalli et al., 2018). However, the estimated alkalinity in high temperature regions (> 12°C) is on average for the *soil_tw_CO_2* approach (green line in Fig. 3.3c) higher than the observed mean alkalinity values from the GLORICH database (Fig. 3.3e) or the predicted ones by the boomerang-shaped alkalinity function, based on a temperature dependency (Fig. 3.3a). This might be because the *soil_tw_CO_2* approach predicts the production of alkalinity in the soil-rock system by design and does not consider other relevant processes affecting the $CaCO_3$-CO_2-H_2O system in the river, e.g. dilution in high runoff areas, CO_2 degassing and calcite precipitation in the river, or the existence of semi to closed system conditions with respect to soil $p\mathrm{CO_2}$ (Zhong et al., 2017; Lauerwald et al., 2015; van Geldern et al., 2015; Bono et al., 2001).

The application of the $p\mathrm{CO_2}$ estimation based on annual evapotranspiration for the soil-rock system (*soil_aet_CO_2*) or river $p\mathrm{CO_2}$ (*river_CO_2*) are not replicating the observed river alkalinity pattern (Fig. 3.3e). Only a weak decreasing trend for elevated temperatures can be observed. The application of two different saturation indices for river $p\mathrm{CO_2}$ (Fig. 3.3b) reveal no different calculated alkalinity pattern, considering the shape and trend, with exception of different resulting concentrations. Considering the applied thermodynamic equation systems for the scenarios in Fig 3.3c to d, temperature does not represent the strongest direct control, but it influences the biological activity and hence the $p\mathrm{CO_2}$ in the soil system.

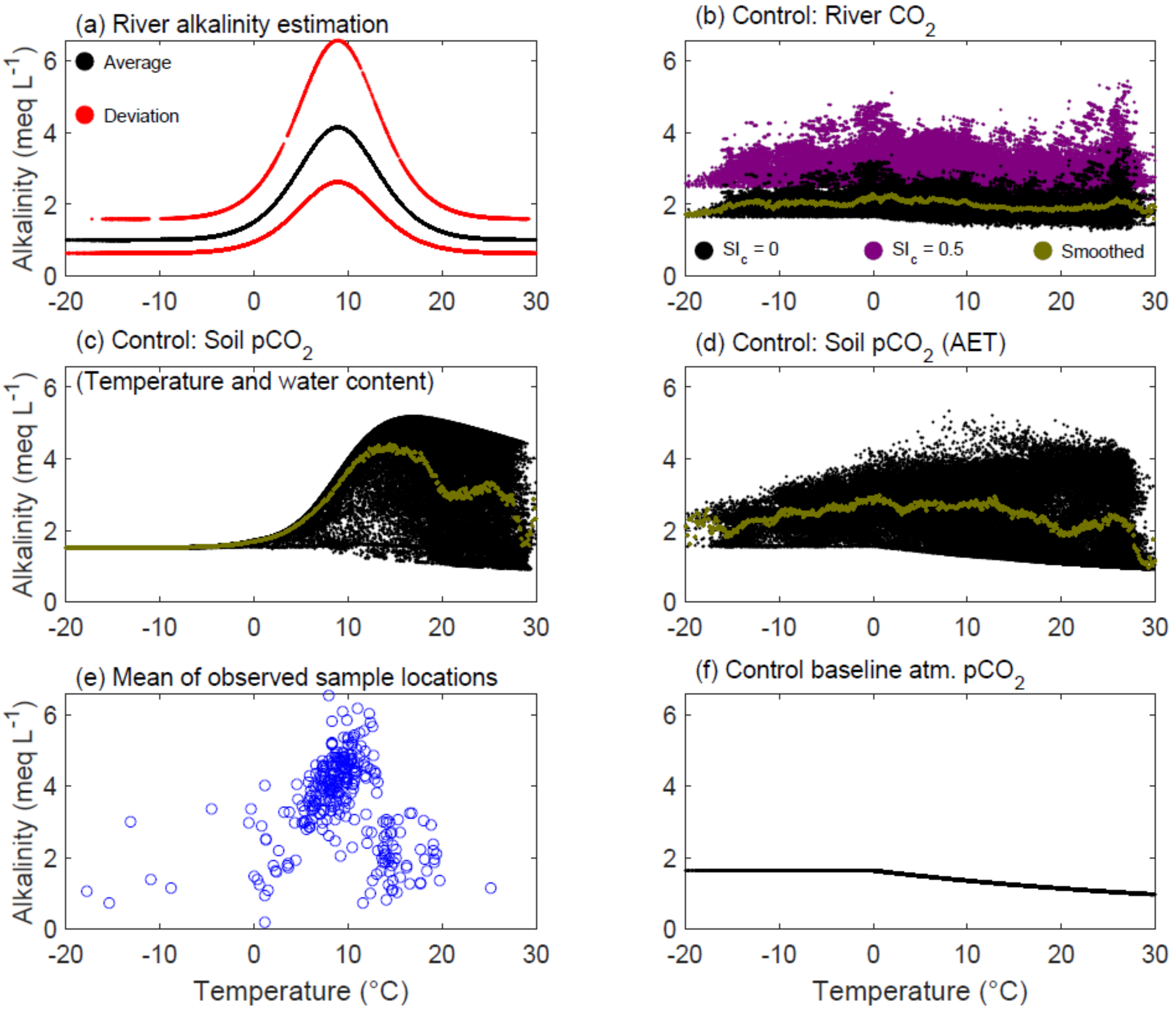

Figure 3.3. Global spatially explicitly calculated alkalinity (meq L-1) against average land temperature (°C) using a 400 km^2 grid cell definition for the scenarios river alkalinity-temperature function *river_alk* (a), and three pCO_2 estimates as constraint (b to d). For *river_CO₂* (b) estimated river pCO_2 and the calcite saturation index (SIc) of 0 and 0.5 are used as constraint. To estimate the soil-rock pCO_2 the constraints temperature and soil water content were used in (c) (*soil_tw_CO₂*) and the annual evapotranspiration rate (AET) in (d) (*soil_aet_CO₂*). Each black point represents a calculation per 400km^2 grid cell (section 3.3.3). For comparison the reference mean values of alkalinity of selected GLORICH sample stations (e), and the baseline scenario using atmospheric pCO_2 as constraint (*CO₂atm*; f) are given. The red points in (a) represent the deviation from the *river_alk* function, and the olive points in (b) to (d) represent the moving averages using a span value of 1°C. The purple points in (b) are the calculated alkalinity values considering a SIc of 0.5, while black points represent the calculation for SIc=0.

3.4.3 Comparing estimate global weathering rates

The different approaches to estimate generated alkalinity concentrations causes for each grid point a different value in the global weathering calculation, and therefore aggregated global rates are different (Fig. 3.4). Calculated global calcite weathering rates are represented as CO_2 consumption rates in Fig. 3.4, comparing the different scenarios with previously used runoff-based functions or phenomenological equations, established by Amiotte-Suchet and Probst (1995) and Bluth and Kump (1994). These latter two approaches, often used in global studies to represent not only calcite but total carbonate weathering rates, produce higher global river alkalinity rates than the baseline calculation (using recent atmospheric $p\mathrm{CO_2}$ as constraint), estimated river $p\mathrm{CO_2}$ (using a calcite saturation index of 0) and the boomerang-shaped function for alkalinity, based on a temperature dependency (considering the mean of the calculations for *river_alk* scenario). The global estimates for the soil-rock system are only slightly higher on average compared to the results from Amiotte-Suchet and Probst (1995) and Bluth and Kump (1994). Two approaches, which allow uncertainty evaluations, show a significant span of possible global rates. Note that the estimates from the previous works were not used here, but new ones recalculated using a homogenized geodatabase to allow comparison of results (Fig. 3.4) for the process discussion below.

The calculated global chemical weathering rates are only related to areas with carbonate sedimentary rocks (labelled SC in the GLIM database), and do not represent rates from mixed sediment areas or trace carbonate rates from other lithological classes (Fig. 3.4). The calculated global rates from mapped carbonate sedimentary rocks are thus lower than total global carbonate weathering rates including further contributing lithologies. The total area of SC used in this work is 10.94 x 10^6 $\mathrm{km^2}$, which is approximately 1% higher than in Hartmann et al. (2014b), but still 7% less than reported by the GLIM database (Hartmann and Moosdorf, 2012). This is because the surface area was calculated from a vector format into a grid format.

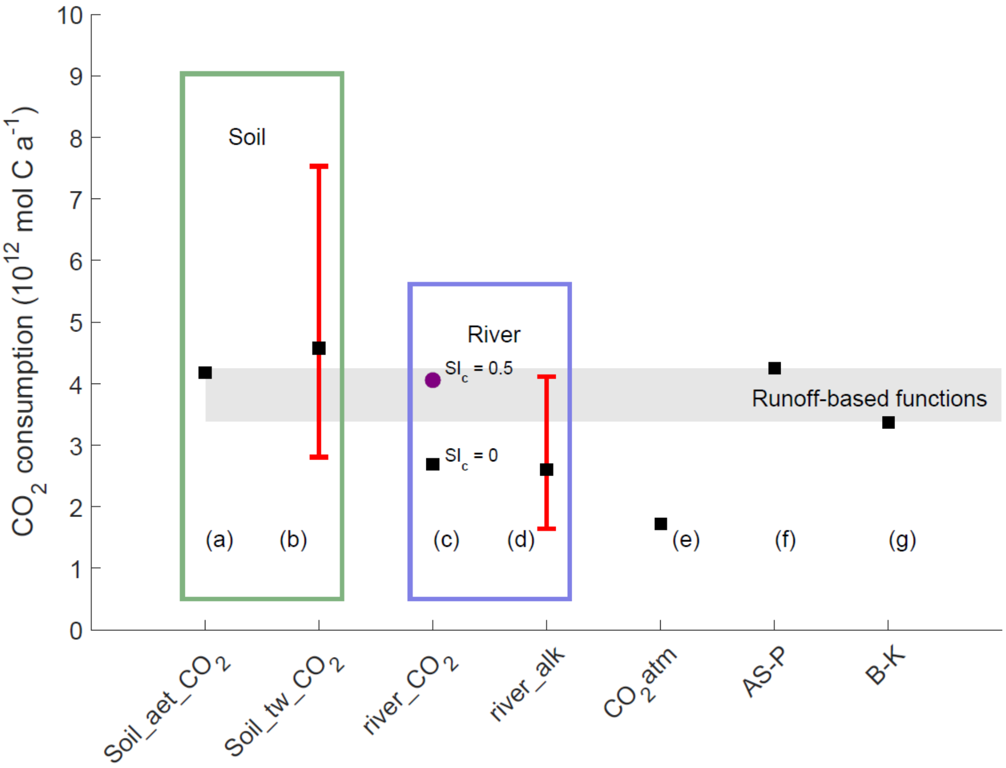

Figure 3.4. Total $\mathrm{CO_2}$ consumption rates (10^{12} mol C a^{-1}) due to global calcite dissolution for different settings: (a) and (b) $\mathrm{CO_2}$ rates due to calcite weathering in soil (*soil_aet_CO₂* and *soil_tw_CO₂* settings, respectively); (c) and (d) $\mathrm{CO_2}$ rates using river settings (*river_CO₂* and *river_alk*, respectively); (e) considering the constant value of 0.000398atm for atmospheric $p\mathrm{CO_2}$ (*CO₂atm*); and, (f) and (g) previous runoff-based functions from Amiotte-Suchet and Probst (1995) and Bluth and Kump (1994), identified as AS-P (Eq. 3.6) and B-K (Eq. 3.7), respectively. The grey rectangle is the interval for previous phenomenological equations AS-P and B-K. Red lines are the maximum and

minimum limits when considering deviation due to residuals for Eq. 3.1 and 3.3. The purple circle represents the total carbon flux when a saturation index SIc = 0.5 is considered for the river $p\mathrm{CO_2}$ estimate.

Comparing calculated fluxes using the mean alkalinity per sampling station with runoff seems to justify the global application of the previous phenomenological models (Fig. 3.5a). However, the available data allow comparison only for a limited runoff range. Approaches using climate sensitive variables show considerable deviation from the phenomenological models, by approximately ± 50% in Fig. 3.5b to 3.5d, and lower deviation for the approach using estimated river $p\mathrm{CO_2}$ as constraint (Fig. 3.5e). This is because the calculated alkalinity concentrations (C_i from Eq. 3.4) vary with temperature, soil water content or evapotranspiration. A significant increase in alkalinity fluxes is calculated when the observed average river saturation index with respect to calcite (SIc) of 0.5 is considered (Fig. 3.7) using river $p\mathrm{CO_2}$ as constraint (Fig. 3.4). This results in an increase of about 50% for calculated global rates, reaching a comparable global value than estimated by runoff-based functions in Fig. 3.4 (AS-P & B-K).

The river $p\mathrm{CO_2}$ data from Lauerwald et al. (2015) is based on climate sensitive parameters like air temperature, net primary productivity (NPP) and a geomorphological component, gradient of slope of a catchment. As this latter catchment property steers the degassing of $\mathrm{CO_2}$, the river $\mathrm{CO_2}$ constraining approach considers a factor directly addressing the potential to precipitate calcite in rivers, and thus lowering the alkalinity fluxes. However, it should be noted that the river $p\mathrm{CO_2}$ estimation is valid only for stream orders larger than two (Lauerwald et al., 2015), and the considerable outgassing from rivers with smaller stream order was not captured here, due to lack of general knowledge in how to parameterized this for small streams at the global scale (Marx et al., 2017). This may in part contribute to the observable difference to the river alkalinity concentration based on observations (Fig. 3.3).

3.4.4 The influence of dilution on global calculations

A further simulation was carried out to study the effect of dilution for high runoff areas on global carbon rates and alkalinity fluxes, because it has been demonstrated that hydrology, besides ecosystem respiration, is a relevant control on the weathering rate from carbonate mineral dissolution in catchments (Zhong et al., 2017). At high runoff, calcite dissolution might not achieve equilibrium and the water will be undersaturated with respect to calcite, or a substantial amount of surface runoff not percolating into the ground is added to the river water. Due to the lack of instant discharge data for a sufficient number of catchments, a comparison with annual runoff is conducted to study first order patterns, which may emerge if dilution would be a relevant factor to be considered. Therefore, a correction coefficient as proposed by Bluth and Kump (1994) was used to calculate a dilution effect on concentrations of chemical species (C_i) with increasing runoff, expressed by the following equation:

$$C_i = \frac{C_{eq}}{q^{0.066}} \tag{3.8}$$

Where C_{eq} stands for the concentration of chemical species i (mol $\mathrm{L^{-1}}$), calculated by equilibrium equations, and q is the runoff ($\mathrm{mm^3\ mm^{-2}\ a^{-1}}$). The dilution parameter of "0.066" was taken from Bluth and Kump (1994) for catchments dominated by carbonate minerals because they have correlated alkalinity with runoff associated to carbonate rocks. Accordingly, a decrease in alkalinity fluxes for increasing runoff can be observed, as expected (Fig. 3.6). Nevertheless, this correction was not applied to the *river_alk* and *river_CO₂* settings because the dilution effect may be already imprinted into the river water composition. An application of the dilution effect would decrease global carbon rates significantly (-34% approximately, Table 3.2), similar to the approaches using river water composition as constraint (*river_alk* and *river_CO₂*). The scenarios with dilution effect result in lower global rates than the scenarios using parameterizations based on Bluth and Kump (1994) and Amiotte-Suchet and Probst (1995). A dilution effect based on annual data is hard to apply, as dilution should happen at the event scale during rainy periods, and would therefore demand a calibration for parameters using event scale data. However, the calculation suggests, that the chosen simple parameterization achieves a plausible effect towards the right direction. Further results discussed below on the open-versus closed system condition (section 3.4.6) suggest that the dilution effect should be weaker, if using annual data as done here.

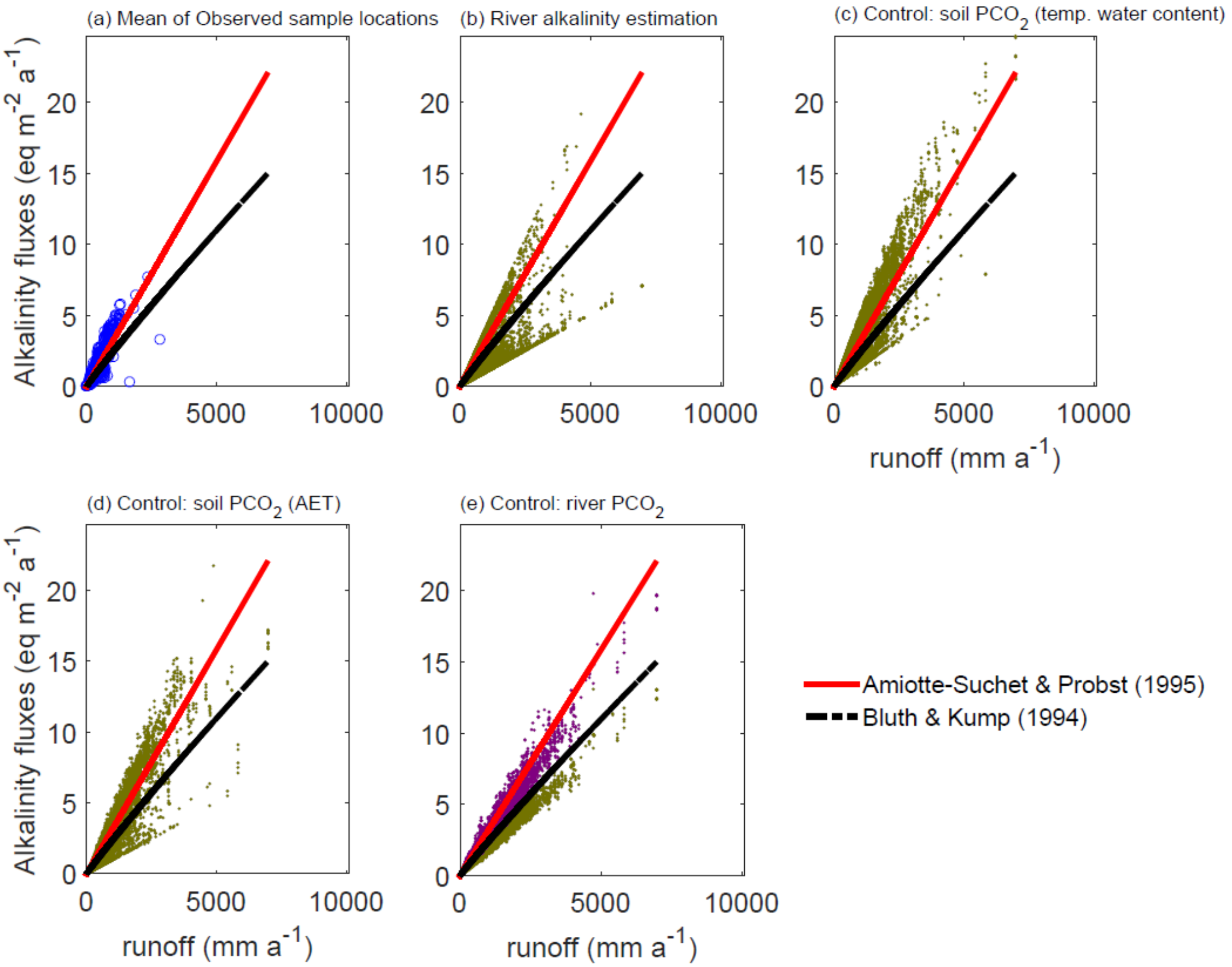

Figure 3.5. Global alkalinity fluxes (eq m^{-2} a^{-1}) against runoff (mm^3 mm^{-2} a^{-1}) calculated using (a) mean values of 299 sample stations in GLORICH database, (b) *river_alk*, (c) *soil_tw_CO₂*, (d) *soil_aet_CO₂*, and (e) *river_CO₂*. Previous phenomenological models based on runoff are represented by the red (Amiotte-Suchet and Probst, 1995) and black

lines (Bluth and Kump, 1994), calculated using Eq. 3.6 and 3.7, respectively. Note that (c) and (d) represent alkalinity rates generated in the soil-rock system, while the other approaches are based on river data. The purple points are the calculated alkalinity values considering a SIc of 0.5.

Table 3.2. Global CO_2 consumption rates associated to modelled calcite dissolution using different approaches based on phenomenological functions and equilibrium equations. The dilution effect was calculated for settings considering pCO_2 constraints for the soil-rock system and the baseline scenario by implementing Eq. 3.8.

Method – Simulation setting	CO_2 consumption (10^{12} mol C a^{-1}). Without dilution effect	CO_2 consumption (10^{12} mol C a^{-1}). Including dilution effect
Amiotte-Suchet and Probst (1995)	4.3	n.a.
Bluth and Kump (1994)	3.4	n.a.
soil_et_CO₂	4.3	2.8
soil_tw_CO₂	4.6 (2.8 – 7.6)	3.0 (1.8 – 4.9)
river_CO₂	2.7 (4.1[a])	n.a.
river_alk	2.6 (1.6 – 4.1)	n.a.[b]
CO₂atm	1.8	1.2

n.a.: not applicable.

a CO_2 rates calculated using SIc = 0.5.

b *river_alk* calculates directly the alkalinity based on relationship with temperature as described by Gaillardet et al. (2018), hence, it might reflect implicitly the dilution effect.

3.4.5 Modelled versus observed alkalinity

Comparing calculated alkalinity mobilization in the soil-rock system (*soil_tw_CO₂* and *soil_aet_CO₂*) with reported alkalinity values in rivers shows a better prediction potential, due resulting soil-rock pCO_2, for the approach using temperature and soil water content as constraint than evapotranspiration (*soil_tw_CO₂* and *soil_aet_CO₂*, respectively). Two different temperature intervals (≥ 11°C and < 11°C) are distinguished to address the maximum of alkalinity in the observed data (Fig. 3.2). The *soil_tw_CO₂* setting underestimates for the low temperature interval (blue points in Fig. 3.6a) observed values systematically by about 1 meq L^{-1}. For elevated temperatures the model tends to produce higher alkalinity values (red points in Fig. 3.6a). This might be in accordance with degassing of CO_2 and subsequent reduction of alkalinity in the river system. However, undersaturated conditions can be observed for some samples in this temperature region (Fig. 3.7). The relationship between modelled and observed values for elevated temperature regions does not improve when a dilution effect is considered, taking the 1:1 line as reference (Fig. 3.6c), and the tendency to underestimate reported values increases. Therefore, a further process, not represented in the model assumptions, might be responsible for overestimation in high temperature regions (see results for open and closed system conditions in the next section).

Calculated alkalinity values using evapotranspiration as constraint (*soil_aet_CO₂*) shows no distinctive relationship with observed values in the GLORICH database, with and without considering a dilution effect (Fig. 3.6b and d, respectively). This indicates that the application of mean annual evapotranspiration to estimated soil-rock pCO_2 (Brook et al., 1983) is not the best selection, based on the data presented in this work. This might be due to the effect of considering different depths during the creation of this soil pCO_2 function (Eq. 3.2), and due to measurements during growing seasons for low temperature regions, affecting the lower limit for mean annual soil pCO_2, were applied (Romero-Mujalli et al., 2018; Brook et al., 1983).

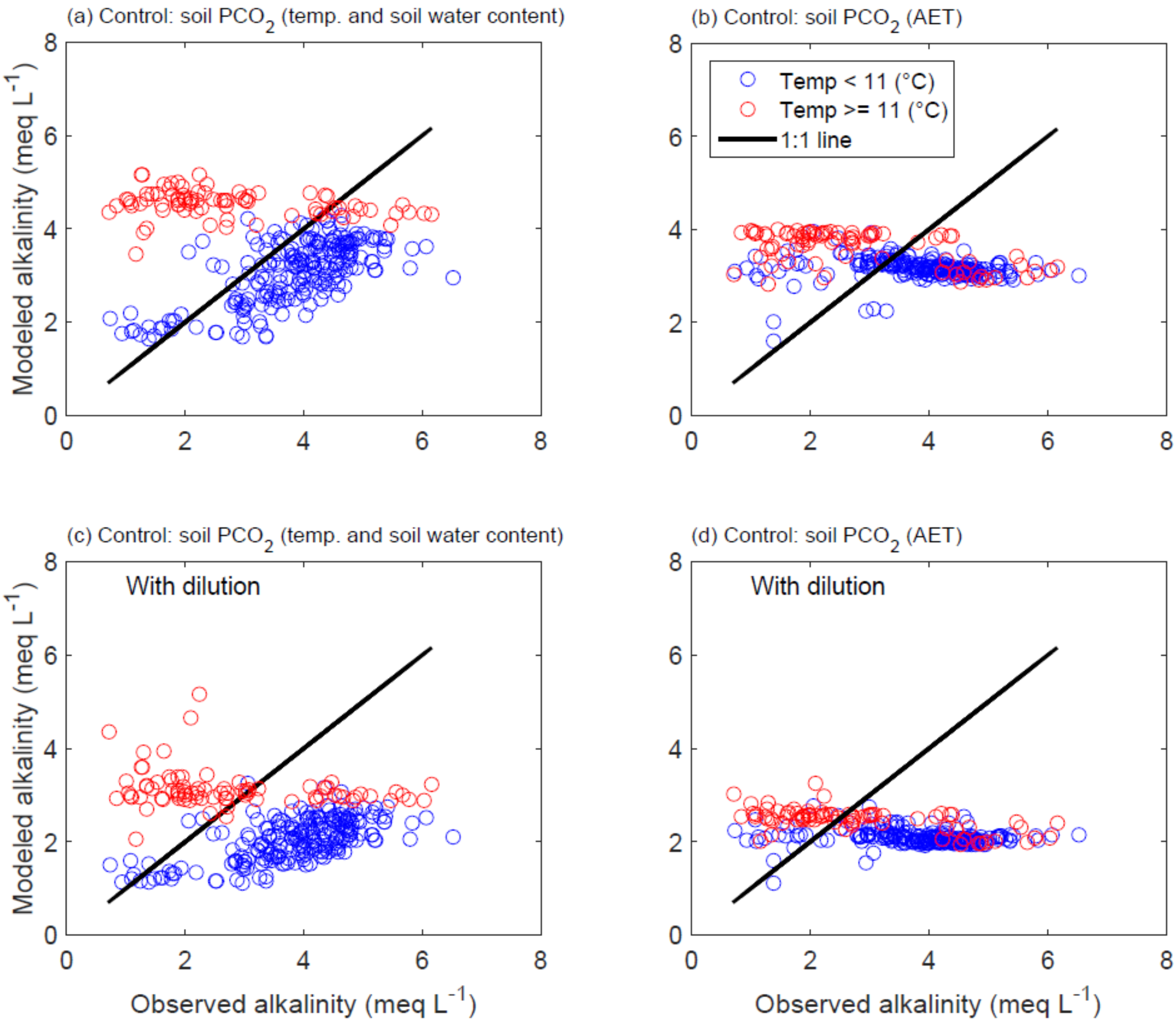

Figure 3.6. Comparison between calculated and observed alkalinity using as a reference the mean values reported for the 299 selected sample stations (Fig. 3.1). (a) *soil_tw_CO₂*, (b) *soil_aet_CO₂*, (c) *soil_tw_CO₂* including dilution, and (d) *soil_aet_CO₂* applying dilution effect. Dilution was applied using Eq. 3.8. The black line represents the ideal 1:1 relationship, red circles are data with surface mean temperature higher or equal than 11°C, and blue circles are data with surface mean temperature < 11°C.

3.4.6 Transition from open to closed system condition with respect to soil pCO_2

Calcite dissolution under closed conditions with respect to a given soil pCO_2 can generate low concentrations of calcium and alkalinity, causing a low saturation index with respect to calcite (SIc), as described by Thrailkill and Robl (1981). The closed conditions are achieved in areas where the water is isolated from the area of soil CO_2 production before reaching an equilibrium with calcite (Deines et al., 1974). Therefore, this condition is probably found in deeper regions of the soil-rock system, where water residence time in the unsaturated zone is less than the time required to reach equilibrium. A global soil depth database was used to evaluate if a systematic bias exists assuming open system conditions. Therefore, the ratio between modelled (using *soil_tw_CO₂* setting) to observed alkalinity was plotted against reported soil depth. The ISRIC-

WISE v3.0 soil database with a half degree resolution was used for this analysis. It is characterized by 45948 unique soil map units, where parameters for each soil unit are estimated using a set of 9600 soil profiles (Batjes, 2005). Extracted values from this database indicate that soils associated with calcite dissolution present, in general, a maximum soil depth < 2m (average of 1m). Calculated alkalinity concentration, under open conditions, using the best representation for soil pCO_2 found in this work (*soil_tw_CO₂*, section 3.4.5), was normalized to observed alkalinity values, and the ratio calculated/observed compared with soil depth for each sample location (Fig. 3.8). Overestimation of calculated alkalinity considering open system conditions tends to increase with soil depths (Fig. 3.8a). This would be expected for a general pattern of a transition from open to closed system conditions with respect to soil CO_2.

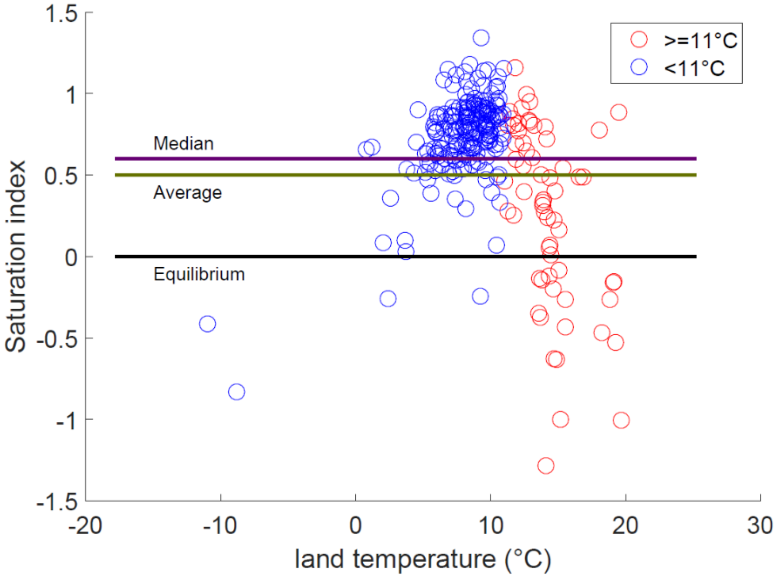

Figure 3.7. Saturation index with respect to calcite (SIc) against mean annual land temperature (°C) for selected 299 GLORICH sample locations. The green line represents the average value, black line is the equilibrium condition (SIc = 0), purple line is the median value and red circles represent the relatively high temperature region (≥ 11°C).

To address the observation, alkalinity was newly calculated assuming open system conditions for soil depth <1.3m and closed system conditions for soil depth >1.3m. In theory, semi-closed conditions can be estimated, but for the purpose of showing the maximum effect, closed system conditions are chosen. Newly calculated alkalinity results in a better approximation compared to observations (Fig. 3.8b). Therefore, soil depth is a parameter that helps to identify conditions for the onset of the transition from open to closed system conditions. Nevertheless, the systematic tendency towards underestimation of river alkalinity using soil-rock pCO_2 estimation is still present. The shape of the scatter plot (Fig. 3.8b) indicates that a systematic bias for the applied *soil_tw_CO₂* function exists. Further studies, applying a larger sample set to retrieve a *soil_tw_CO₂* type function as used in Romero-Mujalli et al. (2018) or improving the soil pCO_2 estimate by including further factors, may lead in the future to better approximations.

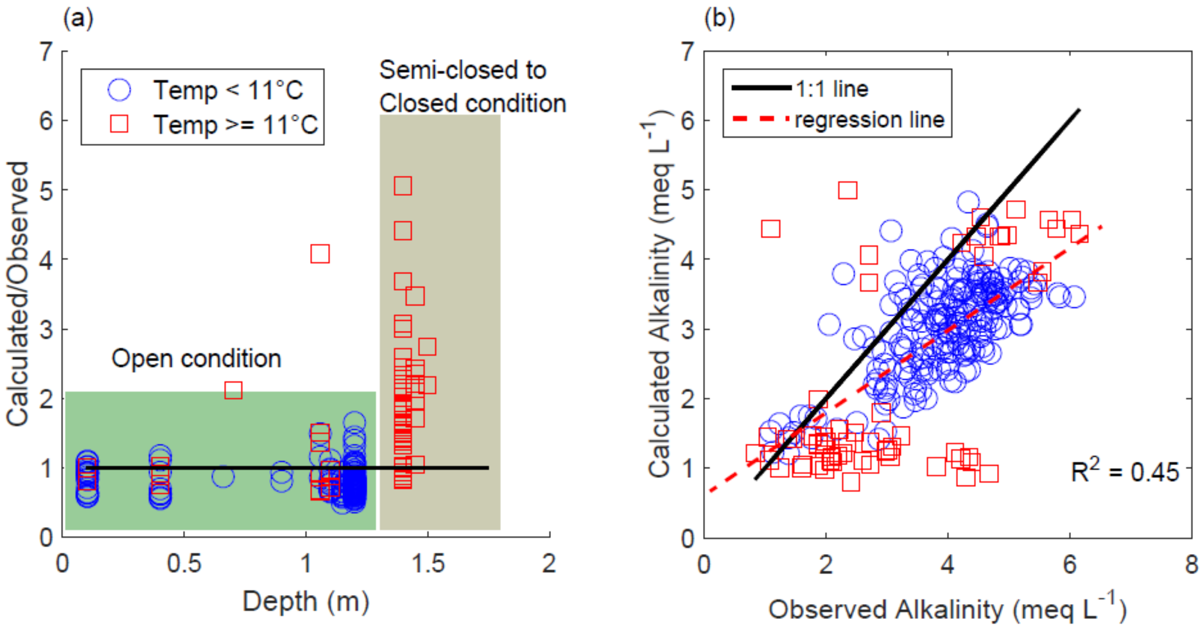

Figure 3.8. Scatter plots showing: (a) alkalinity normalization (Calculated/Observed) against depth, based on ISRIC-WISE v3.0, considering open conditions with respect to CO_2; and (b) calculated against observed alkalinity when closed conditions with respect to CO_2 in deeper soils is included. Alkalinity was calculated using *soil_tw_CO₂* setting (best fit suggested by section 3.4.5) and compared with selected mean values of 299 GLORICH stations. The black line stands for the 1:1 relationship, the red line represents the linear regression with R^2 of 0.45. Shaded regions are the estimated system conditions. A depth of 1.3m was established as the limit between open and closed conditions based on the increasing deviation.

If closed system conditions are assumed for locations with soil depths > 1.3m the calculated global CO_2 consumption would decrease to 1.0 $\times10^{12}$ mol C a^{-1} (applying *soil_tw_CO₂*). This is less than the flux for open system conditions assuming that soil-rock pCO_2 is only equivalent to the atmosphere (*CO₂atm*), with 1.8 $\times10^{12}$ mol C a^{-1}. This result indicates that a transitional zone exists, and the simple two steps model used here is not sufficient for a global application. The calculation suggests that the spatial global abundance of closed system conditions with respect to soil CO_2 is limited. Results indicate that this transitional zone is preferentially abundant in high temperature regions, where thicker soils exist. A spatially-explicit knowledge of where, and under which conditions, the transition towards semi or even closed system conditions appears seems, therefore, a relevant research objective to constrain global carbonate weathering fluxes, specifically in the tropics.

However, the general pattern of river alkalinity can already be replicated with the existing parameterization of the *soil_tw_CO₂* soil-rock pCO_2 function (using a limited available dataset for parameterization), and by using information of open-closed system conditions. The relative systematic underestimation of river alkalinity by about 1meq L^{-1} (Fig. 3.8b) would not allow for further degassing, which can be observed in the rivers (specifically for the temperature range <11°C). An improvement of the soil-rock pCO_2 estimation needs to address this additional effect and would therefore need to produce higher soil-rock pCO_2 values as suggested by the deviation from the 1:1 line considering open-closed-system conditions in Fig. 3.8b.

3.4.7 Seasonal changes

Several studies have demonstrated significant seasonal changes in river chemistry of carbonate rock dominated catchments, mainly due to temperature and discharge changes (van Geldern et al., 2015; Roland et al., 2013; Zhang et al., 2012; Li et al., 2010; Liu et al., 2010; Liu et al., 2007). The selected sample stations (section 3.3.1) show a systematic preferential sampling time in March and September (Fig. 3.9a), and the mean and median alkalinity during these months is higher than during the other sampled months (Fig. 3.9b). Nevertheless, the mean alkalinity is slightly affected by this preferential sampling, from 3.2meq L^{-1} to 3.0meq L^{-1} when samples from March and September are excluded.

The shown underestimation of modelled alkalinity that is shown in the previous section, of approximately 1meq L^{-1} in regions with temperature <11°C, suggests that the soil-rock $p\mathrm{CO}_2$ function by Romero-Mujalli et al. (2018) presents a systematic bias of -1meq L^{-1}. This bias might be influenced by seasonal changes and preferential sampling time of the springs used to calibrate the soil-rock $p\mathrm{CO}_2$ function based on temperature and soil water content. However, seasonal changes could not be considered in the construction of Eq. 3.3, also due to the lack of temporal data for a large enough number of monitoring locations (Romero-Mujalli et al., 2018). Therefore, seasonality or other undiscovered causes may add to the observed systematic underestimation.

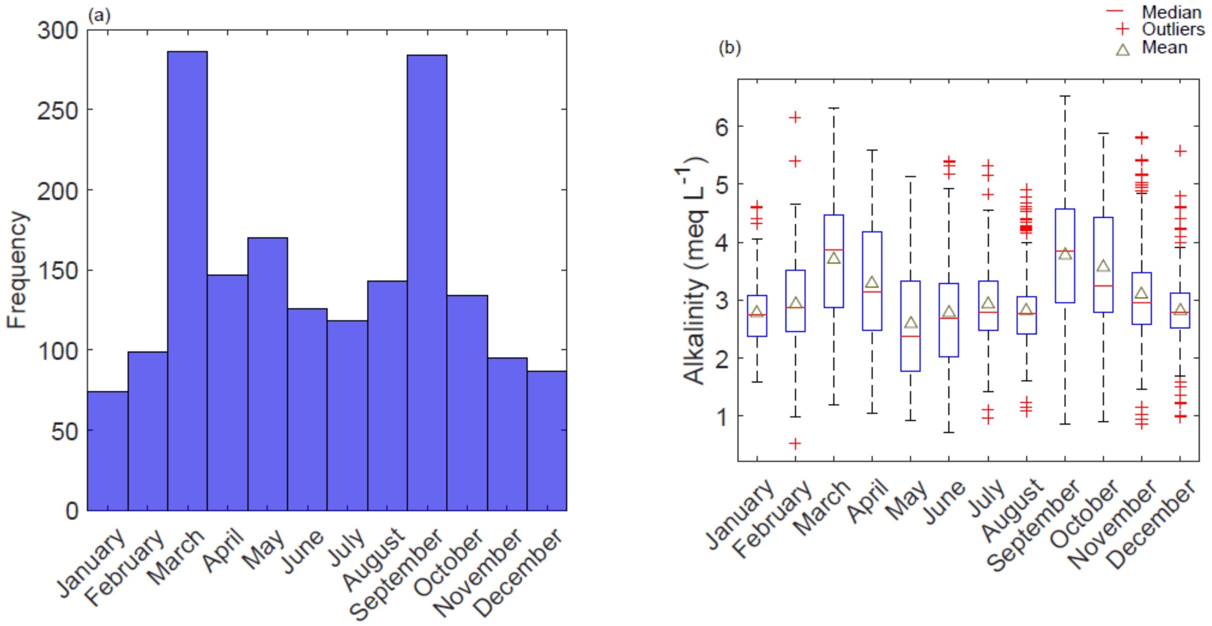

Figure 3.9. Monthly data of 1798 single measurements from 299 GLORICH sample stations (section 3.3.1). (a) Histogram of months sampled showing the preferential months; and, (b) box-plot of alkalinity grouped by months. Monthly data of 1798 single measurements from 299 sample stations.

The sampling period of the selected 1798 samples from the GLORICH database ranges from May of 1963 until November of 2010. The temporal analysis shows an increase of alkalinity and Ca^{2+} + Mg^{2+} concentrations since at least 2001 (Fig. 3.10a and 3.10b, respectively). Temporal variation of water temperature (Fig. 3.10c) does not present a clear relationship with alkalinity or Ca^{2+} + Mg^{2+} concentrations besides seasonal changes during the late 1980s. In addition, the data filtering method implemented in this work reduces the input of evaporites, sulphides, silicates, and anthropogenic sources. Observed temporal variations of the chemical composition in the total dataset may reflect differences in soil-rock *p*CO_2, linked to variations in soil respiration. The soil-rock *p*CO_2 directly reflects the soil temperature and water content where the dissolution of calcite takes place and is not necessarily represented by water temperature of the river (Romero-Mujalli et al., 2018; Kuzyakov, 2006; Mielnick and Dugas, 2000; Amundson and Davidson, 1990).

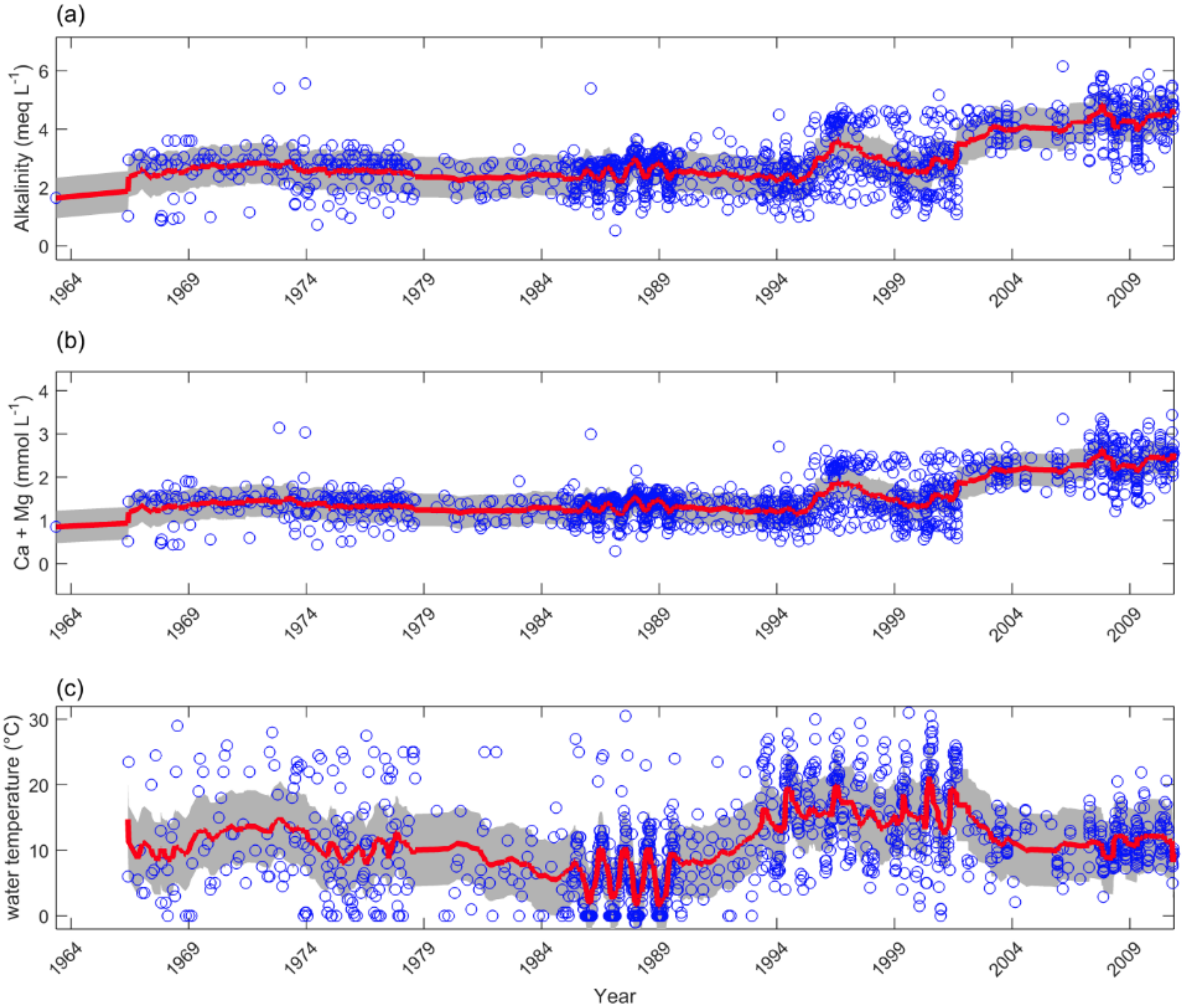

Figure 3.10. Temporal variations of (a) Alkalinity, (b) $Ca^{2+} + Mg^{2+}$, and (c) water temperature of selected 1798 single measurements of GLORICH database. Blue circles represent each sample, red line is the smoothed function based on moving average, and, shaded region is the standard deviation of the smoothed function. Temporal data represents latitudes higher than 30°N due to lack of tropical samples (Fig. 3.1).

3.5 Discussion

Carbonate weathering rates and lateral river rates of the products depend on a combination of processes and system properties, which were tested for their relevance using hydrochemical information from catchments dominated by calcite dissolution, while focusing on alkalinity fluxes. The most prominent control in the critical zone is the soil-rock *p*CO_2, which is supplied by ecosystem respiration, which in turn depends on climate sensitive constraints like soil water content and temperature (Romero-Mujalli et al., 2018). The amount of CO_2 available for the dissolution process is in further controlled by the openness of the system. Semi-enclosed to closed system conditions reduce the weathering rate substantially. Further temperature dependent degassing of CO_2 from rivers (Lauerwald et al., 2015; van Geldern et al., 2015), also controlled by geomorphological properties, causes the average river water to be supersaturated with respect to calcite. The majority of investigated rivers have a saturation index with respect to calcite between 0.5 and 1, and alkalinity loss due precipitation of carbonates is observed in general (Calmels et al., 2014; Li et al., 2008; Liu et al., 2007), but difficult to constraint based on available global data. A rain event specific dilution parameterization maybe relevant for a global climate sensitive carbonate weathering representation, but its relevance and influence needs still to be worked out for the global scale. Simple phenomenological models based on average concentration-runoff relationships seem, for low runoff conditions, to properly address calcite weathering rates. However, rain event scale introduced variability cannot be replicated using the limited global datasets available. An enhanced global carbonate weathering model approach, therefore, should address at least the named processes, while parameterization of these processes for a spatially explicit global application demands further work and specifically more groundwater, spring water, and river water data along the lateral pathway of weathering product rates.

The presented results are based on selected data to represent idealized calcite catchments through minimizing the effect of sulphide oxidation, evaporite dissolution and dolomite contribution. The effects of these neglected minerals and related processes will be discussed below.

Two different approaches for soil pCO_2 estimates were considered in this work to constraint calcite dissolution rates, and both type of estimates present clear differences, mainly in deserts and polar regions (Romero-Mujalli et al., 2018). The function based on annual evapotranspiration (Eq. 3.2) was developed using measurements of soil pCO_2 at different depth and during growing seasons for temperate areas, which causes elevated average soil pCO_2 representations in polar regions. On the other hand, the function based on land temperature and volumetric water content (Eq. 3.3) is conceptually in concordance with ecosystem respiration models and it was created using spring water samples from catchments dominated by calcite dissolution.

The introduced approach calculating alkalinity concentrations based on a representative soil-rock pCO_2 ($soil\_tw\_CO_2$) for open system conditions allows to connect indirectly ecosystem respiration with calcite weathering rates. This work showed that for certain tropical areas, specifically such with deeper soil depth, >1.3m, a transition from open to semi- or even closed system conditions should be considered. However, concepts to address the locations where this happens, and how to represent this transition remain to be elaborated and depends on high quality soil maps. In addition, it was shown that the soil-rock pCO_2 representation demand further work to avoid underestimation of alkalinity concentration (Fig. 3.8b) if the weathering rates should be constraint dynamically by a soil-rock pCO_2 and not a simple river alkalinity parameterization based on temperature (Fig. 3.2). A coupling of carbonate weathering models with ecosystem models might be a further next step, if ecosystem respiration can be replicated properly. The analysis here suggests that evaluation of such coupled models need to include the soil properties and therefore a good representation of the soil-rock hydrology.

3.5.1 Equilibrium approach for calcite dissolution

The applied equilibrium model is constrained by a given pCO_2 and allows the calculation of major chemical species at equilibrium with the system $CaCO_3$-CO_2-H_2O for any given specific temperature. Therefore, the approach might be applied to calculate global calcite weathering from areas dominated by calcium carbonates for the present time and probably over time as it is sensitive to climate variables. However, carbonate rocks are rarely pure calcite. Dolomite ($CaMg(CO_3)_2$) dissolution has a different dissolution rate than calcite and the global pattern of river alkalinity in dependence of temperature changes with the Mg^{2+} concentration relative to Ca^{2+}. Higher alkalinity concentrations are observed in samples with relatively high Mg^{2+} content, in particular in some catchments with elevated temperatures (Fig. 3.2). This might be related to its influence on carbonate precipitation in rivers, because Mg^{2+} can inhibit or delay the precipitation of calcite minerals considering the saturation state of the water (Berner, 1975).

Some studies (Liu et al., 2005; Dreybrodt et al., 1996) have demonstrated that the dissolution of CO_2 in water represents the slowest rate of reaction in the open system $CaCO_3$-CO_2-H_2O. Therefore, it is feasible to consider that a soil-rock system is at equilibrium with calcite for open system conditions (Romero-Mujalli et al., 2018). This might represent an advantage over estimating a simplified soil pCO_2 function based on annual evapotranspiration (*soil_aet_CO₂*).

Being less computationally expensive than chemical kinetic models, further improvements to constrain land to river weathering fluxes might result into incorporation into Earth system models (Goll et al., 2014). Because alkalinity is usually higher in groundwater than in surface waters due to degassing of CO_2 and precipitation of carbonates (Calmels et al., 2014; Li et al., 2008; Liu et al., 2007) further improvements in predicting mineral precipitation and CO_2 outgassing will allow to model sink terms during the transport.

3.5.2 Open and closed system conditions

Although studies related to spring water chemistry in karstic regions have found that the dissolution of carbonate minerals happens mainly under open to semi-open conditions with respect to soil pCO_2 (Romero-Mujalli et al., 2018; van Geldern et al., 2015; Calmels et al., 2014; Gillon et al., 2009), information from tropical regions where soils are usually more developed than in temperate regions is underrepresented. Nevertheless, for specific soil profiles, carbonate minerals are dissolved under closed system conditions with respect to soil pCO_2 (Frisia et al., 2011; Faulkner, 2006; Thrailkill and Robl, 1981; Deines et al., 1974).

The results obtained in this work showed that dissolution of calcite in soils might be developed under a gradual transition from fully open to closed system conditions because the kinetics of dissolution is fast enough to reach equilibrium with calcite before water infiltrates further into the soil profile, where soil production is limited. Soil depth seems not to be a good sole predictor for this transition, but a good one to determine, for a given setting, the start of the transition. A spatially-explicit description of the calcite weathering front, the depth of maximum calcite dissolution, combined with changes of soil CO_2 production with depth are required to constrain the transition of the system's condition of a catchment.

3.5.3 Ideal calcite and real carbonate weathering system

In the present work, equilibrium calculations were developed to solve the ideal system $CaCO_3$-CO_2-H_2O, which allows to determine the chemical species due to calcite weathering. Nevertheless, in the natural system this is not often the case, instead, a complex system is more commonly found where water might be at equilibrium with other minerals, with consequences on the concentration of chemical species. Minerals commonly associated to carbonate lithologies are, e.g., evaporites and sulphides. These minerals produce different deviations from the ideal calcite equilibrium, increasing or decreasing concentrations of chemical species in the water.

Gypsum and anhydrite ($CaSO_4.2H_2O_{(s)}$ and $CaSO_{4(s)}$, respectively) are commonly found in evaporite containing lithologies and both show high solubility in water. A system at equilibrium composed of $CaCO_3$-CO_2-H_2O-gypsum/anhydrite would have approximately 40% less alkalinity if compared to the ideal calcite weathering system (Romero-Mujalli et al., 2018). However, the calcium ion (Ca^{2+}) concentration increases significantly, being able to reach 5 times the concentration presented in the ideal $CaCO_3$-CO_2-H_2O system. This is a consequence of the common ion effect produced by Ca^{2+}, which is shared between two chemical reactions, represented by Eq. B.5 and the gypsum dissolution represented by the following chemical reaction:

$$CaSO_4x2H_2O_{(s)} \leftrightarrow Ca^{2+}_{(aq)} + SO^{2-}_{4(aq)} + 2H_2O_{(l)} \tag{3.9}$$

Furthermore, evaporite minerals like halite ($NaCl_{(s)}$) or sylvite ($KCl_{(s)}$) differ from the effect of gypsum by controlling the ionic strength (I), thus the activity coefficients (Eq. B.12). Elevated contribution of dissolved NaCl to the water enhances calcite dissolution with reference to the ideal calcite weathering (by approximately 40-50% in the given example in Fig. 3.11).

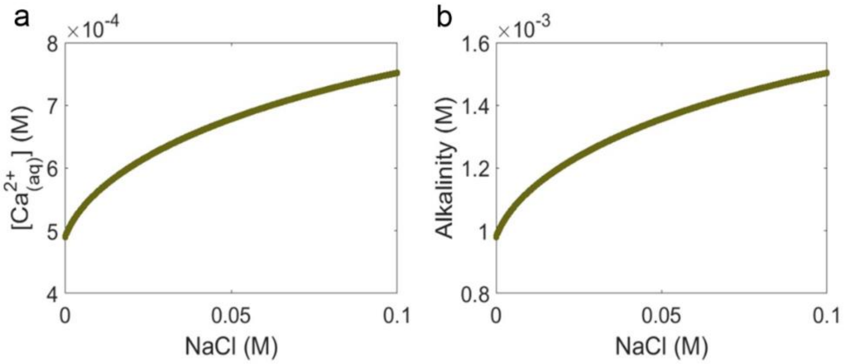

Figure 3.11. Dependency of (a) Ca^{2+} (molar concentration) and (b) alkalinity (equivalent) on halite concentration for the open system NaCl-$CaCO_3$-CO_2-H_2O at 25°C and pCO_2 of 0.000398atm. Relationship as a result of Davies equation for activity coefficient (Eq. B.12).

Sulphide minerals are commonly found in sedimentary rocks and are easily oxidized in the soil profile (Li et al., 2008; Calmels et al., 2007), releasing sulphuric acid (H_2SO_4), a strong acid which may be neutralized by reactions with carbonates, as represented by the following chemical reaction:

$$2CaCO_{3(s)} + H_2SO_{4(aq)} \rightarrow 2Ca^{2+}_{(aq)} + SO^{2-}_{4(aq)} + 2HCO^{-}_{3(aq)} \tag{3.10}$$

This reaction increases carbonate weathering significantly. However, the Ca^{2+}:Alkalinity molar ratio in this system can be 1:1, or even be lower. Therefore, calcite dissolution due to strong acids is not necessarily related to increasing alkalinity fluxes as compared to an ideal calcite dissolution, where the Ca^{2+}:Alkalinity ratio is 1:2. Sulphate ion concentration coming from pyrite oxidation might reach 0.5mM (Li et al., 2008; Calmels et al., 2007). If comparing the concentration differences between the system $CaCO_3$-H_2O-CO_2-FeS_2-O_2 and the ideal carbonate dissolution ($CaCO_3$-H_2O-CO_2), due to the pyrite oxidation two different effects on Ca^{2+} and alkalinity can be expected. The Ca^{2+} concentration would be elevated by up to 20% if compared to the ideal calcite equilibrium calculation when reacting 0.267mM of FeS_2 (Fig. 3.12a). Alkalinity, on the other hand, shows a decrease of approximately 5% with respect to the ideal calcite dissolution (Fig. 3.12b). In both cases, the decreasing trend with temperature follows the dissolution of pure calcite (Fig. 3.12).

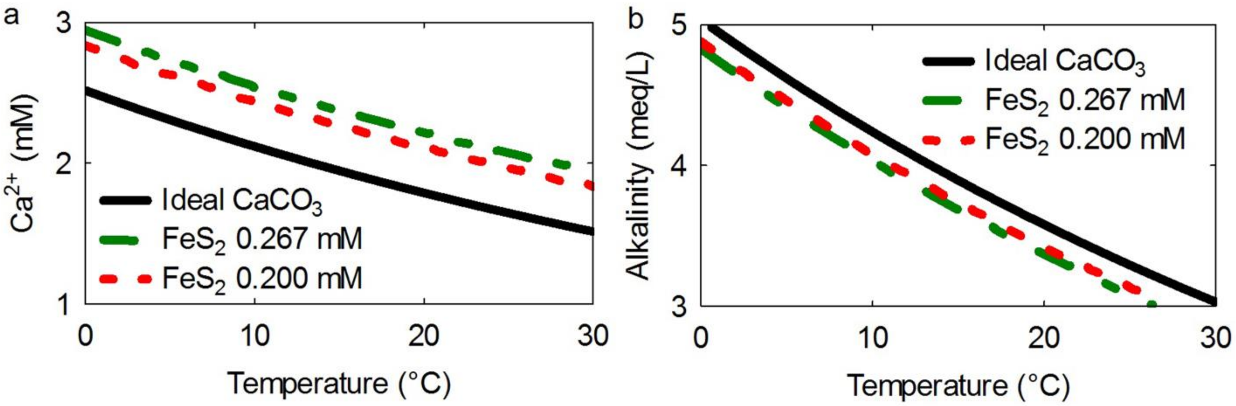

Figure 3.12. Theoretical calculations of (a) Ca2+ concentration and (b) alkalinity against temperature. The black line represents the ideal carbonate equilibrium, the green dash line and red dash line stand for the system $CaCO_3$-H_2O-CO_2-O_2-FeS_2 with pyrite concentration of 0.267mM and 0.200mM, respectively. Results were obtained using the software PHREEQC with "wateq4f.dat" database (Parkhurst and Appelo, 1999) considering a constant pCO_2 of 0.01atm.

Sedimentary carbonate rocks can contain a wide variety of different carbonate minerals, presenting each different dissolution kinetics and solubility. The range of Mg content in Ca-carbonates can vary significantly. Dolomite ($CaMg(CO_3)_2$), another common carbonate mineral, may influence calcite dissolution by adding Ca^{2+} and CO_3^{2-} to the solution (common ion effect). And although its dissolution is slower than calcite (Liu et al., 2005; Chou et al., 1989) and the calcite saturation state can be reached faster, the constant dissolution of dolomite can increase alkalinity in the solution and decrease Ca^{2+} while increasing Mg^{2+} to a Ca/Mg molar ratio closer to the one present in dolomite. We have tested a hypothetical example where the solution is at equilibrium with both minerals (calcite and dolomite saturation indices are 0) and solving the system using the software PHREEQC with "wateq4f.dat" database (Parkhurst and Appelo, 1999). The results show that Ca^{2+} decreases with respect to a solution at equilibrium with only calcite by approximately 40% for the given temperature range in Fig. 3.13a. However, the behaviour of alkalinity is contrary, increasing up to 30% with respect to a solution without dolomite for the considered temperature range (Fig. 3.13b). Moreover, the dolomite effect is more complex than the results obtained by the hypothetical test because Mg^{2+} can enhance calcite dissolution rate under certain conditions (Ruiz-Agudo et al., 2009), and it might increase calcite solubility by increasing ionic strength.

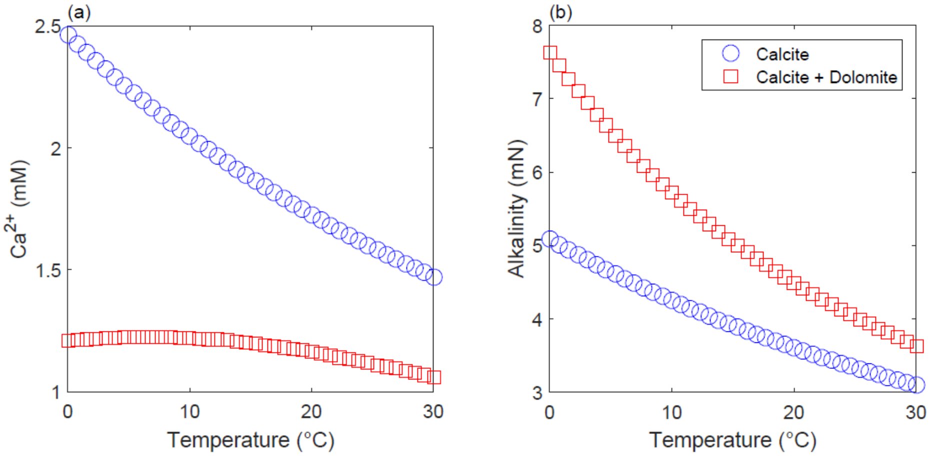

Figure 3.13. Theoretical calculations of (a) Ca^{2+} concentration and (b) alkalinity against temperature. Blue circles represent the ideal carbonate equilibrium and red squares stand for the system $CaCO_3$-$CaMg(CO_3)_2$-CO_2-H_2O. Results were obtained using the software PHREEQC with "wateq4f.dat" database (Parkhurst and Appelo, 1999) considering a constant pCO_2 of 0.01atm.

The relatively low weathering rate of silicate minerals limits its impact on calcite dissolution. For instance, when weathering of anorthite is promoted by carbonic acid, it can increase Ca^{2+} and alkalinity with a similar Ca^{2+}/alkalinity ratio than expected for pure calcite dissolution. However, the dissolution of calcite tends to decrease with temperature, while being opposite for silicate minerals, increasing with higher temperature.

In summary, three main different effects, the common ion effect, ionic strength change and reaction with strong acids need to be considered spatially explicitly to properly model the land-ocean alkalinity fluxes from a carbonate-dominated catchment. These effects show definite deviations from the ideal calcite dissolution system, summarized in Table 3.3. Ca^{2+} concentration presents a positive deviation for the three settings, highlighting the necessity to correct for these effects in order to consider equilibrium equations for ideal calcite dissolution. However, alkalinity behaves differently than Ca^{2+}; its concentration decreases in case sulphide and gypsum minerals are present in carbonate rocks, and it shows a directly proportional dependency on ionic strength.

Table 3.3. Ca^{2+} concentration and alkalinity deviations from the ideal system of carbonate dissolution due to different effects. The mean of deviations for the temperature range from 0 to 30°C is given.

Effect	Deviation on Ca^{2+}	Deviation on alkalinity
Common ion effect (Gypsum)[a]	+400%	-40%
Ionic strength (NaCl)[b]	> +40%	> +40%
Strong acids (FeS_2 oxidation)[c]	+20%	~ -5%
Dolomite ($CaMg(CO_3)_2$)[d]	~ -40%	~ +30%

a. Gypsum Saturation index = 0; Calcite saturation index = 0 and; pCO_2 = 0.01atm.
b. NaCl = 0.1 M; Calcite saturation index = 0 and; pCO_2 = 0.000398atm.

c. FeS_2 = 0.267M; Calcite saturation index = 0 and; pCO_2 = 0.01atm.
d. Dolomite saturation index = 0; Calcite saturation index = 0 and; pCO_2 = 0.01atm.

3.5.4 Anthropogenic effects

Anthropogenic activity was identified to shift geochemical baselines of larger river systems over decades (Raymond and Hamilton, 2018; Hartmann et al., 2007). Carbonate weathering system are due the fast dissolution kinetics very sensitive to anthropogenic influences (e.g. elevated levels of nitric acid or sulphur oxides). Li et al. (2008) have found that 40% of sulphuric acids in soils in Southwest China are related to anthropogenic activity. Furthermore, the use of fertilizers on soils may enhance carbonate weathering, for instance, the addition of N-fertilizers on soils may produce strong acids which can react with carbonate minerals and alter the carbon consumption (Perrin et al., 2008; Semhi et al., 2000) similar as the reaction through pyrite oxidation (section 3.5.3). The application of fertilizers was found to decrease the contribution of soil CO_2 to riverine alkalinity by about 7–17% for studied catchments (Perrin et al., 2008). In addition, anthropogenic effects may control the precipitation rates of calcite in rivers due to phosphate inhibition (Zhang et al., 2012; Bono et al., 2001; Dove and Hochella, 1993).

The use of karstic lands for agriculture or logging activities alters water quality, and changes the natural ecosystem functioning, which might cause an increase of soil degradation and erosion, e.g. due to an increase in surface runoff. The restoration of natural ecosystems on karst regions can take longer than for other land types (Milanović, 2014; Urich, 2002).

On the other hand, the addition of Ca and Mg carbonates (mainly calcite and dolomite) to soils, or liming, is a common agricultural practice to increase pH as well as Ca and Mg bioavailability (Moreira and Fageria, 2010; Diamond et al., 1992). This activity can enhance, for areas other than karst regions, global carbonate weathering fluxes. The potential carbon sequestration due to agricultural liming has been estimated to be around 0.15×10^{12} mol C a^{-1} for soils located in United States of America (Hamilton et al., 2007). This is 3 to 4% of the global carbon rates from sedimentary carbonate rock areas calculated in this work with the idealized calcite weathering approach. However, this carbon sequestration potential depends also on the applied amount of fertilizers resulting in acid production, as discussed above.

3.5.5 Future work for a more holistic carbonate weathering approach

Global CO_2 consumption due to calcite dissolution can be difficult to predict because temperature can exert different effects on the system $CaCO_3$-CO_2-H_2O. For instance, calcite can precipitate in the soil profile in warm and dry conditions, decreasing total weathering flux, as suggested by Goddéris et al. (2013). Moreover, the CO_2 evasion from rivers increases significantly with temperature (Lauerwald et al., 2015), and is one control on the calcite precipitation in the river bed, reducing the total carbon flux to the ocean. Locations and rates, where and at which saturation state this happens considering stream water velocity, biological activity, seasonality or street salt application (Szramek and Walter, 2004; Zaihua et al., 1995; Dreybrodt et al., 1992; Suarez, 1983; Rupp and Adams, 1981), need to be determined for parameterization in a global model approach.

The function for alkalinity concentrations in dependence of land surface temperature is best representing the general dynamics of observed concentrations in rivers, but shows, based on the available data, large uncertainties. The approach could be enhanced by compiling more data, specifically from tropical regions, covering seasonality and in addition instant discharge information. An enhanced approach might include the identification of temperature depending alkalinity for different [Ca^{2+}]:[Mg^{2+}] ratios (Fig. 3.2) and considering ranges of evaporite and sulphide contributions (among other characteristics like catchment size, steepness of the catchment, etc.). Tropical humid areas are of certain interest, due to the high contribution to global weathering fluxes, but also because there are still not enough constraints on the tropical settings (c.f. Fig. 3.8). However, it was shown that by coupling weathering and degassing processes with soil-rock properties, including a soil-rock pCO$_2$ constraint, a more holistic approach could be achieved in the future.

Thermodynamic equations can be implemented to estimate global CO_2 consumption due to carbonate weathering. However, the spatially-explicit mineralogical composition of carbonate systems is required to improve the presented idealized model. The different approaches presented in this work are able to assess the weathering of calcite composed carbonate sedimentary rocks (SC), and do not account for carbonate dissolution from other lithological classes, which contribute relevantly to global carbonate weathering fluxes (Hartmann et al., 2014b; Hartmann et al., 2009). Their contribution is needed to explain the high proportion of calculated global CO_2 consumption by carbonate weathering on the total global CO_2 consumption by weathering, using inverse methods (Gaillardet et al., 1999).

In a next step, the thermodynamic equation approach which is constrained by soil pCO$_2$ due to biological activity should be coupled with a degassing model without increasing significantly computational time for calculations. In the future, detailed models should be created to quantify the global effect of CO_2 evasion from rivers, while considering the transitional zone from open to closed conditions in the soil-rock-system. In addition, the dilution effect due to rain events for different land cover and geomorphological setups, further mineral phases and, finally, the effect of anthropogenic activity need to be addressed. Latter processes might be relevant in order to understand to what degree human activity influences the lateral alkalinity fluxes and to quantify the response to climate processes.

3.6 Conclusion

The findings support that calcite weathering rates in the soil-rock profile are higher than the land-ocean rate via river systems. The identified climate sensitivity of carbonate weathering suggests that an increase of the mean land temperature is not necessarily causing an increase of lateral weathering fluxes. In addition, increasing temperatures have the potential to increase precipitation of carbonate minerals due to its influence on the carbonate system, as suggested, for example, by Goddéris et al. (2013).

The observed temperature dependency of alkalinity in rivers suggests that calcite dissolution increases with temperature in cold to temperate regions up to a maximum around 11°C for land surface temperature. This is in part because of an increase in soil-rock pCO$_2$. The opposite is the case for warmer regions, despite of the identified higher levels of soil-rock pCO$_2$. However, a general impact of climate change on global calcite dissolution rates is difficult to identify, due to discussed further factors, the abundance of other minerals, locations of non-open system conditions, anthropogenic influences, possible dilution due to relevant surface runoff contribution to the river water, and the CO_2 evasion from surface waters. Hence, to be able to model global carbonate rock weathering, instead of the idealized system presented here, would demand that these processes be addressed. However, for most of these processes there is still an insufficient amount of field studies available to parameterize all of these effects and to address the geochemical variety of carbonate rock systems. Therefore, modelling carbonate weathering at the global scale and estimating the impact of climate change will rely, until solved, on idealized weathering models, being either conceptual or mechanistic in high detail.

Future works should focus on understanding the global effect of instream processes in the carbon cycle and the predominance of closed to semi-closed conditions with respect to CO_2 availability for carbonate weathering. For this, more temporal river chemistry data should be collected, mainly in tropical karst regions, to decipher the main mechanism causing the decrease in alkalinity concentration observed in river data.

Chapter 4: Volcanic systems

Influence of hydrothermal fluids on dissolution of primary minerals in Aso Caldera, Japan

This chapter is being prepared for submission into an international journal as: Romero-Mujalli, G., Hartmann, J., Hosono, T., Amann, T., Louvat, P. and Böttcher, M.E., Evaluating the contribution of high temperature fluids to surface waters using Se:SO_4^{2-} molar ratios for the Aso caldera, Japan: Implications for weathering rates of volcanic areas.

4.1 Abstract

Volcanic areas, hotspots of weathering at the global scale, are ideal systems to study hydrothermal alteration and mixing processes with surface waters due to their high geothermal gradient. However, the role of hydrothermal fluids in the dissolution of primary minerals is not well understood at the catchment scale. This study aims to determine the hydrothermal contribution to the surface waters of the Aso caldera in Japan, in terms of weathering processes and related hydrochemical fluxes. Spring and river water samples were collected along the two main rivers of the caldera. Major and trace element concentrations together with stable isotopes of water (δ^2H and δ^{16}O), δ^{13}C and δ^{34}S were measured. The hot springs in this region are associated with high sulphate concentrations of magmatic origin. In contrast, in most cold springs the hydrochemistry reflects surface water-soil interactions. In particular, the cold springs have a significantly higher Se:SO_4^{2-} molar ratio than the hot springs. The lower apparent mobility of Se in the hydrothermal system is likely due to reduced conditions and adsorption into iron oxide-hydroxides. Combining Se:SO_4^{2-} and $\delta^{34}S_{sulphate}$ ratios allows to distinguish three different sources of sulphate in the Aso catchment: hydrothermal waters influenced by oxidation of sulphides, hydrothermal waters controlled by dissolution of SO_2 and sulphate from the soils. Altogether, the results show that hydrothermal waters influence the sulphur budget of the caldera outlet, accounting for 20 to 70% of the total sulphate flux. The DIC - $\delta^{13}C_{DIC}$ carbon budget also suggest that part of the rock weathering reactions were mediated by magmatic CO_2. The dissolution of magmatic CO_2 and the oxidation of sulphur of magmatic origin altogether contribute significantly to the total observed weathering fluxes, and have to be subtracted to accurately determine the atmospheric mediated weathering rates.

4.2 Introduction

Volcanic areas are the focus of weathering studies at the global scale because of their high river chemical fluxes and nutrient release rate (Goll et al., 2014; Hartmann et al., 2014b; Schopka and Derry, 2012; Gaillardet et al., 2011; Hartmann and Moosdorf, 2011; Dessert et al., 2003; Gaillardet et al., 1999; Louvat and Allègre, 1998; Louvat and Allègre, 1997). While silicate rock weathering consumes atmospheric CO_2, other sources of acids as weathering agents exist (Rive et al., 2013; Gaillardet et al., 2011; Dessert et al., 2009; Chiodini et al., 2000). In volcanic contexts, hydrothermal systems have highly diverse chemical compositions and are influenced by admixing fluids of magmatic origin to infiltrated meteoric waters. In particular, the contribution of magmatic gases, e.g. SO_2, CO_2 and halogens, enhances water-rock interactions. These processes increase the dissolved loads of the rivers draining the volcanic areas and their signature can be misinterpreted with low-temperature weathering reactions, making its impact on global weathering fluxes challenging to quantify. The magmatic gases that are “lost” to the hydrothermal systems should, however, be accounted for in the volatile element budget of volcanoes emissions.

It is however possible to distinguish the high versus low temperature weathering fluxes based on the river and spring concentrations in major and trace elements (Dessert et al., 2009; Louvat et al., 2008; Rad et al., 2006; Louvat and Allègre, 1998; Louvat and Allègre, 1997), or to quantify the magmatic contribution of SO_4^{2-} and Cl^- to riverine chemical fluxes (Gaillardet et al., 2011; Rad et al., 2006). Stable isotope geochemistry also allows to disentangle mixing processes and sources in the natural waters, with emphasis on stable isotopes of carbon and contribution of magmatic CO_2 into waters (Rive et al., 2013; Rad et al., 2011; Chiodini et al., 2000). Additionally, stable isotopes of sulphur can provide valuable information on redox processes and the different S sources in the studied water body (Afsin et al., 2014; Hosono et al., 2014; Tostevin et al., 2014; Smith et al., 2010; Calmels et al., 2007; Böttcher et al., 1998; Rye et al., 1981; Yamamoto, 1976).

Hydrothermal systems, besides their importance in formation of ore deposits and their influence on river chemical fluxes, are potential sites for abiotic synthesis of organic molecules that are believe to be related to the origin of life (Barge et al., 2017; Stüeken et al., 2013; Martin et al., 2008; Martin and Russell, 2006; Holm and Andersson, 2005). Here, selenium (Se) represents an important component as essential micronutrient and its chemical species resemble those of sulphur (Fernández-Martínez and Charlet, 2009; Cooke and Bruland, 1987; Shamberger, 1981). Therefore, a relatively constant Se:S molar ratio might be expected in natural systems. However, slightly different geochemical behaviours between both elements can be detected due to adsorption processes, redox reactions, anthropogenic input and type of hydrothermalism (Fellowes et al., 2013; Layton-Matthews et al., 2013; Shamberger, 1981; Yamamoto, 1976; Suzuoki, 1964). Se concentration in fumarolic waters and hydrothermal sulphide deposits is directly proportional to the temperature of the system and depends on the physicochemical characteristics of the system, such as pH, redox-state, pressure and volume (Queffurus and Barnes, 2015; Layton-Matthews et al., 2013; Shamberger, 1981; Yamamoto, 1976; Suzuoki, 1964).

As sulphur, Se can be emitted by volcanic plumes as volatiles or colloids. The Se:S molar ratio in volcanic gases are similar to those measured in rainwater because of the relatively short residence time in the atmosphere (Wen and Carignan, 2007; Greenland and Aruscavage, 1986; Kotra et al., 1983). Therefore, Se concentration in volcanic soils tends to decrease with distance to the volcanic crater (Floor et al., 2011). Se:S molar ratios are relatively high in soil pore-water due to Se adsorption onto iron and aluminium oxide-hydroxides and organic matter, to atmospheric deposition and dissolution of sulphur minerals containing Se (Floor et al., 2011; Fernández-Martínez and Charlet, 2009; Nakamaru et al., 2005). Under reducing conditions, Se and S tend to precipitate as sulphide minerals or as elemental Se or S. Moreover, SeO_3^{2-} oxidation to SeO_4^{2-} is kinetically slower than the equivalent oxidation of sulphur species. Therefore, both SeO_3^{2-} and SeO_4^{2-} can be found in soils even if SeO_4^{2-} is the thermodynamically stable species (Fernández-Martínez and Charlet, 2009; Séby et al., 2001).

These similar but slightly different geochemical behaviours for Se and S allow to classify different natural systems from their Se to S concentration ratios (Se:S). In this work we test the potential of Se:SO_4^{2-} molar ratio together with sulphur and oxygen stable isotopes of sulphate ($\delta^{34}S_{sulphate}$ and $\delta^{18}O_{sulphate}$), O and H stable isotopes of water, and $\delta^{13}C$ of dissolved inorganic carbon (DIC) in natural waters to distinguish hot and cold springs and to quantify the impact of hydrothermal processes on the weathering rates from the Aso caldera (Fig. 4.1), one of the most active volcanoes in Japan.

4.3. Site description

Aso volcano, located in Kyushu Island (Fig. 4.1), is one of the major active volcanoes in Japan and one of the largest caldera volcanoes in the world. The present-time caldera topography, 18km E-W by 25km N-S in diameter, was formed ca. 90ka ago due to eruptions of basaltic to rhyolite magmas (Nakada et al., 2003; Watanabe, 1978). The basement rocks are composed mainly of Paleozoic to Mesozoic metamorphic rocks, cretaceous granitic intrusions and small Miocene volcanic and plutonic complexes (Ono et al., 1981). The compositions of the eruptive magmas have changed over time: felsic magma activities dominated in the initial stage of the caldera formation, while mafic magmas were predominant in the late stage (Nakada et al., 2003; Ono et al., 1981). Naka-dake, the only active central cone in the Aso Caldera, is a stratovolcano of basaltic andesite to basalt. Its dominant eruption product is characterized by an olivine-augite basaltic andesite ash and scoria with a relatively constant mineralogical and chemical composition (Ono et al., 1995). Moreover, volcanic emissions of Japan have the characteristic of having a relatively low CO_2:SO_2 molar ratio, about 1.8 in the Aso Caldera (Aiuppa et al., 2017).

The Futagawa-Hinagu fault system is one of the major active fault systems on Kyushu Island. The fault mechanism is a combination of normal and strike-slip with right lateral movement (Nakada et al., 2003). Northern of the Aso caldera is located at the eastern extension of the Futagawa fault systems, which influence surface geological structures in the Aso caldera. The surface deformations occurred during the 2016 Kumamoto earthquake are in association with this fault system (Tsuji et al., 2017). Most of the geological structures (faults and fractures) follow the same direction of the Futagawa fault (Fig. 4.1), and it might influence migration of hydrothermal fluids to the surface.

The Naka-dake has a crater lake that is influenced by the hydrothermal activity beneath the volcano, where infiltrated waters are heated and mixed with magmatic fluids, and transported to the surface due to convective heat transfer (Terada et al., 2012; Terada and Sudo, 2012). The mixing process results in a water with a pH of about 0.5 and with high concentration of sulphur and chlorine. Precipitations of elemental sulphur, gypsum and anhydrite are major compositions of the lake sediments (Miyabuchi and Terada, 2009). Besides the crater lake and its leakage streams, several natural hot springs can be found inside the Aso caldera, where mixing with magmatic fluids have been reported (Yamada et al., 2011; Hase et al., 2005).

The Aso caldera is drained by Kurokawa and Shirakawa rivers (Fig. 4.1), dividing the caldera in northern and southern catchments, respectively. The two rivers join just before the caldera outlet and flow downstream as Shirakawa main river. The caldera drainage area is 386km^2. The region is characterized by a temperate humid climate affected by monsoon circulation, it presents a mean air temperature of about 10°C and average precipitation of 3200mm a^{-1} (Japan Meteorological Agency in: http://www.data.jma.go.jp/obd/stats/data/en/smp/index.html). The average water discharge in 2015 was 26m^3 s^{-1} (from Water Information System of the Ministry of Land, Infrastructure, Transport and Tourism).

4.4 Methods

4.4.1 Sampling and chemical analysis.

Water samples from 29 springs and 34 rivers and streams (in both Kurokawa and Shirakawa catchments) were collected during seven different field campaigns: (1) March-April 2014, (2) September-October 2014, (3) May 2015, (4) June-July 2015, (5) September 2015, (6) July 2016 and (7) October 2016 (Fig. 4.1). In addition, rainwater was sampled in the caldera in July and October 2016. The pH, dissolved oxygen, temperature and electrical conductivity of each sample were determined in situ using a digital pocket meter from WTW (Multi-parameter portable meter MultiLine® 3630 IDS). Samples were filtered through 0.2 and 0.45µm with cellulose acetate filters and stored in polypropylene bottles. Alkalinity was measured by titration method. Concentrations of major ions (i.e. Na^+, K^+, Ca^{2+}, Mg^{2+}, Cl^-, SO_4^{2-}, NO_3^-, F^- and PO_4^{3-}) were determined by ion chromatography (IC, Metrohm 881 Compact IC Pro system) at the University of Hamburg. Stables isotope ratios of water (δ^2H_{water} and $\delta^{18}O_{water}$) were determined by cavity ring-down laser spectroscopy (CRDS) using Picarro L2140-i (with analytical precision of ± 0.05‰ and ± 0.5‰, respectively) at the Leibniz Institute for Baltic Sea Research Warnemünde (Leibniz IOW), and reported values are relative to Vienna Standard Mean Ocean Water (VSMOW). Stable carbon isotope ratios ($\delta^{13}C_{DIC}$) were determined using a GasBench interfaced with an isotope ratio mass spectrometer (irMS-GB) with analytical precision of ± 0.1‰, at Leibniz IOW, and related to Vienna Peedee Belemnite standard (VPDB). The stable sulphur isotope ratios of sulphate ($\delta^{34}S_{sulphate}$) were analysed by continuous flow gas isotope ratio mass spectrometry coupled with an elemental analyser (CF-IRMS-EA), and delta values are expressed relative to the standard VCDT (Vienna Canyon Diablo Troilite). The oxygen stable isotope ratios of sulphate ($\delta^{18}O_{sulphate}$), relative to VSMOW standard, was determined by continuous flow isotope ratio mass spectrometry coupled with a high temperature conversion elemental analyser (CF-IRMS-TC/EA) at Kumamoto University (Hosono et al., 2015; Hosono et al., 2014). The analytical precision of stable isotope ratios of sulphur and oxygen in sulphate was ± 0.2‰ and ± 0.3‰, respectively. Samples for trace element analysis were acidified with nitric acid (ultrapure grade). The concentrations of trace elements were analysed by inductively coupled plasma mass spectrometry (ICP-MS) at the Kumamoto University and at the Institut de Physique du Globe de Paris.

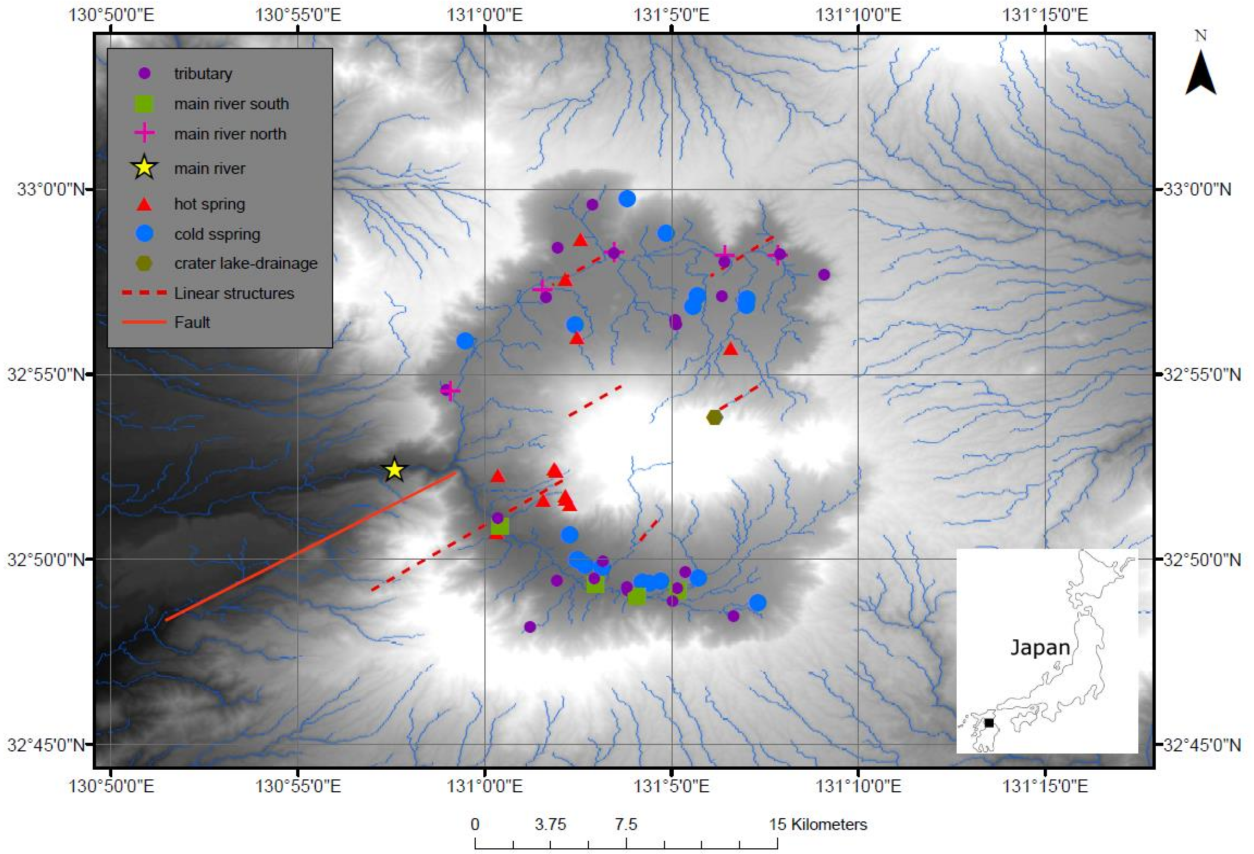

Figure 4.1. Sample locations for different water sample types. Samples were taken during 7 different campaigns: 2014 (spring/fall), 2015 (spring/summer/fall) and 2016 (summer/fall). The red line represents Futagawa fault.

4.4.2 Mixing model.

It is possible to calculate the fraction (f_j) of the chemical species in a system from three different sources (*a* soil, *b* magmatic SO_2 and *c* oxidation of S(-II)) using the following equations:

$$P_m^1 = f_a P_a^1 + f_b P_b^1 + f_c P_c^1 \tag{4.1}$$

$$P_m^2 = f_a P_a^2 + f_b P_b^2 + f_c P_c^2 \tag{4.2}$$

$$1 = f_a + f_b + f_c \tag{4.3}$$

where, P_i represents the parameter *i*, stable isotopic composition or ratio of chemical species (in this study Se:SO_4^{2-} molar ratios and $\delta^{34}S_{sulphate}$ are used), for each source endmember *a*, *b* and *c*.

This equation is solved by linear system of equations of the type:

$$Ax = y \tag{4.4}$$

where, *A* is the matrix of size 3x3 with the coefficients of each f_j (the P_a^i, P_b^i and P_c^i), *x* is the vector with the unknowns f_j and *y* the vector with P_m^1, P_m^2 and 1. The error of the numerical solution (Eq.

4.4) is in the order of the machine precision (10^{-16}), thus, the uncertainty of the mixing model is the result of the propagated analytical uncertainties.

The mixing model implemented to calculate the contribution of magmatic CO_2 into the spring water considers two different sources (magmatic CO_2 and soil CO_2). The equation is in accordance to previous published mixing models in spring waters (Yamada et al., 2011; Chiodini et al., 2000). Here, the fraction of magmatic CO_2 (f_{magma}) contributing to the dissolved inorganic carbon (DIC) of spring waters is calculated by the following equation:

$$f_{magma} = 1 - \frac{\delta^{13}C_{DIC_f} - \alpha - \delta^{13}C_{DIC_{magma}}}{\delta^{13}C_{DIC_{soil}} - \delta^{13}C_{DIC_{magma}}} \tag{4.5}$$

where, $\delta^{13}C_{DIC_{magma}}$ is the isotopic ratio of magmatic CO_2, a value of -5‰ was used in this study (Mason et al., 2017); $\delta^{13}C_{DIC_{soil}}$ is the isotopic ratio of soil pore-water, a range between -30 to −20‰ was used (Rive et al., 2013; Cerling et al., 1991); and, $\delta^{13}C_{DIC_f}$ is the isotopic ratio of DIC in the spring or river sample. When evasion is applicable, a fractionation factor, α, is included with a value between 3 and 5‰ after Doctor et al. (2008).

4.5 Results and Discussion

4.5.1 Chemistry of natural waters in the Aso caldera.

The results of the chemical analysis of natural waters in the Aso caldera are shown in Tables D.1-4 in the Appendix. In general, the hot springs presents a higher conductivity, lower pH and dissolved oxygen than cold springs or other surface waters. Dissolved oxygen in hot springs ranged from 28 to 165µM, whereas conductivity ranged from 200 to 3800µS cm^{-1}. Cold springs displays a lower conductivity (between 66µS cm^{-1} and 454µS cm^{-1}) and higher dissolved oxygen (between 220 and 420µM) than hot springs. Streams and rivers, however, exhibit a conductivity and dissolved oxygen between hot and cold springs ranges, from 44 to 910µS cm^{-1} and 190 to 386µM, respectively.

The hot spots of high dissolved solid concentrations in the Aso caldera correspond to hydrothermal waters that are dominated by SO_4^{2-}, alkalinity and Ca^{2+} or Na^+ + K^+, indicating a strong influence of magmatic CO_2, SO_2 or H_2S (Fig. 4.2). Except for the crater lake, the relatively low Cl^- concentrations indicate hot springs might not be strongly influenced by magmatic HCl, as reflected by their pH: hot springs dominated by Ca^{2+}, SO_4^{2-} and alkalinity have on average a pH ≈ 5.6 (type I), while a pH of about 7.2 is observed in waters of the type Na^+ + K^+ HCO_3^- or SO_4^{2-} (type II). The chemical composition of hydrothermal springs generally results from their subsurface pathways with percolation of ascending magmatic gases, the dissolution of rock and magma-derived minerals (e.g. sulphides), re-equilibration between water and secondary minerals, and from admixture of drainage waters. Type I waters might be associated to the dissolution of magmatic gases, CO_2 and SO_2, into groundwater and rapid reactions with host rocks, without achieving equilibrium (Delmelle et al., 2000). Type II hydrothermal waters may express a more advanced equilibrium between hydrothermal fluids and rocks, where further dissolution of minerals has neutralized the acidity of the waters (Smith et al., 2010). Moreover, SO_4^{2-} rich waters generally result from high temperature magmatic fluids transported by deep groundwaters (Giggenbach and Soto, 1992). Hydrothermal waters, or hot springs, have δ^2H_{water} and $\delta^{18}O_{water}$

signatures of meteoric origin (Fig. 4.3), indicating that the Aso hydrothermal system recharges from percolating meteoric water heated at depth, as suggested by Hase et al. (2005). In general, chloride (Cl^-) represents less than 25% of total anions equivalent concentrations of natural waters in the Aso caldera, including hot springs (Fig. 4.2a, 4.2c). Therefore, the hydrothermal contribution of magmatic chlorine in surface waters can be less significant compared to SO_2 or CO_2. The chemical composition of the natural waters in the Aso caldera is variable and results from different sources and physicochemical processes. Its spatial variations seem to follow heat fluxes distribution within the caldera, reflecting the influence of a magmatic chamber beneath the central active volcanic part of the Aso caldera, but also of a secondary heat and fluid source below the Futagawa active fault system in the northern catchment (Kurokawa river, Hosono et al., 2018).

The variability of chemical composition observed for the springs (cold and hot, Fig. 4.2a, 4.2b) is as important for the streams (Fig. 4.2c, 4.2d). Cold springs and stream waters are generally dominated by Ca^{2+} and alkalinity or SO_4^{2-} (Fig. 4.2), similar to several hot springs. The drainage water coming from the crater lake is the most acid stream water ($pH < 5$) and is particularly enriched in sulphate, due to the dissolution of magmatic SO_2 and H_2S coupled to a strong evaporation (Terada et al., 2012; Miyabuchi and Terada, 2009). The crater lake drainage water has variable δ^2H_{water} and $\delta^{18}O_{water}$, depending on seasonality, where highest values were documented for the sample on March 2017. This strong enrichment on heavier water isotopes might be due to the constant evaporation and possible isotopic exchange during SO_2 disproportionation, with the subsequent precipitation of sulphate minerals in lake sediment, or with volcanic CO_2 (Karolytė et al., 2017).

If only the major ion concentrations are considered, the sources of solutes to the Aso's natural waters are difficult to decipher, but trace elements and C and S isotopes can be helpful.

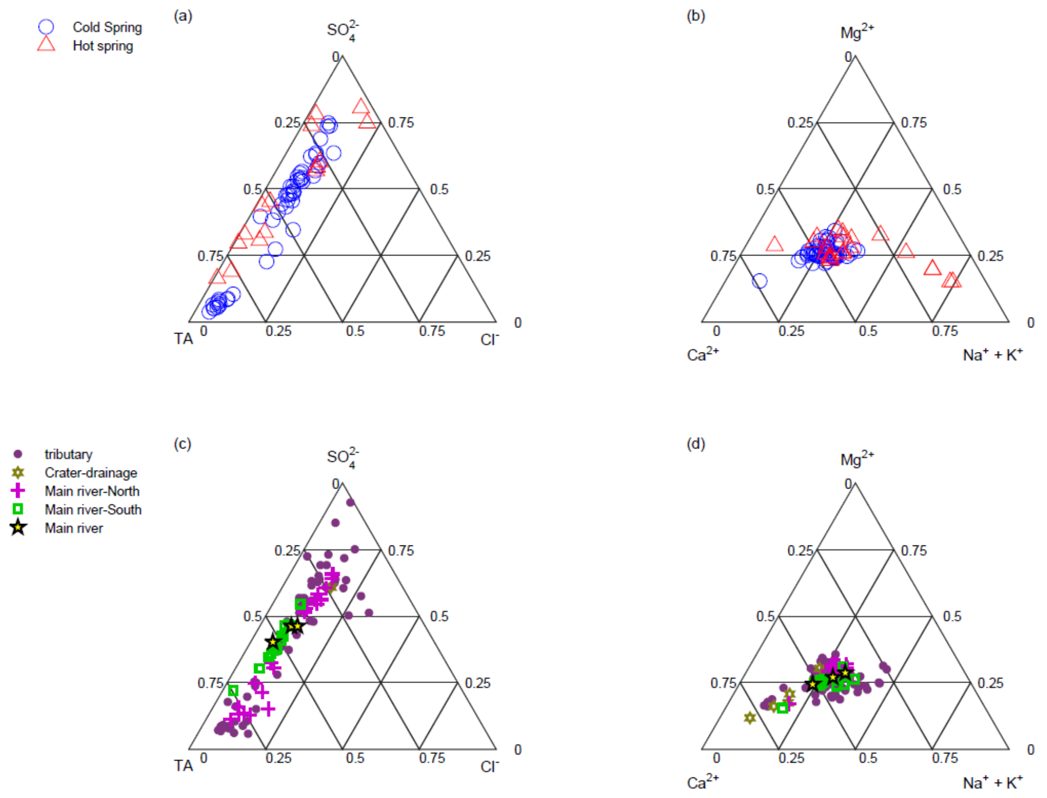

Figure 4.2. Ternary diagrams of major ions in water samples. (a) Anions and (b) cations in cold and hot springs. (c) Anions and (d) cations in stream water samples.

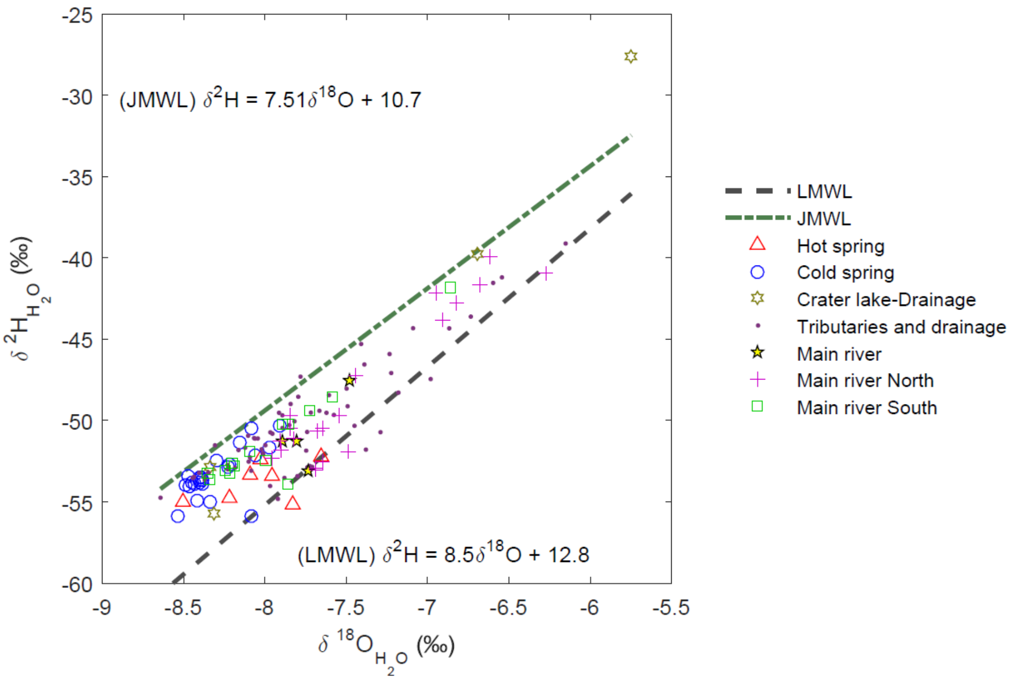

Figure 4.3. Relationship between δ^2H_{water} and $\delta^{18}O_{water}$ in water samples from Aso caldera. Japanese meteoric water line (JMWL) was taken from Ichiyanagi et al. (2016) (average line for Japanese rainwaters) and local meteoric water line (LMWL) from Okumura et al. (2018) (Precipitation from April to September).

4.5.2 Selenium to sulphate molar ratio

Selenium concentrations in the Aso's waters range from 0.1 to 30nM for streams, 0.1 to 37nM for cold springs and 0.2 to 17nM for hot springs (Table C.4). While other trace elements such as Fe, Al and Mn have distinctively high concentrations in hydrothermal waters compared to streams, there is no noticeable enrichment for Se. However, spring waters in Aso are clearly classified by their Se:SO_4^{2-} molar ratio, with high Se:SO_4^{2-} for cold springs and low Se:SO_4^{2-} for hot springs (Fig. 4.4a). The reason for low Se:SO_4^{2-} and low Se concentration in hot springs is not well understood. Selenium could escape from the hydrothermal system during partition between steam and water, and is generally less abundant in reduced waters, being more stable as oxidized Se(IV) under the form of oxyanions (Floor and Román-Ross, 2012; Conde and Sanz Alaejos, 1997). In the hydrothermal waters of Volcano island, Italy, Se was enriched in hot oxidized Cl-rich waters and depleted in Fe-S-rich waters (Aiuppa et al., 2000). Furthermore, Se can form organic volatiles (e.g. Dimethyl selenium) in hydrothermal conditions similar as S (Hirner et al., 1998). These compounds are assumed to be produced by abiotic processes. Nevertheless, in some experiments, at low temperature and pressure conditions, the dimethylation of Se is only possible through biotic organic molecules (Amouroux et al., 2000). It is still not well established whether the loss of Se by volatilization of organic or inorganic chemical species is significant enough to explain the low concentration of some hot springs, as in the Aso caldera.

Se concentrations in hot springs show a good correlation with Fe and Cu concentrations (Fig. 4.4b and 4.4d, respectively), suggesting that Se is associated to oxide-hydroxides or sulphides minerals. Furthermore, although studies confirm that Se concentration decreases in acid solutions, at low temperature and pressure, due to adsorption (Basu et al., 2007; McNeal and Balistrieri, 1989), in hot springs an increase at low pH is observed (Fig. 4.4c), similar trend for Fe (Fig. 4.4e).

We propose that Se in the Aso hydrothermal system is preferentially under the forms Se(-II), Se(0) and Se(IV), which are, with exception of Se(-II), relatively more immobile than its equivalent S species. Se(IV) is preferentially adsorbed into Fe and Al oxide-hydroxides, where it can be immobile if crystalline minerals are formed from the amorphous oxides (Börsig et al., 2017). Furthermore, there is clear evidence that the temperature of the hydrothermal system controls the Se:S molar ratio of hydrothermal fluids (Layton-Matthews et al., 2013; Yamamoto, 1976; Suzuoki, 1964). Therefore, it is likely that a combination of different processes controls the Se:SO_4^{2-} molar ratio in the Aso caldera, and leads to a decrease of Se concentrations in the shallow hydrothermal system, especially where oxide-hydroxides are formed.

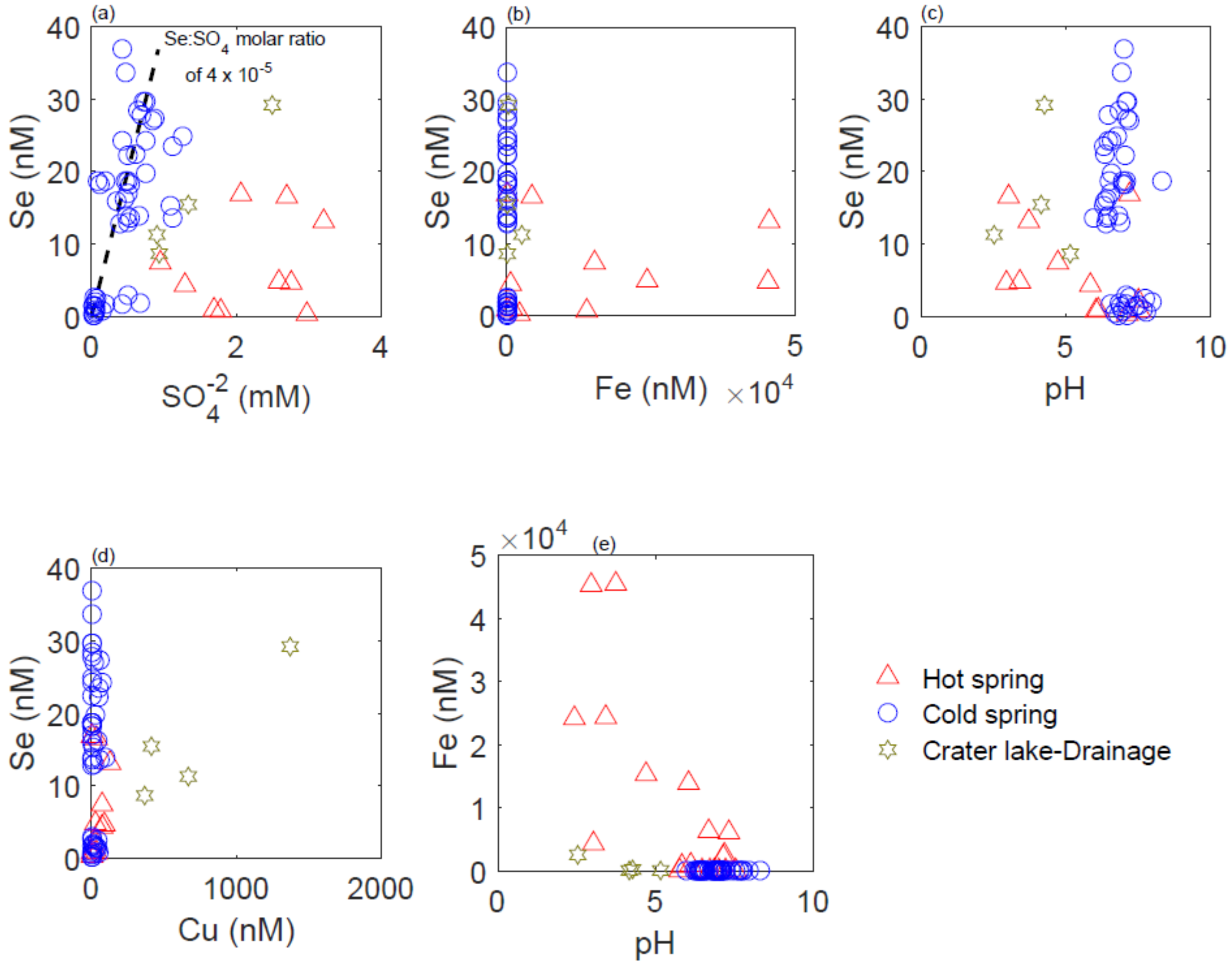

Figure 4.4. (a) Se vs SO_4^{2-}, showing the different behaviour between hot and cold springs, regression line has a r^2 of 0.4; (b) Se against Fe; (c) Se vs pH; (d) Se vs Cu; and (e) Fe vs pH. The Se:SO_4^{2-} molar ratio of 4 x 10^{-5} ± 2 x 10^{-5} is the results of the correlation in cold spring samples.

In this work, the lower limit of Se:SO_4^{2-} molar ratio for soil-related samples is 4 x 10^{-5} ± 2 x 10^{-5}, obtained from the correlation using cold springs (Fig. 4.4a, r^2 of 0.4), is in agreement with Se:SO_4^{2-} of spring water and rainwater (Fig. 4.5). Se:SO_4^{2-} molar ratio of different samples in volcanic systems (Fig. 4.5) shows a clear difference between the hydrothermal fluids (hot springs and fumarolic fluids) and the surficial fluids (rainwater and cold springs). However, it is important to highlight that within the sulphur-rich hydrothermal system two main zones are defined according to the temperature, high and low temperature hydrothermal systems. High temperature hydrothermal fluids (> 200°C) can produce sulphide deposits with Se:S molar ratios up to 10^{-1}, whereas low temperature hydrothermal sulphide deposits (< 200°C) have Se:S molar ratios lower than $10^{-4.5}$, as are observed in this work for hot springs. However, the Se:S of the sulphur deposits is usually higher than the fluids at a given temperature (Layton-Matthews et al., 2013; Suzuoki, 1964).

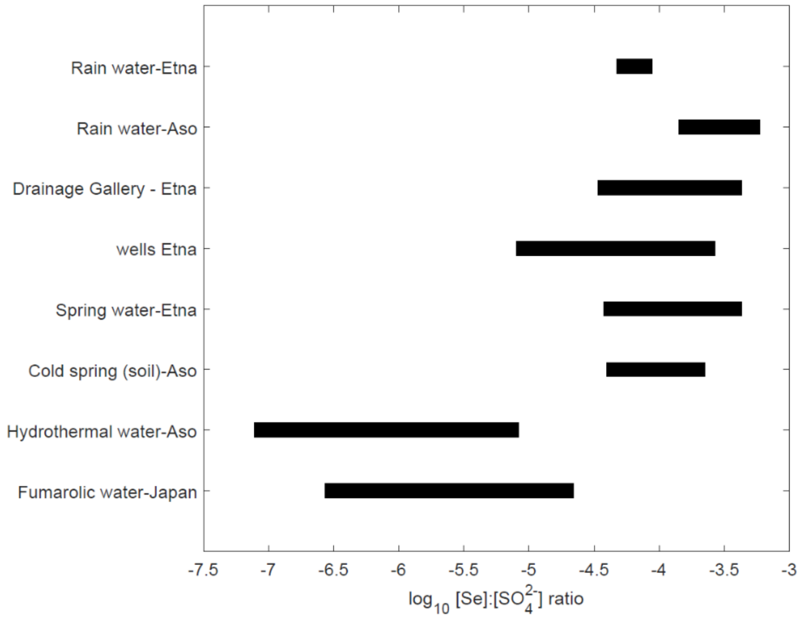

Figure 4.5. Logarithm scale of Se:SO_4^{2-} molar ratio for some water samples in Aso and Etna. Data rainwater Etna comes from Calabrese (2009) and Etna's spring, drainage gallery and well samples from Aiuppa et al. (2000). Japanese fumarolic water from Suzuoki (1964).

4.5.3 Influence of magmatic gases SO_2, H_2S and CO_2

Waters draining the Aso caldera are influenced by deep hydrothermal fluids that have been circulating in the neighbourhood of magma chambers, either under the central cone or beneath the north-western Futagawa fault system (Hosono et al., 2018). The dissolution of magmatic CO_2 and SO_2 in water produce protons according to the following reactions:

$$CO_{2(g)} + H_2O_{(l)} \leftrightarrow\ HCO^-_{3(aq)} + H^+_{(aq)} \tag{4.6}$$

$$SO_{2(g)} + H_2O_{(l)} + {}^1/_2\, O_{2(g)} \leftrightarrow\ SO^{2-}_{4(aq)} + 2H^+_{(aq)} \tag{4.7}$$

These reactions thus produce carbonic and sulphuric acids that promote the dissolution of rocks (Berner et al., 1983). The oxidation of volcanic or hydrothermal sulphur minerals produces additional sulphuric acid. In the following, we attempt to budge the sulphur and carbon content of the Aso's springs and streams in order to quantify the influence of the hydrothermal system on the weathering rates.

4.5.3.1 Sulphur budget

Aso hot springs can be classified in at least two groups according to their O and S isotopic ratios of the sulphates: hydrothermal waters with high $\delta^{34}S_{sulphate}$ and $\delta^{18}O_{sulphate}$ and acid hydrothermal waters with low $\delta^{34}S_{sulphate}$ and $\delta^{18}O_{sulphate}$ (Fig. 4.6a). Isotopically heavier hydrothermal waters occur mostly in the north-western section of the catchment, where deep over-pressured hydrothermal fluids migrate to the surface through newly open pathways associated to the seismic deformation of the Futagawa fault system (Hosono et al., 2018). The high sulphate concentration might result either from the disproportionation of magmatic SO_2 in the groundwater or from sulphate reduction/disproportionation in a deep aquifer with reducing environment (Hosono et al., 2018). In contrast, the acid hot springs with low $\delta^{34}S_{sulphate}$ possibly result from the oxidation of magmatic S(-II) (Afsin et al., 2014; Rye, 2005) and are generally located close to the Aso central volcanic cone. In the stream and cold spring samples, sulphate may also come from the surface drainage system, with mixed atmospheric, anthropogenic and mineral sources, with intermediate $\delta^{34}S_{sulphate}$ (Fig. 4.6b).

Because the redox conditions within the streams are not changing significantly during their course, we hypothesize that only admixing of different water masses can change the Se:SO_4^{2-} molar ratio of the streams. Therefore, a three component mixing model (Eq. 4.1-4.4 in section 4.4.2) is applied to determine the contribution of type-I (Se:SO_4^{2-} of $1.7 \times 10^{-6} \pm 1 \times 10^{-7}$ and $\delta^{34}S_{sulphate}$ of 2.5 ± 0.1‰) and type-II hydrothermal waters (Se:SO_4^{2-} of $1.7 \times 10^{-6} \pm 1 \times 10^{-7}$ and $\delta^{34}S_{sulphate}$ of 17.5 ± 0.1‰) and of waters percolating soils (Se:SO_4^{2-} of $4 \times 10^{-5} \pm 2 \times 10^{-5}$ and $\delta^{34}S_{sulphate}$ of 6 ± 1‰) to the sulphate budget of the water samples. The Se:SO_4^{2-} and $\delta^{34}S_{sulphate}$ of each endmember were taken based on Fig. 4.5 and stable isotopic composition of spring waters, respectively.

The results (table 4.1) showed that sulphate can be in some cold springs strongly sourced from hydrothermal waters (90 ± 10%). The drainage sample downstream the crater lake presents, on March 27th of 2014, approximate 70 ± 10% hydrothermal SO_4^{2-}, mainly from acid hydrothermal origin (oxidation of sulphide).

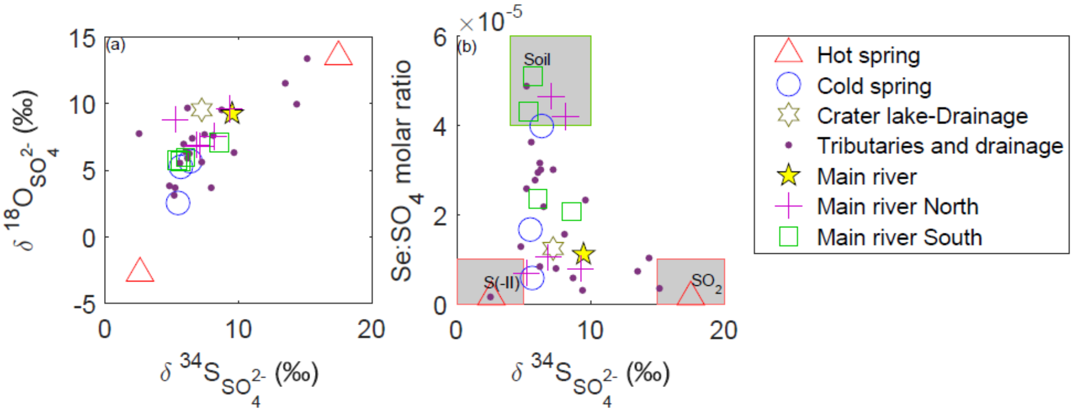

Figure 4.6. (a) Relationship between $\delta^{18}O$ and $\delta^{34}S$ stable isotopes of sulphate in water samples from the Aso caldera. The (b) Se:SO_4^{2-} molar ratio vs $\delta^{34}S_{sulphate}$ shows three different sources: (1) sulphate from soil pore water, which represents the mixture between atmospheric origin, anthropogenic Se, and sulphate minerals dissolution in soils; (2) Hot springs with a clear low $\delta^{34}S_{sulphate}$ signature, possibly originated from oxidation of magmatic S(-II) ($\delta^{34}S_{sulphate}$ < 0‰ (Delmelle et al., 2000)); and, (3) hot springs with high $\delta^{34}S_{sulphate}$ signature (> 15‰), which might be the result of dissolution of magmatic SO_2 into water and occurrence of subsequent sulphate reduction.

Table 4.1. Summarized calculations for mixing of SO_4^{2-} in natural waters using Se:SO_4^{2-} molar ratio and $\delta^{34}S$ of sulphate. Values inside the brackets represent the range of data and the value outside the brackets is the mean for different dates.

Sample	Type*	$\delta^{18}O_{SO4}$ (‰)	$\delta^{34}S_{SO4}$ (‰)	$\log_{10}$Se:SO_4^{2-}	f_{soil}^1	f_{H-I}^2	f_{H-II}^3
S01	mrn	8.8	5.2	-5.22 [-5.66,-5.05]	0.1	0.7	0.2
S02	t,d	13.4	15.1	-5.46 [-5.47,-5.44]	0.1	0.1	0.8
S03	cc	9.5	7.2	-4.95 [-5.04,-4.9]	0.3	0.5	0.2
S04	t,d	6.2	6.3	-4.29 [-4.52,-3.85]	0.7	0.2	0.1

S05	t,d	7.6	8.1	-4.87 [-4.98,-4.8]	0.4	0.3	0.3
S06	mrs	5.9	6	-4.8 [-4.97,-4.63]	0.6	0.3	0.1
S07	cs	5.2	5.7	-4.32 [-5.23,-3.66]	0.1	0.7	0.2
S08	t,d	9.2	9.4	-5.35 [-5.51,-5.24]	0	0.5	0.5
S09	t,d	5.9	6.2	-4.51 [-4.53,-4.5]	0.8	0.1	0.1
S10	mrs	5.7	5.7	-4.37 [-4.47,-4.29]	1	0	0
S11	t,d	3.7	5.2	-4.68 [-4.75,-4.59]	0.6	0.3	0.1
S12	t,d	7.6	7.4	-4.87 [-5.1,-4.64]	0.2	0.5	0.3
S13	t,d	7.4	6.5	-4.54 [-4.66,-4.39]	0.5	0.3	0.2
S14	mrs	5.8	5.4	-4.73 [-5.36,-4.37]	1	0	0
S15	t,d	5.6	5.6	-4.66 [-5.02,-4.44]	0.9	0.1	0
S16	cs	2.6	5.5	-4.64 [-4.88,-4.43]	0.4	0.5	0.1
S17	t,d	3.1	5.2	-4.39 [-4.5,-4.31]	1	0	0
S19	cs	5.6	6.3	-4.62 [-5.39,-4.25]	1	0	0
S20	t,d	6.4	6	-4.5 [-4.53,-4.47]	0.7	0.2	0.1
S21	hs	-2.8	2.6	-5.49 [-5.77,-5.21]	0	1	0
S22	t,d	3.8	4.8	-4.84 [-4.89,-4.76]	0.3	0.6	0.1
S23	mrs	7.1	8.5	-4.66 [-5.06,-4.13]	0.5	0.2	0.3
S24	t,d	5.6	7.2	-4.61 [-4.68,-4.52]	0.7	0.1	0.2
S25	mrn	7.6	8.1	-4.62 [-5.04,-4.38]	1	0	0
S26	t,d	6.3	9.6	-5.16 [-5.69,-4.63]	0.6	0.1	0.3
S27	t,d	6.9	5.9	-4.55 [-4.56,-4.54]	0.7	0.3	0
S28	t,d	7.8	2.5	-5.42 [-6.02,-4.93]	0	1	0
S29	t,d	9.5	8.7	-5.44 [-6.2,-5.01]	0.1	0.5	0.4
S30	mrn	6.9	6.8	-4.7 [-4.97,-4.5]	0.2	0.6	0.2
S31	t,d	9.7	6.2	-4.72 [-5.07,-4.42]	0.2	0.6	0.2
S32	t,d	10	14.3	-4.87 [-4.99,-4.78]	0.3	0	0.7
S33	mr	9.3	9.5	-4.75 [-4.95,-4.47]	0.5 [0.2,0.8]	0.3 [0.1,0.5]	0.2 [0,0.4]
S34	t,d	11.5	13.5	-5.39 [-5.87,-5.08]	0.15	0.15	0.7
S35	mrn	9.6	9.3	-5.29 [-5.73,-5.1]	0.2	0.4	0.4
S36	mrn	6.8	7.1	-4.45 [-4.54,-4.33]	1	0	0

* Cold springs (cs), hot springs (hs), crater lake drainage (cc), tributary or drainage (t,d), main river south (mrs), main river north (mrn) and catchment outlet (mr).

1 Fraction of sulphate that comes from the soil pore water (f_{soil})

2 Fraction of sulphate that comes from the type I hydrothermal waters (f_{H-I}), influenced by possible oxidation of S(-II).

3 Fraction of sulphate that comes from the type II hydrothermal waters (f_{H-II}), influenced by magmatic SO_2.

4.5.3.2 Carbon budget

Stable carbon isotope ratios ($\delta^{13}C$) of DIC in spring waters (Fig. 4.7) range from -18 to -4‰, when DIC concentrations are between 1 and 10mM. There is a marked difference between cold and hot springs: low DIC (< 2mM) and low but variable $\delta^{13}C$ values (-18 to -10‰) for cold springs and high DIC (> 2mM) for hot springs with high $\delta^{13}C$ (-8 to -4‰), increasing with DIC (Fig. 4.7a). Three main C sources can be considered here: atmospheric CO_2 ($\delta^{13}C \approx -8$‰), magmatic CO_2 with $\delta^{13}C \approx -5$‰ (Mason et al., 2017), and soil CO_2 with $\delta^{13}C$ -25 ±5‰ (Rive et al., 2013; Cerling et al., 1991). In cold springs, the carbon $\delta^{13}C$ could represent a mixing between the atmospheric CO_2 and the biogenic CO_2 from soil respiration or microbial activity. The hot spring trend would then be a mixing between the atmospheric and the magmatic CO_2. The mixing calculation (Eq. 4.5) was conducted using two endmembers: soil and magmatic CO_2, with values of -5‰ and -25 ±5‰, respectively.

The influence of magmatic CO_2 in stream waters is challenging to estimate because other processes occurring in rivers - namely CO_2 evasion, respiration and oxidation of organic matter – change the DIC concentration and its carbon isotopic ratio (Deines et al., 1974). In spring waters, however, degassing of CO_2 is not relevant because it starts taking place during the first meters after the emerging from the spring (Doctor et al., 2008). If water velocity of the streams is high enough and no algae and biofilms are observed, photosynthesis and respiration are likely negligible (Rive et al., 2013).

Stream and river samples have a variable $\delta^{13}C$ values (Fig. 4.7). The sample S51, located nearby a hot springs area, has a constant influx of hot spring water and presents a relatively high $\delta^{13}C$ (-1 ± 0.1‰), which might be caused by CO_2 evasion. Assuming that the DIC in this stream sample has a magmatic origin, the fractionation due to degassing is 4 ± 0.1‰.

The range of magmatic influence in cold spring samples is from 37 ± 9% to 74 ± 5% (table D.3), whereas in hot spring samples hydrothermal influence is from 85 ± 3% to 100 ± 3%. Samples S16 and S44, although their relatively high influence of magmatic DIC, are located near the caldera rim, where the hydrothermal waters are not influenced by magmatic fluids from the volcano. Therefore, waters infiltrating the caldera rim are mixed with other deep CO_2 source.

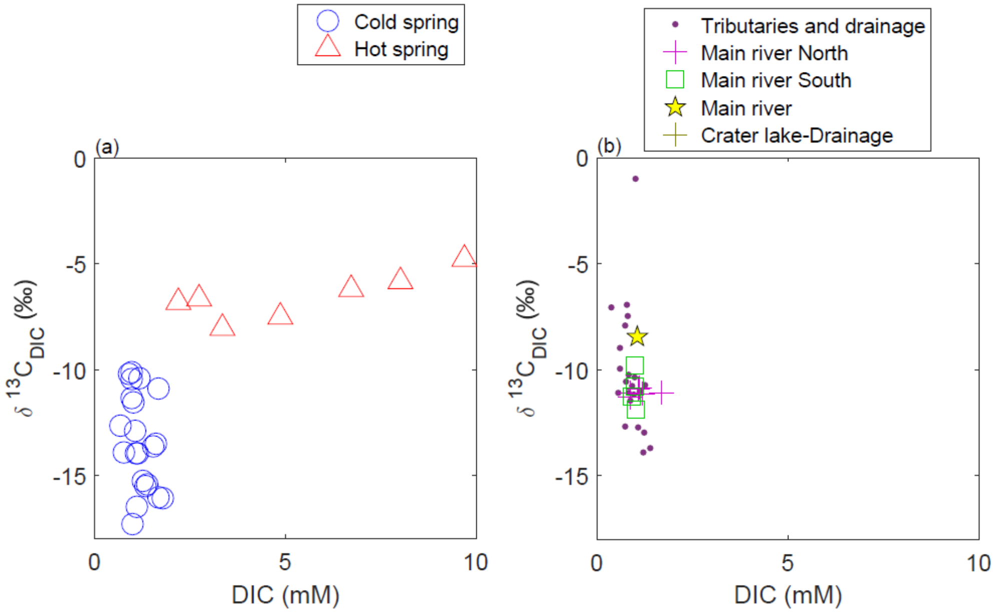

Figure 4.7. Scatterplots for $\delta^{13}C_{DIC}$ against DIC for (a) Aso hot and cold spring samples and (b) streams and rivers.

4.5.4 Hydrothermal influence on weathering rates

The northern part of the hydrological catchment (Kurokawa river) is highly influenced by hydrothermal fluids, mainly due to the deformations in the eastern extension of the Futagawa fault system, which triggers the circulation of deep fluids to the surface (Hosono et al., 2018), and to the influence of acid hydrothermal waters coming from the magma chamber. The $Se:SO_4^{2-}$ molar ratio of the rivers draining the catchment confirms this finding (Fig. 4.8). Moreover, a clear decrease in $Se:SO_4^{2-}$ molar ratio is observed in the southern part of the catchment (Shirakawa river) at about 11km distance from the outlet. Similarly, a strong increase in boron concentration and decrease in $\delta^{11}B$ have been reported for the same samples (and was less pronounced for Li and δ^7Li) (Hosono et al., 2018). All these tracers attest for the presence of hydrothermal fluids in this area, about 10km south from the central cone (aerial view), which were not sampled in this study. As in the north-western active fault area, fluids could migrate to the surface from the magma chamber through geological structures, even if the seismic activity in this zone has been quite limited since 1923 (Hosono et al., 2018).

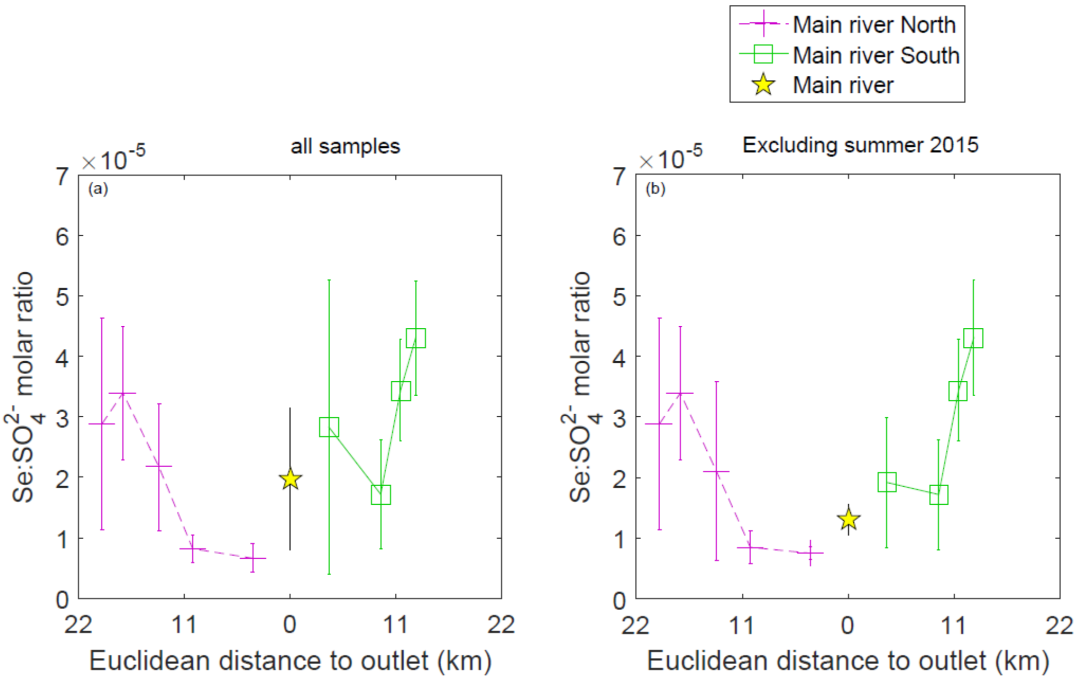

Figure 4.8. Se:SO_4^{2-} molar ratio for the two main rivers Kurokawa in the North and Shirokawa in the South and its relation with the Euclidean distance to the caldera outlet. (a) Representing the observed behaviour including all samples campaigns, and (b) excluding summer 2015, which has a clear dilution signature due to Monsoon season (heavy rainfall). However, the observed trend does not significantly change, where a decrease of Se:SO_4^{2-} molar ratios indicates higher hydrothermal input.

The ratio between the molar ratio of magmatic DIC (C_m) over magmatic SO_4^{2-} (S_m) has a high spatial variability, following heat source in the Aso caldera (Fig. 4.9). Values near the volcano are similar to the CO_2:SO_2 molar ratio observed for volcanic emissions (about 1.8 (Aiuppa et al., 2017)). The spatial differences might be related to uncertainties in the mixing model and difference in thermodynamic dependency of solubility of gases. The samples near the caldera rim have a higher C_m:S_m molar ratio than samples near heat source (> 10) because they are influenced by infiltration of water through the caldera rim and is not influenced by high temperature magmatic fluids. Moreover, the spatial differences follow different hydrothermal alterations zones.

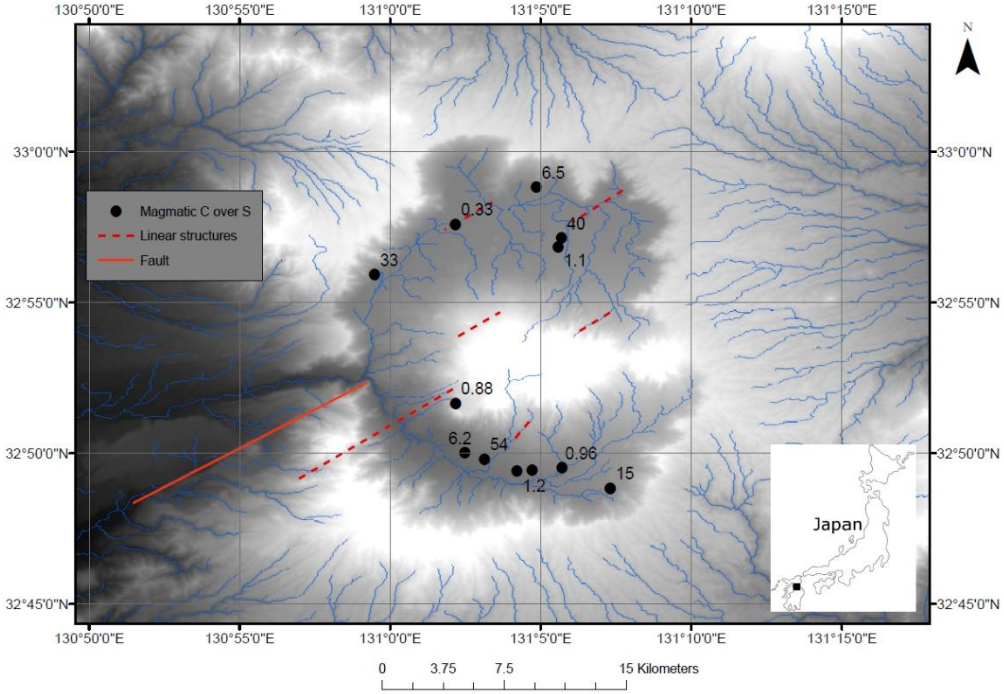

Figure 4.9. Ratios of magmatically derived DIC (C_m) over the magmatically derived sulphate (S_m) in spring samples.

Most of the magmatic CO_2 in the spring water is lost rapidly by degassing to the atmosphere and causing an increase on $\delta^{13}C$ signature (Chiodini et al., 2000). This effect was included in the mixing calculations for streams and rivers assuming a fractionation of 4‰ (Eq. 4.5). The calculations implemented in this work quantify the equivalent cationic concentration of HCO_3^- + CO_3^{2-} from magmatic DIC in the outlet of the catchment. Therefore, the hydrothermal alkalinity fraction in the river outlet, calculated by the mixing model, is 0.50 ± 0.06.

At global scale, the weathering of minerals is assumed to be induced by atmospheric CO_2 (Hartmann et al., 2014b; Hartmann and Moosdorf, 2011; Dessert et al., 2003), without taking into consideration the influence of other acids of magmatic origin, e.g. SO_2 and H_2S that produces sulphuric acid. The estimated contribution of the magmatic CO_2 to the dissolution of minerals in the Aso caldera is approximately 20 ± 3% (Table 4.2). This result is in accordance with other studies where the contribution of magmatic CO_2 on weathering rates where estimated to be up to 40% in Lesser Antilles (Rive et al., 2013) and about 10% in Iceland only due to the dissolution of magmatic-origin calcite (Jacobson et al., 2015). On the other hand, the influence of magmatic sulphur in the dissolution of minerals (dissolution with sulphuric acid) is 5 - 30%, resulting in maximum total hydrothermal influence of 55 ± 8% (acid provided by dissolution of CO_2 and SO_2). The lowest value observed is for the 2015 sample (Table 4.2), that might be associated to the monsoon season, where heavy rainfall may have diluted the hydrothermal signature (Fig. 4.8b). These results, although influenced by temporal variations, imply that the main mechanism of dissolution of primary minerals is mainly through the reaction with acids of magmatic origin (sulphuric acid and carbonic acid), and that consumption of atmospheric CO_2 by weathering is significantly less than previously believed.

Influence of other magmatic acids, e.g. hydrochloric acid, are not included because they exhibit a low influence on chemistry of waters (Cl:(SO_4^{2-} + alkalinity) molar ratio is less than 0.3).

Nevertheless, theirs effect will be to increase the total hydrothermal influence on weathering. Furthermore, the contribution of hydrothermal sulphate in surface waters might be underestimate because the sulphate fraction that comes from the soil (f_{soil}) was not accounted as of hydrothermal origin, despite that most of the sulphate in soil of the Aso caldera are influenced by the deposition of ash and pyroclastic materials (magmatic gases and eruptions).

The variation on input of magmatic S in the catchment outlet suggests that the hydrothermal rate may change with time and can follow changes on the hydrothermal activity beneath the volcanic crater (Terada et al., 2012; Terada et al., 2008). More studies should be carried on to understand if a link exists between seasonal changes and hydrothermal activity.

Table 4.2. Calculated weathering fluxes from Aso caldera and hydrothermal influence on cation rates.

Date	Discharge (m^3 s^{-1})*	Area (km^2)	Cation rate (eq h^{-1})	SO_4^{2-} rate (mol h^{-1})	Hydrothermal SO_4^{2-} rate (mol h^{-1})	Alkalinity rate (eq h^{-1})	Hydrothermal alkalinity rate (eq h^{-1})a	Hydrothermal Cation rate (eq h^{-1})
4/4/2014	16.1	386	150	35	25 ± 5	63	32 ± 4	82 ± 10
10/4/2014	13.11	386	140	28	19 ± 3	54	n.a.	38 ± 6^{b}
6/29/2015	22.26	386	70	12	2 ± 1	32	n.a.	4 ± 2^{b}

* Discharge data is from the Water Information System of the Ministry of Land, Infrastructure, Transport and Tourism (http://www1.river.go.jp/).

a This estimate does not consider CO_2 degassing from streams.

n.a. Hydrothermal alkalinity rate is not quantified because carbon isotope ratios were not measured.

b. Magmatic contribution of C is not included.

4.6 Conclusions

Because the hydrothermal system of the Aso caldera is dominated by sulphate ions (of magmatic SO_2 and H_2S source) and there is a marked contrast between the Se concentrations of hydrothermal springs (low) and of the streams and cold springs (high), we combined the Se:SO_4^{2-} molar ratio together with sulphur isotopes of sulphate to distinguish the hydrothermal contribution to the springs and streams. The Se:SO_4^{2-} molar ratio in the hydrothermal fluids is smaller than in surface waters, because Se is adsorbed onto the oxide-hydroxides of Fe and might be also retained in sulphide minerals within the hydrothermal system. Moreover, Se escapes as volatiles from the hydrothermal system, which may also decrease the Se:SO_4^{2-} molar ratio. The calculated molar ratio of magmatic DIC over magmatic SO_4^{2-} surface waters is similar to previous published values in volcanic emissions. However, this ratio can vary spatially, controlled by the influence of magmatic fluids on infiltrating waters. The water chemistry at the outlet of the Aso caldera shows a significant input of hydrothermal waters, with 20 to 70% of the SO_4^{2-} and 50 ± 6% of the DIC of magmatic origin. The contribution of magmatic CO_2, SO_2 and H_2S, influencing the dissolution of primary minerals, might represent half of the total observed cationic rate. This implies that the weathering rate induced by the atmospheric CO_2 is significantly lower than the one that would have been calculated from the total dissolved load of the river, without discriminating the origin of C and S. A detailed research is necessary to understand the link between temporal variability of the chemical composition at the outlet of the catchment and the hydrothermal activity beneath the volcanic crater. Future studies should test the application of Se:S molar ratio in other volcanic and natural systems as a complement of stable isotope ratios of sulphur.

Chapter 5: Synthesis

This thesis analysed the role of temperature in processes controlling weathering rates of carbonate rocks and in volcanic systems, mainly, because previous calculations in biogeochemical models had limitations in representing the temperature dependency on global carbonate weathering rates and the influence of hydrothermal reactions on weathering rates of volcanic systems.

This work showed that the spring water chemistry, in catchments dominated by carbonate minerals, could serve as a proxy to understand changes of soil $p\mathrm{CO_2}$ and land temperature by implementing a new global inverse calculation based on thermodynamic equations (Chapter 2). This new method led to a parameterization of global soil $p\mathrm{CO_2}$, which was implemented in global carbonate weathering calculations. For this, published spring water chemistry data in catchments dominated by carbonate rocks was collected. A data filtering method was implemented using molar ratios, stable isotopes of carbon and charge balance error, in order to collect data with a signature of calcite dissolution.

On the other hand, a new relation between alkalinity concentrations and land temperature in rivers draining carbonate rocks was found by studying global river chemistry databases (Chapter 3). The selection of the data was done by implemented more strict conditions for ideal calcite dissolution than the ones implemented in chapter 2. The behaviour of alkalinity concentration is best described by a bell-shaped dependency on temperature with a maximum between 10 and 13°C, resulting from the combination of climatic, biological, geological and hydrological processes. This novel global pattern highlights the climatic dynamics observed in water chemistry data, which can be represented in global biogeochemical models by implementing thermodynamic equations, as described in this thesis for the carbonate system. Low alkalinity concentrations observed in high temperature regions could be related to the dissolution of carbonates considering semi-closed to closed system condition with respect to soil $\mathrm{CO_2}$ available for reaction.

The role of hydrothermal reactions in weathering fluxes of active volcanoes are difficult to quantify, and previous studies focused only on magmatic $\mathrm{CO_2}$ consumption. This work tested a new method to quantify mixing processes between hydrothermal fluids and meteoric water by applying stable isotope geochemistry and $\mathrm{Se:SO_4^{2-}}$ molar ratios in water, a new proxy to quantify the sulphur budget (Chapter 4). The results showed that approximately half of the alkalinity might be from the dissolution of magmatic $\mathrm{CO_2}$ in groundwater. This magmatic $\mathrm{CO_2}$ is not represented in global weathering calculations and its global effect on weathering rates has to be tested. The total hydrothermal influence on weathering rates in the Aso caldera is quantified to be approximately half of the total cation rate. However, the input of hydrothermal fluids into surface waters is not constant over time, and it is impacted by the migration of volcanic fluids.

Global weathering parameterizations, besides including temperature and runoff effect, have to test the influence of production of acids (predominantly due to the dissolution of $\mathrm{CO_2}$ in the soil system) in order to quantify its significance at the global scale. In this work, it was also shown that, in catchments dominated by carbonate minerals, the alkalinity concentration in water percolating soils differ from the concentrations observed in river water. This difference might be linked to processes happening in the river system, mainly dilution effect, precipitation of carbonate minerals and CO_2 evasion. The global significance of these processes on the carbon cycle have to be studied.

Earth system models may test the application of thermodynamic equations, as applied in this work, to quantify the weathering of carbonate minerals at the global scale, because this system represents one of the most sensitive chemical weathering process. Furthermore, the thermodynamic equations for calcite dissolution can also be implemented in other lithological classes, besides limestones, where calcite may represent an important component, e.g. loess, marble and mixed sedimentary rocks. However, this work focused on an ideal calcite system and the influence of the dissolution of other minerals on alkalinity concentration remain to be analysed at the global scale.

Hydrothermal processes enhance the release of nutrients to the surface because of high-temperature-pressure fluid-rock interactions and the mixture between meteoric water and deep fluids. The application of the introduced new proxy, $Se:SO_4^{2-}$ molar ratios, in natural waters from volcanic fields, where SO_2 and CO_2 are the main volcanic gases in the hydrothermal systems, can serve as an indicator for deep fluids (SO_2, H_2S or sulphides) in other geological systems. In order to quantify the total hydrothermal influence, however, the mixing models should be exclusive for each chemical species because of differences in solubility of gases in water. Although hydrothermal contribution to surface waters differs for each geological setting, it may impact the global biogeochemical cycles for timescales shorter than 10^7 years (Berner and Berner, 2012), mainly because of the dissolution of minerals with sulphuric acid.

Periods of intensive volcanic activity during Earth's history, besides accounting for intensive CO_2 emission to the atmosphere, might be responsible for higher weathering rates, and consequently higher nutrient release rate, than usually assumed. Furthermore, the consumption of atmospheric CO_2 in volcanic systems through the dissolution of minerals should be distinguished from the consumption of magmatic CO_2 in the hydrothermal system because, if not accounted in the atmospheric carbon budget, it may lead to an overestimation of atmospheric CO_2 consumption rates.

Börker et al. (2018) have demonstrated that the temperature-normalized alkalinity function for inactive volcanic fields (IVF) of basaltic composition has a good linear correlation with the fraction of basaltic Holocene area in active volcanic fields (AVF). This equation might represent a good parameterization to extrapolate the effect of active volcanoes, of basalt composition, on global weathering rates. However, the hydrothermal contribution on alkalinity fluxes cannot be distinguished from other mechanisms, e.g. the constant input of fresh volcanic material with greater surface area, by implementing the equation. Future works should focus on understanding how to extrapolate the hydrothermal influence on chemical weathering at the global scale and to compare it with the other mechanisms that can increase chemical weathering fluxes.

Future studies have to focus on new global mechanistic-based methods to reduce the uncertainty related to parameterizations (i.e. runoff and soil pCO_2 parameterizations) and to include the effect of ecosystem respiration. The results from chapter 3 showed that uncertainty propagation due to parameterization are significant and should be taken into account in other studies. Finally, spatially-explicit information of composition of the rocks and the sediments at the global scale is required in order to quantify, by direct weathering calculations, the contribution of the dissolution of sulphides, secondary minerals and other phases to the carbon, sulphur, silicon and phosphorus biogeochemical cycles.

References

Abongwa, P.T., Atekwana, E.A., 2015. Controls on the chemical and isotopic composition of carbonate springs during evolution to saturation with respect to calcite. Chemical Geology, 404: 136-149.

Afsin, M., Allen, D.M., Kirste, D., Durukan, U.G., Gurel, A., Oruc, O., 2014. Mixing processes in hydrothermal spring systems and implications for interpreting geochemical data: a case study in the Cappadocia region of Turkey. Hydrogeology Journal, 22(1): 7-23.

Aiuppa, A., Allard, P., D'Alessandro, W., Michel, A., Parello, F., Treuil, M., Valenza, M., 2000. Mobility and fluxes of major, minor and trace metals during basalt weathering and groundwater transport at Mt. Etna volcano (Sicily). Geochimica et Cosmochimica Acta, 64(11): 1827-1841.

Aiuppa, A., Fischer, T.P., Plank, T., Robidoux, P., Di Napoli, R., 2017. Along-arc, inter-arc and arc-to-arc variations in volcanic gas CO2/ST ratios reveal dual source of carbon in arc volcanism. Earth-science reviews, 168: 24-47.

Amiotte-Suchet, P., Probst, J.-L., 1995. A global model for present-day atmospheric/soil CO2 consumption by chemical erosion of continental rocks (GEM-CO2). Tellus B, 47(1-2): 273-280.

Amiotte-Suchet, P., Probst, J.L., 1993. Modelling of atmospheric CO2 consumption by chemical weathering of rocks: application to the Garonne, Congo and Amazon basins. Chemical Geology, 107(3-4): 205-210.

Amouroux, D., Pécheyran, C., Donard, O.F., 2000. Formation of volatile selenium species in synthetic seawater under light and dark experimental conditions. Applied Organometallic Chemistry, 14(5): 236-244.

Amundson, R.G., Davidson, E.A., 1990. Carbon dioxide and nitrogenous gases in the soil atmosphere. Journal of Geochemical Exploration, 38(1-2): 13-41.

Arvidson, R.S., Mackenzie, F.T., Guidry, M., 2006. MAGic: A Phanerozoic model for the geochemical cycling of major rock-forming components. American Journal of Science, 306(3): 135-190.

Banerjee, S., Helgason, B., Wang, L., Winsley, T., Ferrari, B.C., Siciliano, S.D., 2016. Legacy effects of soil moisture on microbial community structure and N2O emissions. Soil Biology and Biochemistry, 95: 40-50.

Barge, L., Branscomb, E., Brucato, J., Cardoso, S., Cartwright, J., Danielache, S., Galante, D., Kee, T., Miguel, Y., Mojzsis, S., 2017. Thermodynamics, disequilibrium, evolution: Far-from-equilibrium geological and chemical considerations for origin-of-life research. Origins of Life and Evolution of Biospheres, 47(1): 39-56.

Barnes, C., Allison, G., 1988. Tracing of water movement in the unsaturated zone using stable isotopes of hydrogen and oxygen. Journal of Hydrology, 100(1-3): 143-176.

Basu, R., Haque, S.E., Tang, J., Ji, J., Johannesson, K.H., 2007. Evolution of selenium concentrations and speciation in groundwater flow systems: Upper Floridan (Florida) and Carrizo Sand (Texas) aquifers. Chemical Geology, 246(3-4): 147-169.

Batjes, N., 2005. ISRIC-WISE global data set of derived soil properties on a 0.5 by 0.5 degree grid (Version 3.0). ISRIC-World Soil Information, Wageningen.

Beaulieu, E., Goddéris, Y., Donnadieu, Y., Labat, D., Roelandt, C., 2012. High sensitivity of the continental-weathering carbon dioxide sink to future climate change. Nature Climate Change, 2(5): 346.

Beaulieu, E., Goddéris, Y., Labat, D., Roelandt, C., Calmels, D., Gaillardet, J., 2011. Modeling of water-rock interaction in the Mackenzie basin: Competition between sulfuric and carbonic acids. Chemical Geology, 289(1-2): 114-123.

References

Berner, E.K., Berner, R.A., 2012. Global environment: water, air, and geochemical cycles. Princeton University Press, NJ, USA, 488 pp.

Berner, R., 1975. The role of magnesium in the crystal growth of calcite and aragonite from sea water. Geochimica et Cosmochimica Acta, 39(4): 489-504.

Berner, R., Lasaga, A., Garrels, R., 1983. The carbonate-silicate geochemical cycle and its effect on atmospheric carbon dioxide over the past 100 million years. American Journal of Science, 283: 641-683.

Beusen, A., Bouwman, A., Dürr, H., Dekkers, A., Hartmann, J., 2009. Global patterns of dissolved silica export to the coastal zone: Results from a spatially explicit global model. Global Biogeochemical Cycles, 23(4).

Blagodatsky, S., Smith, P., 2012. Soil physics meets soil biology: towards better mechanistic prediction of greenhouse gas emissions from soil. Soil Biology and Biochemistry, 47: 78-92.

Bluth, G.J., Kump, L.R., 1994. Lithologic and climatologic controls of river chemistry. Geochimica et Cosmochimica Acta, 58(10): 2341-2359.

Bono, P., Dreybrodt, W., Ercole, S., Percopo, C., Vosbeck, K., 2001. Inorganic calcite precipitation in Tartare karstic spring (Lazio, central Italy): field measurements and theoretical prediction on depositional rates. Environmental Geology, 41(3-4): 305-313.

Börker, J., Hartmann, J., Romero-Mujalli, G., Li, G., 2018. Aging of basalt volcanic systems and decreasing CO 2 consumption by weathering. Earth Surface Dynamics: 1-9.

Börsig, N., Scheinost, A.C., Shaw, S., Schild, D., Neumann, T., 2017. Uptake mechanisms of selenium oxyanions during the ferrihydrite-hematite recrystallization. Geochimica et Cosmochimica Acta, 206: 236-253.

Böttcher, M.E., Brumsack, H.-J., De Lange, G.J., Robertson, A., 1998. Sulfate reduction and related stable isotope (34S,18O) variations in interstitial waters from the Eastern Mediterranean, PROCEEDINGS-OCEAN DRILLING PROGRAM SCIENTIFIC RESULTS. NATIONAL SCIENCE FOUNDATION, pp. 365-376.

Brantley, S.L., 2008. Kinetics of mineral dissolution. In: Brantley, S.L., Kubicki, J.D., White, A.F. (Eds.), Kinetics of water-rock interaction. Springer, pp. 151-210.

Brook, G.A., Folkoff, M.E., Box, E.O., 1983. A world model of soil carbon dioxide. Earth Surface Processes and Landforms, 8(1): 79-88.

Calabrese, S., 2009. Atmospheric Deposition Of Volcanogenic Major And Trace Elements On Mt. Etna (Italy). PhD Dissertation, University of Palermo, Italy.

Calmels, D., Gaillardet, J., Brenot, A., France-Lanord, C., 2007. Sustained sulfide oxidation by physical erosion processes in the Mackenzie River basin: climatic perspectives. Geology, 35(11): 1003-1006.

Calmels, D., Gaillardet, J., François, L., 2014. Sensitivity of carbonate weathering to soil CO2 production by biological activity along a temperate climate transect. Chemical Geology, 390: 74-86.

Cartwright, J., Hui, D., 2015. Soil respiration patterns and controls in limestone cedar glades. Plant and Soil, 389(1-2): 157-169.

Cerling, T.E., Solomon, D.K., Quade, J., Bowman, J.R., 1991. On the isotopic composition of carbon in soil carbon dioxide. Geochimica et Cosmochimica Acta, 55(11): 3403-3405.

Chiodini, G., Frondini, F., Cardellini, C., Parello, F., Peruzzi, L., 2000. Rate of diffuse carbon dioxide Earth degassing estimated from carbon balance of regional aquifers: the case of central Apennine, Italy. Journal of Geophysical Research: Solid Earth, 105(B4): 8423-8434.

Chiodini, G., Frondini, F., Kerrick, D., Rogie, J., Parello, F., Peruzzi, L., Zanzari, A., 1999. Quantification of deep CO2 fluxes from Central Italy. Examples of carbon balance for regional aquifers and of soil diffuse degassing. Chemical Geology, 159(1-4): 205-222.

Chou, L., Garrels, R.M., Wollast, R., 1989. Comparative study of the kinetics and mechanisms of dissolution of carbonate minerals. Chemical geology, 78(3-4): 269-282.

Conde, J., Sanz Alaejos, M., 1997. Selenium concentrations in natural and environmental waters. Chemical Reviews, 97(6): 1979-2004.

Cooke, T.D., Bruland, K.W., 1987. Aquatic chemistry of selenium: evidence of biomethylation. Environmental science & technology, 21(12): 1214-1219.

Cox, P.M., Betts, R.A., Jones, C.D., Spall, S.A., Totterdell, I.J., 2000. Acceleration of global warming due to carbon-cycle feedbacks in a coupled climate model. Nature, 408(6809): 184.

Dandurand, J., Gout, R., Hoefs, J., Menschel, G., Schott, J., Usdowski, E., 1982. Kinetically controlled variations of major components and carbon and oxygen isotopes in a calcite-precipitating spring. Chemical geology, 36(3-4): 299-315.

Deines, P., Langmuir, D., Harmon, R.S., 1974. Stable carbon isotope ratios and the existence of a gas phase in the evolution of carbonate ground waters. Geochimica et Cosmochimica Acta, 38(7): 1147-1164.

Delmelle, P., Bernard, A., Kusakabe, M., Fischer, T., Takano, B., 2000. Geochemistry of the magmatic–hydrothermal system of Kawah Ijen volcano, East Java, Indonesia. Journal of Volcanology and Geothermal research, 97(1-4): 31-53.

Dessert, C., Dupré, B., Gaillardet, J., François, L.M., Allegre, C.J., 2003. Basalt weathering laws and the impact of basalt weathering on the global carbon cycle. Chemical Geology, 202(3-4): 257-273.

Dessert, C., Gaillardet, J., Dupre, B., Schott, J., Pokrovsky, O.S., 2009. Fluxes of high-versus low-temperature water–rock interactions in aerial volcanic areas: example from the Kamchatka Peninsula, Russia. Geochimica et Cosmochimica Acta, 73(1): 148-169.

Deverel, S., Fujii, R., 1988. Processes affecting the distribution of selenium in shallow groundwater of agricultural areas, western San Joaquin Valley, California. Water Resources Research, 24(4): 516-524.

Diamond, M., Hirst, D., Winder, L., Crawshaw, D.H., Prigg, R.F., 1992. The effect of liming agricultural land on the chemistry and biology of the River Esk, north-west England. Environmental pollution, 78(1-3): 179-185.

Doctor, D.H., Kendall, C., Sebestyen, S.D., Shanley, J.B., Ohte, N., Boyer, E.W., 2008. Carbon isotope fractionation of dissolved inorganic carbon (DIC) due to outgassing of carbon dioxide from a headwater stream. Hydrological Processes: An International Journal, 22(14): 2410-2423.

Dorigo, W., Gruber, A., De Jeu, R., Wagner, W., Stacke, T., Loew, A., Albergel, C., Brocca, L., Chung, D., Parinussa, R., 2015. Evaluation of the ESA CCI soil moisture product using ground-based observations. Remote Sensing of Environment, 162: 380-395.

Dörr, H., Münnich, K.O., 1980. Carbon-14 and carbon-13 in soil CO2. Radiocarbon, 22(3): 909-918.

Dove, P.M., Hochella, M.F., 1993. Calcite precipitation mechanisms and inhibition by orthophosphate: In situ observations by Scanning Force Microscopy. Geochimica et cosmochimica acta, 57(3): 705-714.

Dreher, G., Finkelman, R., 1992. Selenium mobilization in a surface coal mine, Powder River Basin, Wyoming, USA. Environmental Geology and Water Sciences, 19(3): 155-167.

Drever, J.I., 1997. The Geochemistry of Natural Waters: Surface and Groundwater Environments, 436 pp. Prentice Hall, Upper Saddle River, NJ.

Dreybrodt, W., Buhmann, D., Michaelis, J., Usdowski, E., 1992. Geochemically controlled calcite precipitation by CO2 outgassing: Field measurements of precipitation rates in comparison to theoretical predictions. Chemical Geology, 97(3-4): 285-294.

Dreybrodt, W., Lauckner, J., Zaihua, L., Svensson, U., Buhmann, D., 1996. The kinetics of the reaction CO2+ H2O→ H++ HCO3− as one of the rate limiting steps for the dissolution of calcite in the system H2O - CO2 - CaCO3. Geochimica et Cosmochimica Acta, 60(18): 3375-3381.

References

Dupré, B., Dessert, C., Oliva, P., Goddéris, Y., Viers, J., François, L., Millot, R., Gaillardet, J., 2003. Rivers, chemical weathering and Earth's climate. Comptes Rendus Geoscience, 335(16): 1141-1160.

Dürr, H.H., Meybeck, M., Dürr, S.H., 2005. Lithologic composition of the Earth's continental surfaces derived from a new digital map emphasizing riverine material transfer. Global Biogeochemical Cycles, 19(4).

Edwards, C., Reichle, D., Crossley, D., 1973. The role of soil invertebrates in turnover of organic matter and nutrients, Analysis of temperate forest ecosystems. Springer, pp. 147-172.

Egli, M., Mirabella, A., Sartori, G., 2008. The role of climate and vegetation in weathering and clay mineral formation in late Quaternary soils of the Swiss and Italian Alps. Geomorphology, 102(3-4): 307-324.

Epron, D., Farque, L., Lucot, É., Badot, P.-M., 1999. Soil CO2 efflux in a beech forest: dependence on soil temperature and soil water content. Annals of Forest Science, 56(3): 221-226.

Faulkner, T., 2006. Limestone dissolution in phreatic conditions at maximum rates and in pure, cold, water. Cave and Karst Science, 33(1): 11.

Fekete, B.M., Vörösmarty, C.J., Grabs, W., 2002. High-resolution fields of global runoff combining observed river discharge and simulated water balances. Global Biogeochemical Cycles, 16(3): 15-1-15-10.

Fellowes, J., Pattrick, R., Boothman, C., Al Lawati, W., van Dongen, B., Charnock, J., Lloyd, J., Pearce, C., 2013. Microbial selenium transformations in seleniferous soils. European journal of soil science, 64(5): 629-638.

Fernández-Martínez, A., Charlet, L., 2009. Selenium environmental cycling and bioavailability: a structural chemist point of view. Reviews in Environmental Science and Bio/Technology, 8(1): 81-110.

Floor, G., Calabrese, S., Román-Ross, G., Aiuppa, A., 2011. Selenium mobilization in soils due to volcanic derived acid rain: an example from Mt Etna volcano, Sicily. Chemical Geology, 289(3-4): 235-244.

Floor, G.H., Román-Ross, G., 2012. Selenium in volcanic environments: a review. Applied Geochemistry, 27(3): 517-531.

Foster, G.L., Vance, D., 2006. Negligible glacial–interglacial variation in continental chemical weathering rates. Nature, 444(7121): 918.

Friedlingstein, P., Cox, P., Betts, R., Bopp, L., von Bloh, W., Brovkin, V., Cadule, P., Doney, S., Eby, M., Fung, I., 2006. Climate–carbon cycle feedback analysis: results from the C4MIP model intercomparison. Journal of climate, 19(14): 3337-3353.

Frisia, S., Fairchild, I.J., Fohlmeister, J., Miorandi, R., Spötl, C., Borsato, A., 2011. Carbon mass-balance modelling and carbon isotope exchange processes in dynamic caves. Geochimica et Cosmochimica Acta, 75(2): 380-400.

Gaillardet, J., Calmels, D., Romero-Mujalli, G., Zakharova, E., Hartmann, J., 2018. Global climate control on carbonate weathering intensity. Chemical Geology.

Gaillardet, J., Dupré, B., Louvat, P., Allegre, C., 1999. Global silicate weathering and CO2 consumption rates deduced from the chemistry of large rivers. Chemical geology, 159(1-4): 3-30.

Gaillardet, J., Rad, S., Rive, K., Louvat, P., Gorge, C., Allègre, C.J., Lajeunesse, E., 2011. Orography-driven chemical denudation in the Lesser Antilles: Evidence for a new feed-back mechanism stabilizing atmospheric CO2. American journal of science, 311(10): 851-894.

Gaumont-Guay, D., Black, T.A., Griffis, T.J., Barr, A.G., Jassal, R.S., Nesic, Z., 2006. Interpreting the dependence of soil respiration on soil temperature and water content in a boreal aspen stand. Agricultural and Forest Meteorology, 140(1-4): 220-235.

Giggenbach, W.F., Soto, R.C., 1992. Isotopic and chemical composition of water and steam discharges from volcanic-magmatic-hydrothermal systems of the Guanacaste Geothermal Province, Costa Rica. Applied Geochemistry, 7(4): 309-332.

Gillon, M., Barbecot, F., Gibert, E., Alvarado, J.C., Marlin, C., Massault, M., 2009. Open to closed system transition traced through the TDIC isotopic signature at the aquifer recharge stage, implications for groundwater 14C dating. Geochimica et Cosmochimica Acta, 73(21): 6488-6501.

Goddéris, Y., Brantley, S.L., François, L., Schott, J., Pollard, D., Déqué, M., Dury, M., 2013. Rates of consumption of atmospheric CO2 through the weathering of loess during the next 100 yr of climate change. Biogeosciences, 10: 135-148.

Goddéris, Y., François, L.M., Probst, A., Schott, J., Moncoulon, D., Labat, D., Viville, D., 2006. Modelling weathering processes at the catchment scale: The WITCH numerical model. Geochimica et Cosmochimica Acta, 70(5): 1128-1147.

Goll, D.S., Moosdorf, N., Hartmann, J., Brovkin, V., 2014. Climate-driven changes in chemical weathering and associated phosphorus release since 1850: Implications for the land carbon balance. Geophysical Research Letters, 41(10): 3553-3558.

Gombert, P., 2002. Role of karstic dissolution in global carbon cycle. Global and Planetary Change, 33(1-2): 177-184.

Greenland, L., Aruscavage, P., 1986. Volcanic emission of Se, Te, and As from Kilauea volcano, Hawaii. Journal of volcanology and geothermal research, 27(1-2): 195-201.

Hamilton, S.K., Kurzman, A.L., Arango, C., Jin, L., Robertson, G.P., 2007. Evidence for carbon sequestration by agricultural liming. Global Biogeochemical Cycles, 21(2).

Hartmann, J., 2009. Bicarbonate-fluxes and CO2-consumption by chemical weathering on the Japanese Archipelago—application of a multi-lithological model framework. Chemical Geology, 265(3-4): 237-271.

Hartmann, J., Dürr, H.H., Moosdorf, N., Meybeck, M., Kempe, S., 2012. The geochemical composition of the terrestrial surface (without soils) and comparison with the upper continental crust. International Journal of Earth Sciences, 101(1): 365-376.

Hartmann, J., Jansen, N., Dürr, H.H., Kempe, S., Köhler, P., 2009. Global CO2-consumption by chemical weathering: What is the contribution of highly active weathering regions? Global and Planetary Change, 69(4): 185-194.

Hartmann, J., Jansen, N., Kempe, S., Dürr, H.H., 2007. Geochemistry of the river Rhine and the upper Danube: Recent trends and lithological influence on baselines. Journal of Environmental Science for Sustainable Society, 1: 39-46.

Hartmann, J., Lauerwald, R., Moosdorf, N., 2014a. A brief overview of the GLObal RIver CHemistry Database, GLORICH. Procedia Earth and Planetary Science, 10: 23-27.

Hartmann, J., Moosdorf, N., 2011. Chemical weathering rates of silicate-dominated lithological classes and associated liberation rates of phosphorus on the Japanese Archipelago—Implications for global scale analysis. Chemical Geology, 287(3-4): 125-157.

Hartmann, J., Moosdorf, N., 2012. The new global lithological map database GLiM: A representation of rock properties at the Earth surface. Geochemistry, Geophysics, Geosystems, 13(12): 1-37.

Hartmann, J., Moosdorf, N., Lauerwald, R., Hinderer, M., West, A.J., 2014b. Global chemical weathering and associated P-release—The role of lithology, temperature and soil properties. Chemical Geology, 363: 145-163.

Hase, H., Hashimoto, T., Sakanaka, S.y., Kanda, W., Tanaka, Y., 2005. Hydrothermal system beneath Aso volcano as inferred from self-potential mapping and resistivity structure. Journal of Volcanology and Geothermal Research, 143(4): 259-277.

Hellevang, H., Pham, V.T., Aagaard, P., 2013. Kinetic modelling of CO2–water–rock interactions. International Journal of Greenhouse Gas Control, 15: 3-15.

Hercod, D.J., Brady, P.V., Gregory, R.T., 1998. Catchment-scale coupling between pyrite oxidation and calcite weathering. Chemical Geology, 151(1-4): 259-276.

Herman, J.S., Lorah, M.M., 1987. CO2 outgassing and calcite precipitation in Falling Spring Creek, Virginia, USA. Chemical Geology, 62(3-4): 251-262.

Hijmans, R.J., Cameron, S.E., Parra, J.L., Jones, P.G., Jarvis, A., 2005. Very high resolution interpolated climate surfaces for global land areas. International journal of climatology, 25(15): 1965-1978.

Hirner, A.V., Feldmann, J., Krupp, E., Gruemping, R., Goguel, R., Cullen, W.R., 1998. Metal (loid) organic compounds in geothermal gases and waters. Organic Geochemistry, 29(5-7): 1765-1778.

Hoefs, J., 2009. Stable isotope geochemistry. Springer, Berlin, Germany, 285 pp.

Holm, N.G., Andersson, E., 2005. Hydrothermal simulation experiments as a tool for studies of the origin of life on earth and other terrestrial planets: a review. Astrobiology, 5(4): 444-460.

Hosono, T., Alvarez, K., Lin, I.-T., Shimada, J., 2015. Nitrogen, carbon, and sulfur isotopic change during heterotrophic (Pseudomonas aureofaciens) and autotrophic (Thiobacillus denitrificans) denitrification reactions. Journal of contaminant hydrology, 183: 72-81.

Hosono, T., Hartmann, J., Louvat, P., Amann, T., Washington, K.E., West, A.J., Okamura, K., Böttcher, M.E., Gaillardet, J., 2018. Earthquake-induced structural deformations enhance long-term solute fluxes from active volcanic systems. Scientific reports, 8(1): 14809.

Hosono, T., Lorphensriand, O., Onodera, S.-i., Okawa, H., Nakano, T., Yamanaka, T., Tsujimura, M., Taniguchi, M., 2014. Different isotopic evolutionary trends of δ34S and δ18O compositions of dissolved sulfate in an anaerobic deltaic aquifer system. Applied geochemistry, 46: 30-42.

Huang, F., Zhang, C., Xie, Y., Li, L., Cao, J., 2015. Inorganic carbon flux and its source in the karst catchment of Maocun, Guilin, China. Environmental Earth Sciences, 74(2): 1079-1089.

Ichiyanagi, K., Tanoue, M., Science, I.M.W.G.o.t.J.S.o.H., 2016. Spatial analysis of annual mean stable isotopes in precipitation across Japan based on an intensive observation period throughout 2013. Isotopes in environmental and health studies, 52(4-5): 353-362.

Ilstedt, U., Nordgren, A., Malmer, A., 2000. Optimum soil water for soil respiration before and after amendment with glucose in humid tropical acrisols and a boreal mor layer. Soil Biology and Biochemistry, 32(11-12): 1591-1599.

Jacobson, A.D., Andrews, M.G., Lehn, G.O., Holmden, C., 2015. Silicate versus carbonate weathering in Iceland: New insights from Ca isotopes. Earth and Planetary Science Letters, 416: 132-142.

Jacobson, R.L., Langmuir, D., 1970. The Chemical History of Some Spring Waters in Carbonate Rocks a. Groundwater, 8(3): 5-9.

Jacobson, R.L., Langmuir, D., 1974. Controls on the quality variations of some carbonate spring waters. Journal of Hydrology, 23(3-4): 247-265.

Jeelani, G.H., Bhat, N.A., Shivanna, K., Bhat, M.Y., 2011. Geochemical characterization of surface water and spring water in SE Kashmir Valley, western Himalaya: Implications to water–rock interaction. Journal of Earth System Science, 120(5): 921-932.

Kanduč, T., Mori, N., Kocman, D., Stibilj, V., Grassa, F., 2012. Hydrogeochemistry of Alpine springs from North Slovenia: Insights from stable isotopes. Chemical Geology, 300-301: 40-54.

Karimi, H., Raeisi, E., Bakalowicz, M., 2005. Characterising the main karst aquifers of the Alvand basin, northwest of Zagros, Iran, by a hydrogeochemical approach. Hydrogeology Journal, 13(5): 787-799.

Karolytė, R., Johnson, G., Serno, S., Gilfillan, S.M., 2017. The influence of water-rock reactions and O isotope exchange with CO2 on water stable isotope composition of CO2 springs in SE Australia. Energy Procedia, 114: 3832-3839.

Kempe, S., 1979. Carbon in the freshwater cycle. The global carbon cycle, 13: 317-342.

Kohfahl, C., Sprenger, C., Herrera, J.B., Meyer, H., Chacón, F.F., Pekdeger, A., 2008. Recharge sources and hydrogeochemical evolution of groundwater in semiarid and karstic environments: A field study in the Granada Basin (Southern Spain). Applied Geochemistry, 23(4): 846-862.

References

Kotra, J.P., Finnegan, D.L., Zoller, W.H., Hart, M.A., Moyers, J.L., 1983. El Chichón: Composition of plume gases and particles. Science, 222(4627): 1018-1021.

Kuzyakov, Y., 2006. Sources of CO2 efflux from soil and review of partitioning methods. Soil biology and biochemistry, 38(3): 425-448.

Langmuir, D., 1971. The geochemistry of some carbonate ground waters in central Pennsylvania. Geochimica et Cosmochimica Acta, 35(10): 1023-1045.

Lasaga, A.C., 1984. Chemical kinetics of water-rock interactions. Journal of geophysical research: solid earth, 89(B6): 4009-4025.

Lauerwald, R., Laruelle, G.G., Hartmann, J., Ciais, P., Regnier, P.A., 2015. Spatial patterns in CO2 evasion from the global river network. Global Biogeochemical Cycles, 29(5): 534-554.

Layton-Matthews, D., Leybourne, M.I., Peter, J.M., Scott, S.D., Cousens, B., Eglington, B.M., 2013. Multiple sources of selenium in ancient seafloor hydrothermal systems: Compositional and Se, S, and Pb isotopic evidence from volcanic-hosted and volcanic-sediment-hosted massive sulfide deposits of the Finlayson Lake District, Yukon, Canada. Geochimica et Cosmochimica Acta, 117: 313-331.

Lellei-Kovács, E., Botta-Dukát, Z., De Dato, G., Estiarte, M., Guidolotti, G., Kopittke, G.R., Kovács-Láng, E., Kröel-Dulay, G., Larsen, K.S., Peñuelas, J., 2016. Temperature dependence of soil respiration modulated by thresholds in soil water availability across European shrubland ecosystems. Ecosystems, 19(8): 1460-1477.

Lerman, A., Mackenzie, F., Garrels, R., 1975. Modeling of geochemical cycles: Phosphorus as an example. Geological Society of America Memoir, 142: 205-218.

Li, G., Hartmann, J., Derry, L.A., West, A.J., You, C.-F., Long, X., Zhan, T., Li, L., Li, G., Qiu, W., 2016. Temperature dependence of basalt weathering. Earth and Planetary Science Letters, 443: 59-69.

Li, G., Ji, J., Chen, J., Kemp, D.B., 2009. Evolution of the Cenozoic carbon cycle: The roles of tectonics and CO2 fertilization. Global Biogeochemical Cycles, 23: 1-11.

Li, S.-L., Calmels, D., Han, G., Gaillardet, J., Liu, C.-Q., 2008. Sulfuric acid as an agent of carbonate weathering constrained by δ13CDIC: Examples from Southwest China. Earth and Planetary Science Letters, 270(3): 189-199.

Li, S.-L., Liu, C.-Q., Li, J., Lang, Y.-C., Ding, H., Li, L., 2010. Geochemistry of dissolved inorganic carbon and carbonate weathering in a small typical karstic catchment of Southwest China: Isotopic and chemical constraints. Chemical Geology, 277(3-4): 301-309.

Liu, Y.Y., Dorigo, W.A., Parinussa, R.M., de Jeu, R.A.M., Wagner, W., McCabe, M.F., Evans, J.P., van Dijk, A.I.J.M., 2012. Trend-preserving blending of passive and active microwave soil moisture retrievals. Remote Sensing of Environment, 123: 280-297.

Liu, Z., Dreybrodt, W., Wang, H., 2010. A new direction in effective accounting for the atmospheric CO2 budget: Considering the combined action of carbonate dissolution, the global water cycle and photosynthetic uptake of DIC by aquatic organisms. Earth-Science Reviews, 99(3-4): 162-172.

Liu, Z., Li, Q., Sun, H., Wang, J., 2007. Seasonal, diurnal and storm-scale hydrochemical variations of typical epikarst springs in subtropical karst areas of SW China: soil CO2 and dilution effects. Journal of Hydrology, 337(1-2): 207-223.

Liu, Z., Yuan, D., Dreybrodt, W., 2005. Comparative study of dissolution rate-determining mechanisms of limestone and dolomite. Environmental Geology, 49(2): 274-279.

Lloyd, J., Taylor, J.A., 1994. On the Temperature Dependence of Soil Respiration. Functional Ecology, 8(3): 315-323.

Long, X., Sun, Z., Zhou, A., Liu, D., 2015. Hydrogeochemical and isotopic evidence for flow paths of karst waters collected in the Heshang Cave, Central China. Journal of Earth Science, 26(1): 149-156.

López-Chicano, M., Bouamama, M., Vallejos, A., Pulido-Bosch, A., 2001. Factors which determine the hydrogeochemical behaviour of karstic springs. A case study from the Betic Cordilleras, Spain. Applied Geochemistry, 16(9): 1179-1192.

Louvat, P., Allègre, C.J., 1997. Present denudation rates on the island of Reunion determined by river geochemistry: basalt weathering and mass budget between chemical and mechanical erosions. Geochimica et Cosmochimica Acta, 61(17): 3645-3669.

Louvat, P., Allègre, C.J., 1998. Riverine erosion rates on Sao Miguel volcanic island, Azores archipelago. Chemical Geology, 148(3-4): 177-200.

Louvat, P., Gislason, S.R., Allègre, C.J., 2008. Chemical and mechanical erosion rates in Iceland as deduced from river dissolved and solid material. American Journal of Science, 308(5): 679-726.

Mackenzie, F.T., Garrels, R.M., 1966. Chemical mass balance between rivers and oceans. American Journal of Science, 264(7): 507-525.

Martens, B., Miralles, D.G., Lievens, H., van der Schalie, R., de Jeu, R.A.M., Fernández-Prieto, D., Beck, H.E., Dorigo, W.A., Verhoest, N.E.C., 2017. GLEAM v3: satellite-based land evaporation and root-zone soil moisture. Geoscientific Model Development, 10(5): 1903-1925.

Martin, J.B., 2017. Carbonate minerals in the global carbon cycle. Chemical Geology, 449: 58-72.

Martin, W., Baross, J., Kelley, D., Russell, M.J., 2008. Hydrothermal vents and the origin of life. Nature Reviews Microbiology, 6(11): 805.

Martin, W., Russell, M.J., 2006. On the origin of biochemistry at an alkaline hydrothermal vent. Philosophical Transactions of the Royal Society B: Biological Sciences, 362(1486): 1887-1926.

Marx, A., Dusek, J., Jankovec, J., Sanda, M., Vogel, T., Van Geldern, R., Hartmann, J., Barth, J., 2017. A review of CO2 and associated carbon dynamics in headwater streams: A global perspective. Reviews of Geophysics, 55(2): 560-585.

Mason, E., Edmonds, M., Turchyn, A.V., 2017. Remobilization of crustal carbon may dominate volcanic arc emissions. Science, 357(6348): 290-294.

Mast, M.A., Drever, J.I., 1987. The effect of oxalate on the dissolution rates of oligoclase and tremolite. Geochimica et Cosmochimica Acta, 51(9): 2559-2568.

McNeal, J.M., Balistrieri, L.S., 1989. Geochemistry and occurrence of selenium: an overview. Selenium in Agriculture and the Environment(seleniuminagric): 1-13.

Meybeck, M., 1987. Global chemical weathering of surficial rocks estimated from river dissolved loads. American journal of science, 287(5): 401-428.

Mielnick, P., Dugas, W.A., 2000. Soil CO2 flux in a tallgrass prairie. Soil Biology and Biochemistry, 32(2): 221-228.

Milanović, P., 2014. Hydraulic properties of karst groundwater and its impacts on large structures, H2Karst Research in Limestone Hydrogeology. Springer, pp. 19-48.

Miralles, D.G., Holmes, T.R.H., De Jeu, R.A.M., Gash, J.H., Meesters, A.G.C.A., Dolman, A.J., 2011. Global land-surface evaporation estimated from satellite-based observations. Hydrol. Earth Syst. Sci., 15(2): 453-469.

Miyabuchi, Y., Terada, A., 2009. Subaqueous geothermal activity revealed by lacustrine sediments of the acidic Nakadake crater lake, Aso Volcano, Japan. Journal of Volcanology and Geothermal Research, 187(1-2): 140-145.

Moosdorf, N., Hartmann, J., Lauerwald, R., Hagedorn, B., Kempe, S., 2011. Atmospheric CO2 consumption by chemical weathering in North America. Geochimica et Cosmochimica Acta, 75(24): 7829-7854.

Moral, F., Cruz-Sanjulián, J.J., Olías, M., 2008. Geochemical evolution of groundwater in the carbonate aquifers of Sierra de Segura (Betic Cordillera, southern Spain). Journal of Hydrology, 360(1): 281-296.

Moreira, A., Fageria, N.K., 2010. Liming influence on soil chemical properties, nutritional status and yield of alfalfa grown in acid soil. Revista Brasileira de Ciencia do solo, 34(4): 1231-1239.

Nakada, S., Miyabuchi, Y., Watanabe, K., Sudo, Y., Hoshizumi, H., Uto, K., Matsumoto, A., Shimizu, H., 2003. Field Guidebook, A3: Unzen and Aso Volcanoes. In: Japan, T.V.S.o. (Ed.), XXIII General

Assembly of the International Union of Geodesy and Geophysics: IUGG. The Volcanological Society of Japan, Tokyo, Japan, pp. 67-104.

Nakamaru, Y., Tagami, K., Uchida, S., 2005. Distribution coefficient of selenium in Japanese agricultural soils. Chemosphere, 58(10): 1347-1354.

Norton, K.P., Molnar, P., Schlunegger, F., 2014. The role of climate-driven chemical weathering on soil production. Geomorphology, 204: 510-517.

Okumura, A., Hosono, T., Boateng, D., Shimada, J., 2018. Evaluations of the downward velocity of soil water movement in the unsaturated zone in a groundwater recharge area using δ18 O tracer: the Kumamoto region, southern Japan. Geologia Croatica, 71(2): 65-82.

Ono, K., Kubotera, A., Ota, K., 1981. Aso VolcanoField Excursion Guide to Sakurajima, Kirishima and Aso Volcanoes. In: Kubotera, A. (Ed.), Field Excursion Guide to Sakurajima, Kirishima and Aso Volcanoes. IAVCEI Symposium on Arc Volcanism, Tokyo and Hakone. Volcanological Society of Japan, Tokyo, Japan, pp. 33-52.

Ono, K., Watanabe, K., Hoshizumi, H., Ikebe, S.-i., 1995. Ash eruption of the Naka-dake crater, Aso volcano, southwestern Japan. Journal of volcanology and geothermal research, 66(1-4): 137-148.

Özkul, M., Gökgöz, A., HorvatinčIć, N., 2010. Depositional properties and geochemistry of Holocene perched springline tufa deposits and associated spring waters: a case study from the Denizli Province, Western Turkey. Geological Society, London, Special Publications, 336(1): 245-262.

Parkhurst, D.L., Appelo, C., 1999. User's Guide to PHREEQC (version 2): A Computer Program for Speciation, Batch-reaction, One-dimensional Transport, and Inverse Geochemical Calculations.

Perrin, A.-S., Probst, A., Probst, J.-L., 2008. Impact of nitrogenous fertilizers on carbonate dissolution in small agricultural catchments: implications for weathering CO2 uptake at regional and global scales. Geochimica et Cosmochimica Acta, 72(13): 3105-3123.

Pu, T., He, Y., Zhang, T., Wu, J., Zhu, G., Chang, L., 2013. Isotopic and geochemical evolution of ground and river waters in a karst dominated geological setting: a case study from Lijiang basin, South-Asia monsoon region. Applied geochemistry, 33: 199-212.

Qibo, H., Xiaoqun, Q., Qiyong, Y., Pengyu, L., Jinsong, Z., 2016. Identification of dissolved sulfate sources and the role of sulfuric acid in carbonate weathering using δ13CDIC and δ34S in karst area, northern China. Environmental Earth Sciences, 75(1): 51.

Queffurus, M., Barnes, S.-J., 2015. A review of sulfur to selenium ratios in magmatic nickel–copper and platinum-group element deposits. Ore Geology Reviews, 69: 301-324.

Rad, S., Louvat, P., Gorge, C., Gaillardet, J., Allègre, C.J., 2006. River dissolved and solid loads in the Lesser Antilles: new insight into basalt weathering processes. Journal of Geochemical Exploration, 88(1-3): 308-312.

Rad, S., Rivé, K., Allegre, C.J., 2011. Weathering regime associated with subsurface circulation on volcanic islands. Aquatic Geochemistry, 17(3): 221-241.

Raich, J.W., Potter, C.S., 1995. Global patterns of carbon dioxide emissions from soils. Global Biogeochemical Cycles, 9(1): 23-36.

Raymond, P.A., Hamilton, S.K., 2018. Anthropogenic influences on riverine fluxes of dissolved inorganic carbon to the oceans. Limnology and Oceanography Letters, 3(3): 143-155.

Reddy, M.M., Plummer, L.N., Busenberg, E., 1981. Crystal growth of calcite from calcium bicarbonate solutions at constant PCO2 and 25 C: a test of a calcite dissolution model. Geochimica et Cosmochimica Acta, 45(8): 1281-1289.

Rive, K., Gaillardet, J., Agrinier, P., Rad, S., 2013. Carbon isotopes in the rivers from the Lesser Antilles: origin of the carbonic acid consumed by weathering reactions in the Lesser Antilles. Earth Surface Processes and Landforms, 38(9): 1020-1035.

Roelandt, C., Goddéris, Y., Bonnet, M.P., Sondag, F., 2010. Coupled modeling of biospheric and chemical weathering processes at the continental scale. Global Biogeochemical Cycles, 24(2): 1-18.

References

Roland, M., Serrano-Ortiz, P., Kowalski, A.S., Goddéris, Y., Sánchez-Cañete, E., Ciais, P., Domingo, F., Cuezva, S., Sanchez-Moral, S., Longdoz, B., 2013. Atmospheric turbulence triggers pronounced diel pattern in karst carbonate geochemistry. Biogeosciences, 10(7): 5009-5017.

Romero-Mujalli, G., Hartmann, J., Börker, J., Gaillardet, J., Calmels, D., 2018. Ecosystem controlled soil-rock pCO2 and carbonate weathering–Constraints by temperature and soil water content. Chemical Geology.

Ruiz-Agudo, E., Putnis, C., Jiménez-López, C., Rodriguez-Navarro, C., 2009. An atomic force microscopy study of calcite dissolution in saline solutions: The role of magnesium ions. Geochimica et Cosmochimica Acta, 73(11): 3201-3217.

Rupp, G.L., Adams, V.D., 1981. Calcium carbonate precipitation as influenced by stream primary production. Water Quality Series(1-51).

Rye, R., Back, W., Hanshaw, B., Rightmire, C., Pearson Jr, F., 1981. The origin and isotopic composition of dissolved sulfide in groundwater from carbonate aquifers in Florida and Texas. Geochimica et Cosmochimica Acta, 45(10): 1941-1950.

Rye, R.O., 2005. A review of the stable-isotope geochemistry of sulfate minerals in selected igneous environments and related hydrothermal systems. Chemical Geology, 215(1-4): 5-36.

Schopka, H.H., Derry, L.A., 2012. Chemical weathering fluxes from volcanic islands and the importance of groundwater: The Hawaiian example. Earth and Planetary Science Letters, 339: 67-78.

Schott, J., Oelkers, E.H., Bénézeth, P., Goddéris, Y., François, L., 2012. Can accurate kinetic laws be created to describe chemical weathering? Comptes Rendus Geoscience, 344(11-12): 568-585.

Schwendenmann, L., Veldkamp, E., 2006. Long-term CO2 production from deeply weathered soils of a tropical rain forest: evidence for a potential positive feedback to climate warming. Global Change Biology, 12(10): 1878-1893.

Séby, F., Potin-Gautier, M., Giffaut, E., Borge, G., Donard, O., 2001. A critical review of thermodynamic data for selenium species at 25 C. Chemical Geology, 171(3-4): 173-194.

Semhi, K., Suchet, P.A., Clauer, N., Probst, J.-L., 2000. Impact of nitrogen fertilizers on the natural weathering-erosion processes and fluvial transport in the Garonne basin. Applied Geochemistry, 15(6): 865-878.

Seneviratne, S.I., Corti, T., Davin, E.L., Hirschi, M., Jaeger, E.B., Lehner, I., Orlowsky, B., Teuling, A.J., 2010. Investigating soil moisture–climate interactions in a changing climate: A review. Earth-Science Reviews, 99(3): 125-161.

Serrano-Ortiz, P., Roland, M., Sanchez-Moral, S., Janssens, I.A., Domingo, F., Goddéris, Y., Kowalski, A.S., 2010. Hidden, abiotic CO2 flows and gaseous reservoirs in the terrestrial carbon cycle: Review and perspectives. Agricultural and Forest Meteorology, 150(3): 321-329.

Shamberger, R.J., 1981. Selenium in the environment. Science of the total environment, 17(1): 59-74.

Smith, D.J., Jenkin, G., Naden, J., Boyce, A., Petterson, M., Toba, T., Darling, W., Taylor, H., Millar, I., 2010. Anomalous alkaline sulphate fluids produced in a magmatic hydrothermal system—Savo, Solomon Islands. Chemical Geology, 275(1-2): 35-49.

Smith, H., Wood, P.J., 2002. Flow permanence and macroinvertebrate community variability in limestone spring systems. Hydrobiologia, 487(1): 45-58.

Spence, J., Telmer, K., 2005. The role of sulfur in chemical weathering and atmospheric CO2 fluxes: evidence from major ions, δ13CDIC, and δ34SSO4 in rivers of the Canadian Cordillera. Geochimica et Cosmochimica Acta, 69(23): 5441-5458.

Steefel, C.I., Lasaga, A.C., 1994. A coupled model for transport of multiple chemical species and kinetic precipitation/dissolution reactions with application to reactive flow in single phase hydrothermal systems. American Journal of science, 294(5): 529-592.

Stüeken, E., Anderson, R., Bowman, J., Brazelton, W., Colangelo-Lillis, J., Goldman, A., Som, S., Baross, J., 2013. Did life originate from a global chemical reactor? Geobiology, 11(2): 101-126.

Suarez, D., 1983. Calcite supersaturation and precipitation kinetics in the Lower Colorado River, All-American Canal and East Highline Canal. Water Resources Research, 19(3): 653-661.

Suseela, V., Conant, R.T., Wallenstein, M.D., Dukes, J.S., 2012. Effects of soil moisture on the temperature sensitivity of heterotrophic respiration vary seasonally in an old-field climate change experiment. Global Change Biology, 18(1): 336-348.

Suzuoki, T., 1964. A geochemical study of selenium in volcanic exhalation and sulfur deposits. Bulletin of the Chemical Society of Japan, 37(8): 1200-1206.

Szramek, K., Walter, L.M., 2004. Impact of Carbonate Precipitation on Riverine Inorganic Carbon Mass Transport from a Mid-continent, Forested Watershed. Aquatic Geochemistry, 10(1): 99-137.

Szramek, K., Walter, L.M., Kanduč, T., Ogrinc, N., 2011. Dolomite Versus Calcite Weathering in Hydrogeochemically Diverse Watersheds Established on Bedded Carbonates (Sava and Soča Rivers, Slovenia). Aquatic Geochemistry, 17(4): 357-396.

Terada, A., Hashimoto, T., Kagiyama, T., 2012. A water flow model of the active crater lake at Aso volcano, Japan: fluctuations of magmatic gas and groundwater fluxes from the underlying hydrothermal system. Bulletin of volcanology, 74(3): 641-655.

Terada, A., Hashimoto, T., Kagiyama, T., Sasaki, H., 2008. Precise remote-monitoring technique of water volume and temperature of a crater lake in Aso volcano, Japan: implications for a sensitive window of a volcanic hydrothermal system. Earth, planets and space, 60(6): 705-710.

Terada, A., Sudo, Y., 2012. Thermal activity within the western-slope geothermal zone of Aso volcano, Japan: Development of a new thermal area. Geothermics, 42: 56-64.

Thorley, R.M.S., Taylor, L.L., Banwart, S.A., Leake, J.R., Beerling, D.J., 2015. The role of forest trees and their mycorrhizal fungi in carbonate rock weathering and its significance for global carbon cycling. Plant, Cell & Environment, 38(9): 1947-1961.

Thrailkill, J., Robl, T.L., 1981. Carbonate geochemistry of vadose water recharging limestone aquifers. Journal of Hydrology, 54(1-3): 195-208.

Torres, M.A., Moosdorf, N., Hartmann, J., Adkins, J.F., West, A.J., 2017. Glacial weathering, sulfide oxidation, and global carbon cycle feedbacks. Proceedings of the National Academy of Sciences, 114(33): 8716-8721.

Torres, M.A., West, A.J., Li, G., 2014. Sulphide oxidation and carbonate dissolution as a source of CO2 over geological timescales. Nature, 507: 346.

Tostevin, R., Turchyn, A.V., Farquhar, J., Johnston, D.T., Eldridge, D.L., Bishop, J.K., McIlvin, M., 2014. Multiple sulfur isotope constraints on the modern sulfur cycle. Earth and planetary science letters, 396: 14-21.

Tsuji, T., Ishibashi, J.i., Ishitsuka, K., Kamata, R., 2017. Horizontal sliding of kilometre-scale hot spring area during the 2016 Kumamoto Earthquake. Scientific reports, 7: 42947.

Ugolini, F.C., Dahlgren, R.A., 2002. Soil development in volcanic ash. GLOBAL ENVIRONMENTAL RESEARCH-ENGLISH EDITION-, 6(2): 69-82.

Urich, P.B., 2002. Land use in karst terrain: review of impacts of primary activities on temperate karst ecosystems. Department of Conservation Wellington, 60 pp.

van Geldern, R., Schulte, P., Mader, M., Baier, A., Barth, J.A., 2015. Spatial and temporal variations of pCO2, dissolved inorganic carbon and stable isotopes along a temperate karstic watercourse. Hydrological Processes, 29(15): 3423-3440.

Von Blanckenburg, F., Bouchez, J., Ibarra, D.E., Maher, K., 2015. Stable runoff and weathering fluxes into the oceans over Quaternary climate cycles. Nature Geoscience, 8(7): 538-542.

Wagner, W., Dorigo, W., de Jeu, R., Fernandez, D., Benveniste, J., Hass, E., Ertl, M., 2012. Fusion of active and passive microwave observations to create an essential climate variable data record on soil moisture. ISPRS Annals of the Photogrammetry, Remote Sensing and Spatial Information Sciences (ISPRS Annals), 7: 315-321.

Walker, J.C., Hays, P., Kasting, J.F., 1981. A negative feedback mechanism for the long-term stabilization of Earth's surface temperature. Journal of Geophysical Research: Oceans, 86(C10): 9776-9782.

Wang, S., Yeager, K.M., Wan, G., Liu, C.-Q., Liu, F., Lü, Y., 2015. Dynamics of CO2 in a karst catchment in the southwestern plateau, China. Environmental Earth Sciences, 73(5): 2415-2427.

Watanabe, K., 1978. Studies on the Aso pyroclastic flow deposits in the region to the west of Aso caldera, southwest Japan. I: geology. Mem. Fac. Educ. Kumamoto Univ., Natural. Sci.(27): 97-120.

Wen, H., Carignan, J., 2007. Reviews on atmospheric selenium: emissions, speciation and fate. Atmospheric environment, 41(34): 7151-7165.

West, A.J., Galy, A., Bickle, M., 2005. Tectonic and climatic controls on silicate weathering. Earth and Planetary Science Letters, 235(1-2): 211-228.

White, A.F., Blum, A.E., 1995. Effects of climate on chemical weathering in watersheds. Geochimica et Cosmochimica Acta, 59(9): 1729-1747.

White, A.F., Blum, A.E., Schulz, M.S., Vivit, D.V., Stonestrom, D.A., Larsen, M., Murphy, S.F., Eberl, D., 1998. Chemical weathering in a tropical watershed, Luquillo Mountains, Puerto Rico: I. Long-term versus short-term weathering fluxes. Geochimica et Cosmochimica Acta, 62(2): 209-226.

White, A.F., Brantley, S.L., 2003. The effect of time on the weathering of silicate minerals: why do weathering rates differ in the laboratory and field? Chemical Geology, 202(3-4): 479-506.

Winkel, L., Vriens, B., Jones, G., Schneider, L., Pilon-Smits, E., Bañuelos, G., 2015. Selenium cycling across soil-plant-atmosphere interfaces: a critical review. Nutrients, 7(6): 4199-4239.

Yamada, M., Ohsawa, S., Kazahaya, K., Yasuhara, M., Takahashi, H., Amita, K., Mawatari, H., Yoshikawa, S., 2011. Mixing of magmatic CO2 into volcano groundwater flow at Aso volcano assessed combining carbon and water stable isotopes. Journal of Geochemical Exploration, 108(1): 81-87.

Yamamoto, M., 1976. Relationship between Se/S and sulfur isotope ratios of hydrothermal sulfide minerals. Mineralium Deposita, 11(2): 197-209.

Yoshimura, K., Liu, Z., Cao, J., Yuan, D., Inokura, Y., Noto, M., 2004. Deep source CO2 in natural waters and its role in extensive tufa deposition in the Huanglong Ravines, Sichuan, China. Chemical Geology, 205(1): 141-153.

Yoshimura, K., Nakao, S., Noto, M., Inokura, Y., Urata, K., Chen, M., Lin, P.W., 2001. Geochemical and stable isotope studies on natural water in the Taroko Gorge karst area, Taiwan—chemical weathering of carbonate rocks by deep source CO2 and sulfuric acid. Chemical Geology, 177(3): 415-430.

Zaihua, L., Daoxian, Y., Shiyi, H., 1997. Stable Carbon Isotope Geochemical and Hydrochemical Features in the System of Carbonate–H2O–CO2 and Their Implications—Evidence from Several Typical Karst Areas of China. Acta Geologica Sinica - English Edition, 71(4): 446-454.

Zaihua, L., Svensson, U., Dreybrodt, W., Daoxian, Y., Buhmann, D., 1995. Hydrodynamic control of inorganic calcite precipitation in Huanglong Ravine, China: Field measurements and theoretical prediction of deposition rates. Geochimica et Cosmochimica Acta, 59(15): 3087-3097.

Zhang, J., Wang, H., Liu, Z., An, D., Dreybrodt, W., 2012. Spatial–temporal variations of travertine deposition rates and their controlling factors in Huanglong Ravine, China–A world's heritage site. Applied geochemistry, 27(1): 211-222.

Zhao, M., Liu, Z., Li, H.-C., Zeng, C., Yang, R., Chen, B., Yan, H., 2015. Response of dissolved inorganic carbon (DIC) and δ13CDIC to changes in climate and land cover in SW China karst catchments. Geochimica et Cosmochimica Acta, 165: 123-136.

Zhong, J., Li, S.-l., Tao, F., Yue, F., Liu, C.-Q., 2017. Sensitivity of chemical weathering and dissolved carbon dynamics to hydrological conditions in a typical karst river. Scientific reports, 7: 42944.

Žutić, V., Stumm, W., 1984. Effect of organic acids and fluoride on the dissolution kinetics of hydrous alumina. A model study using the rotating disc electrode. Geochimica et Cosmochimica Acta, 48(7): 1493-1503.

Zuyi, T., Taiwei, C., Jinzhou, D., XiongXin, D., Yingjie, G., 2000. Effect of fulvic acids on sorption of U (VI), Zn, Yb, I and Se (IV) onto oxides of aluminum, iron and silicon. Applied Geochemistry, 15(2): 133-139.

Appendix

Appendix A. Temperature and soil water content ranges.

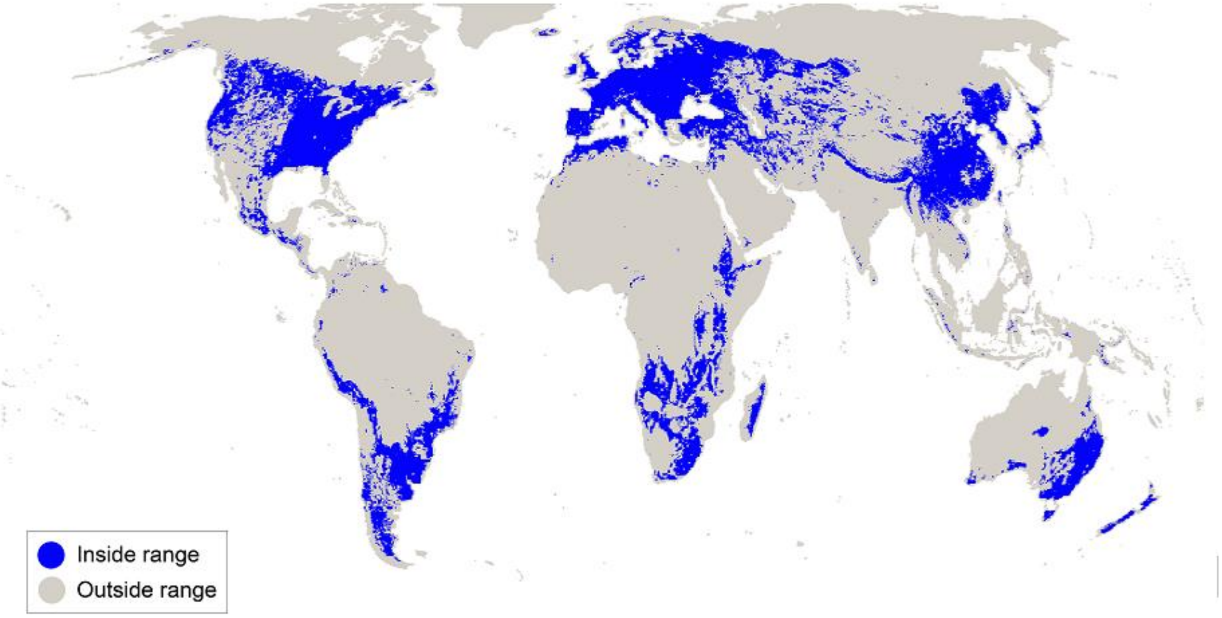

Figure A.1. Distribution of areas within the range of land temperature (0.4 to 22.0°C) and soil water content (0.17 to 0.37m^{-3} m^{-3}) of the 164 selected spring samples. Blue indicates the regions with the same range and in grey are the regions with different land temperature or soil water content.

Appendix B. Equilibrium model

The concentration of chemical species at equilibrium with calcite dissolution was calculated considering open conditions for the system $CaCO_3$-H_2O-CO_2 and a given calcite saturation index (SIc = 0 or SIc = 0.5, when applicable), represented by the following chemical reactions:

$$2H_2O_{(l)} \leftrightarrow H_3O^+_{(aq)} + OH^-_{(aq)} \tag{B.1}$$

$$CO_{2(g)} \leftrightarrow CO_{2(aq)} \tag{B.2}$$

$$CO_{2(aq)} + \ 2H_2O_{(l)} \leftrightarrow HCO^-_{3(aq)} + H_3O^+_{(aq)} \tag{B.3}$$

$$HCO^-_{3(aq)} + \ H_2O_{(l)} \leftrightarrow CO^{2-}_{3(aq)} + H_3O^+_{(aq)} \tag{B.4}$$

$$CaCO_{3(s)} \leftrightarrow Ca^{2+}_{(aq)} + CO^{2-}_{3(aq)} \tag{B.5}$$

with equilibrium constants K_w, K_{pCO2}, K_1, K_{a2} and K_{sp}, expressed as:

$$K_w = \ (H_3O^+)\ (OH^-) \tag{B.6}$$

$$K_{pCO_2} = \frac{(CO_{2(aq)})}{fCO_2} \tag{B.7}$$

$$K_1 = \frac{(HCO_3^-)(H_3O^+)}{(CO_{2(aq)})} \tag{B.8}$$

$$K_{a2} = \frac{(CO_3^{2-})(H_3O^+)}{(HCO_3^-)} \tag{B.9}$$

$$K_{sp} = (Ca^{2+})\ (CO_3^{2-}) \tag{B.10}$$

where parenthesis indicates activity of chemical species and "*f*" fugacity of gases. In this work we assumed that fugacity is equal to partial pressure. Alkalinity was assumed to be $[HCO_3^-] + 2[CO_3^{2-}] + [OH^-] - [H^+]$. The equilibrium equations were solved using the charge balance equation and the Newton-Raphson method for the numerical approach. The standard equilibrium constants (*K*) at 25°C for each chemical equation (from Eq. B.1 to B.5) are reported in Table B.1, the temperature dependency of the equilibrium constants (*K*) and the Henry's constant (K_{pCO2}) was calculated using the Van't Hoff equation (Eq. B.11), given by:

$$ln\left(\frac{K_2}{K_1}\right) = -\frac{\Delta H°}{R}\left(\frac{1}{T_2} - \frac{1}{T_1}\right) \tag{B.11}$$

where T represents the absolute temperature in Kelvin, ΔH° is the standard enthalpy of reaction and *R* is the gas constant. Furthermore, the activity coefficient of each chemical species *i* (γ_i) was calculated using the Davies Equation (Eq. B.12):

$$log\gamma_i = -Az_i{}^2\left(\frac{\sqrt{I}}{1+\sqrt{I}} - 0.3I\right) \tag{B.12}$$

where *A* is a temperature related constant, z_i is the charge of the chemical species and *I* is the ionic strength of the solution.

Furthermore, closed system conditions were calculated using a simplified equation based on the following summarized chemical equation for calcite dissolution:

$$CaCO_{3(s)} + CO_{2(aq)} + H_2O_{(l)} \leftrightarrow Ca^{2+}_{(aq)} + 2HCO^{-}_{3(aq)} \tag{B.13}$$

The total concentration of calcium ions, $[Ca^{2+}]_t$ was assumed to be equal to half of the concentration of carbonate acid, $[HCO_3^-]$. In order to account for closed system conditions, the initial *p*CO₂ (*p*CO₂ᵢ) should be equal to $[Ca^{2+}]_t + [CO_{2(aq)}]$, and $[Ca^{2+}]_t$ is determined by solving the following equation:

$$[Ca^{2+}]_t^3 + \frac{K_{sp}K_1}{4K_{a2}\gamma_1^2\gamma_2}[Ca^{2+}]_t - \frac{K_{sp}K_1K_{pCO_2}}{4K_{a2}\gamma_1^2\gamma_2}pCO_{2i} = 0 \tag{B.14}$$

where γ_z stands for the activity coefficient for ions of charge "*z*" (Eq. B.12), and K_{sp}, K_1, K_{a2}, K_{pCO2} are the equilibrium constants for equations B.5, B.3, B.4, and B.2, respectively (see table B.1).

Table B.1. Solubility product constants at 25°C (K) and standard enthalpy (*ΔH°*) for the reactions considered in this work (Romero-Mujalli et al., 2018).

Reaction number	Constant (*K*)	$\Delta H_r°$ (KJ/mol)
B.1	10^{-14}	55.9066
B.2	$10^{-1.468(a)}$	-19.983
B.3	$10^{-6.352}$	9.109
B.4	$10^{-10.329}$	14.90
B.5	$10^{-8.48}$	-9.61

Thermodynamic data was taken from phreeqc.dat database after (Parkhurst and Appelo, 1999).
(a): Henry's constant for dissolution of gas CO_2 in water.

Appendix C. Schematic of global calcite weathering model

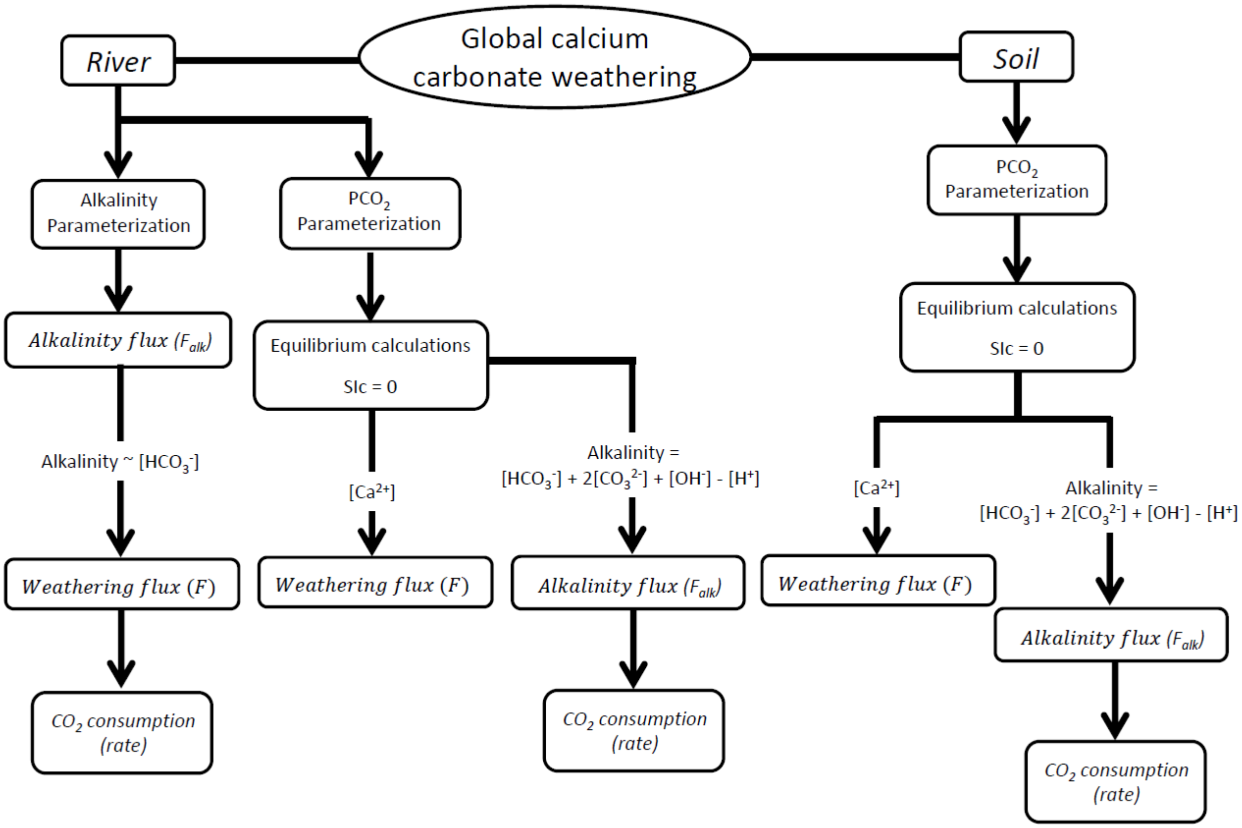

Fig. C.1. Schematic of how calcium carbonate dissolution was modelled using different constraints. The assumption alkalinity is approximately [HCO$_3^-$] was applied for the alkalinity parameterization only to calculate global alkalinity fluxes, equivalent to the weathering flux (*F*). The equilibrium approaches were used to calculate concentrations of Ca^{2+} and alkalinity due to dissolution of calcite. For this scenario, alkalinity is represented as [HCO$_3^-$] + 2[CO$_3^{2-}$] + [OH$^-$] - [H$^+$]. Alkalinity weathering fluxes (*F*) and resulting CO$_2$ rates are discussed in the main text.

Appendix D. Results of chemical analysis of natural waters in Aso caldera

Table A.1. Sample localizations and in situ measurements. Total alkalinity (TA) measured by titration method.

N°	Campaign	Date (dd.mm.yyyy)	Time (hh:mm)	Type	Lat (°)	Lon (°)	Alt. (m.a.s.l.)	Temp. (°C ± 0.1)	pH (± 0.01)	Cond. (µS cm^{-1} ± 1)	DO (µM ± 5)	TA (µM ± 10)
S01	1	27.03.2014	11:30	mrn	32.90935	130.9846	463	16.3	6.23	429	n.m.	698
S02	1	27.03.2014	12:30	d	32.90936	130.983	464	19.3	6.32	534	n.m.	913
S03	1	27.03.2014		cc	32.89722	131.1027	938	15.1	2.52	519	n.m.	n.m.
S04	1	27.03.2014	17:00	t	32.96746	131.107	494	21.5	6.60	343	n.m.	954
S05	1	28.03.2014	11:00	t	32.82453	131.0489	407	16.6	7.12	343	215	757
S06	1	28.03.2014	11:30	mrs	32.8223	131.0495	406	17.0	7.18	223	203	1016
S07	1	28.03.2014	12:50	cs	32.82512	131.0951	485	15.0	7.09	235	231	879
S08	1	01.04.2014	11:30	t	32.82777	131.0894	501	10.6	5.31	852	291	92
S09	1	01.04.2014	12:00	t	32.82013	131.0859	462	15.9	5.87	249	254	853
S10	1	01.04.2014	12:30	mrs	32.81911	131.0861	460	16.8	6.24	241	201	906
S11	1	01.04.2014	13:00	t	32.81462	131.0838	461	17.1	6.84	160	191	1094
S12	1	01.04.2014	14:30	t	32.82066	131.0635	429	18.1	6.45	337	209	657
S13	1	01.04.2014	15:00	d	32.81953	131.0638	426	17.7	6.69	286	210	883
S14	1	01.04.2014		mrs	32.81674	131.0678	431	17.9	6.86	216	271	1018
S15	1	01.04.2014	16:30	t	32.82373	131.0322	408	15.6	7.12	137	218	762
S16	1	02.04.2014	10:40	cs	32.81393	131.1218	408	15.6	7.68	151	221	1284
S17	1	02.04.2014	11:20	t	32.80792	131.111	534	16.2	7.70	145	245	1297
S18	1	02.04.2014	12:30	t	32.80308	131.0203	503	12.3	8.05	44	251	309
S19	1	02.04.2014	14:00	cs	32.82995	131.0521	423	15.1	7.07	192	273	642
S20	1	02.04.2014	14:30	t	32.83241	131.0529	435	17.8	7.54	193	263	875
S21	1	02.04.2014	15:30	hs	32.86075	131.0361	712	43.0	2.96	815	28	n.m.
S22	1	02.04.2014	16:30	t	32.85201	131.0059	337	18.3	5.39	187	239	585
S23	1	02.04.2014	17:00	mrs	32.84843	131.007	333	17.7	5.69	201	196	1012
S24	1	03.04.2014	10:20	t	32.96167	131.1515	537	16.1	7.14	138	264	985
S25	1	03.04.2014	11:00	mrn	32.97026	131.1307	495	17.9	7.21	278	205	1788
S26	1	03.04.2014	11:20	t	32.97094	131.1317	494	16.0	7.39	185	195	1269
S27	1	03.04.2014	13:00	t	32.95171	131.1058	506	18.5	8.23	333	286	1488
S28	1	03.04.2014	13:30	t	32.94094	131.085	514	18.0	7.61	773	220	1250
S29	1	03.04.2014	14:00	t	32.971	131.0576	478	16.5	7.51	760	208	1301
S30	1	03.04.2014	15:30	mrn	32.97149	131.0578	480	15.0	7.55	231	220	1255
S31	1	03.04.2014	16:30	t	32.99326	131.0481	496	12.6	7.56	72	267	548
S32	1	03.04.2014	17:00	t	32.97377	131.0326	480	13.9	7.39	99	212	632
S33	1	04.04.2014	12:53	mr	32.87384	130.9597	197	13.9	6.98	280	272	1083
S34	1	04.04.2014	14:00	t	32.95227	131.0262	475	16.0	7.56	454	257	840
S35	1	04.04.2014	14:23	mrn	32.95455	131.0258	471	13.8	7.51	432	285	1097
S36	1	04.04.2014	15:10	mrn	32.96986	131.1072	494	13.7	7.68	238	270	1268
S01	2	01.10.2014	17:17	mrn	32.90935	130.9846	463	17.8	7.42	338	273	956
S02	2	01.10.2014	17:50	t	32.90933	130.983	464	18.6	7.58	627	262	1038
S03	2	02.10.2014	16:20	cc	32.89722	131.1027	938	19.5	4.17	419	264	1029
S03	2	02.10.2014	16:50	cc	32.89594	131.102	968	19.5	4.14	383	261	n.m.

N°	Campaign	Date (dd.mm.yyyy)	Time (hh:mm)	Type	Lat (°)	Lon (°)	Alt. (m.a.s.l.)	Temp. (°C ± 0.1)	pH (± 0.01)	Cond. (µS cm^{-1} ± 1)	DO (µM ± 5)	TA (µM ± 10)
S04	2	01.10.2014	14:06	t	32.96746	131.107	494	18.9	9.00	290	386	1149
S05	2	30.09.2014	16:55	t	32.82453	131.0489	407	17.3	7.34	327	288	743
S06	2	04.10.2014	12:45	mrs	32.8223	131.0495	406	19.1	8.08	233	284	993
S07	2	03.10.2014	12:35	cs	32.82512	131.0951	485	14.3	7.03	224	303	853
S08	2	03.10.2014	13:30	t	32.82777	131.0894	501	21.2	4.30	793	263	884
S09	2	30.09.2014	14:07	t	32.82013	131.0859	462	16.6	7.60	290	297	735
S10	2	30.09.2014	13:37	mrs	32.81911	131.0861	460	17.8	7.70	237	285	951
S11	2	30.09.2014	12:45	t	32.81462	131.0838	461	17.4	7.96	130	295	1075
S11	2	30.09.2014	13:07	t	32.81438	131.0839	459	17.1	7.61	128	291	n.m.
S12	2	30.09.2014	16:30	t	32.82066	131.0635	429	17.3	7.37	270	284	830
S13	2	30.09.2014	16:00	d	32.81953	131.0638	426	17.8	7.55	265	276	874
S14	2	04.10.2014	13:50	mrs	32.81674	131.0678	431	18.2	7.97	221	287	1044
S15	2	03.10.2014	16:10	t	32.82373	131.0322	408	19.0	7.98	179	285	1058
S15	2	03.10.2014	16:00	t	32.82305	131.0323	408	18.6	7.58	188	282	n.m.
S16	2	03.10.2014	11:52	cs	32.81393	131.1218	534	16.1	7.76	155	307	1293
S17	2	30.09.2014	12:00	t	32.80792	131.111	503	18.2	7.93	152	284	1246
S19	2	03.10.2014	14:55	cs	32.82995	131.0521	423	16.4	6.55	212	279	664
S20	2	30.09.2014	17:20	t	32.83241	131.0529	435	17.5	7.68	206	282	904
S21	2	06.10.2014	17:23	hs	32.86042	131.0358	712	35.1	4.43	287	n.m.	885
S21	2	06.10.2014	17:40	hs	32.86042	131.0358	712	39.3	3.04	735	n.m.	n.m.
S22	2	03.10.2014	17:20	t	32.85201	131.0059	337	21.5	7.85	185	265	632
S23	2	04.10.2014	11:55	mrs	32.84843	131.007	333	19.6	8.07	235	282	1162
S24	2	01.10.2014	11:15	t	32.96167	131.1515	537	17.2	7.78	124	290	1034
S25	2	01.10.2014	11:55	mrn	32.97026	131.1307	495	18.6	7.60	242	251	1633
S26	2	01.10.2014	12:30	t	32.97094	131.1317	494	17.9	7.45	165	255	1258
S27	2	02.10.2014	13:40	t	32.95171	131.1058	506	21.1	8.50	307	350	1527
S28	2	02.10.2014	14:30	t	32.94094	131.085	514	21.4	7.22	712	257	1197
S29	2	01.10.2014	14:40	t	32.971	131.0576	478	20.4	8.01	587	278	1335
S30	2	01.10.2014	15:42	mrn	32.97149	131.0578	480	18.0	7.86	216	291	1110
S31	2	02.10.2014	12:50	t	32.99326	131.0481	496	17.8	7.67	87	280	640
S32	2	02.10.2014	12:10	t	32.97377	131.0326	480	19.2	7.33	163	257	773
S33	2	04.10.2014	10:45	mr	32.87384	130.9597	197	18.8	8.04	280	286	1138
S34	2	01.10.2014	16:03	t	32.95227	131.0262	475	19.2	7.92	478	278	875
S35	2	01.10.2014	16:30	mrn	32.95455	131.0258	471	18.4	7.62	370	278	1029
S36	2	01.10.2014	13:17	mrn	32.96986	131.1072	494	17.8	7.83	172	290	1135
S37	2	04.10.2014	14:40	cs	32.82243	131.0732	449	17.0	6.31	338	249	519
S38	2	04.10.2014	15:20	cs	32.82367	131.0785	465	15.7	6.57	273	257	646
S39	2	04.10.2014	16:05	cs	32.83068	131.0447	410	16.9	6.43	226	242	888
S40	2	04.10.2014	16:35	cs	32.83333	131.0412	403	16.8	6.41	241	263	894
S41	2	04.10.2014	17:05	cs	32.84456	131.0378	421	16.5	6.81	265	276	903
S42	2	06.10.2014	13:55	hs	32.86009	131.0261	528	46.0	6.04	947	n.m.	4459
S43	2	06.10.2014	16:15	hs	32.85854	131.038	762	43.5	4.71	202	n.m.	4454
S44	2	07.10.2014	11:25	cs	32.99602	131.0636	738	15.3	7.53	71	298	561

Appendix

N°	Campaign	Date (dd.mm.yyyy)	Time (hh:mm)	Type	Lat (°)	Lon (°)	Alt. (m.a.s.l.)	Temp. (°C ± 0.1)	pH (± 0.01)	Cond. (µS cm^{-1} ± 1)	DO (µM ± 5)	TA (µM ± 10)
S45	2	07.10.2014	12:10	cs	32.98022	131.0808	490	17.4	6.88	116	365	814
S46	2	07.10.2014	12:40	cs	32.95202	131.0948	507	14.7	7.12	311	292	797
S47	2	07.10.2014	13:55	cs	32.93916	131.0403	494	15.7	6.98	127	295	596
S48	2	07.10.2014	15:20	cs	32.93196	130.9912	490	16.1	7.39	102	304	877
S49	2	07.10.2014	16:25	hs	32.86238	131.036	682	41.2	3.74	624	48	1607
S49	2	07.10.2014	16:30	hs	32.86238	131.036	682	49.2	5.85	543	79	2902
S01	3	13.05.2015	10:50	mrn	32.90935	130.9846	463	16.2	7.28	416	285	812
S01	3	16.05.2015	9:30	mrn	32.90935	130.9846	463	18.3	7.15	358	258	651
S02	3	13.05.2015	11:20	d	32.90936	130.983	464	17.1	7.64	103	312	687
S03	3	17.05.2015	12:20	cc	32.89722	131.1027	938	20.3	4.28	661	257	n.m.
S04	3	13.05.2015	16:25	t	32.96746	131.107	494	21.0	8.37	246	315	1192
S05	3	14.05.2015	12:00	t	32.82453	131.0489	407	18.1	7.26	307	296	833
S06	3	14.05.2015	12:25	mrs	32.8223	131.0495	406	18.8	7.85	258	281	872
S07	3	12.05.2015	12:45	cs	32.82512	131.0951	485	14.2	7.06	222	303	882
S08	3	14.05.2015	15:00	t	32.82777	131.0894	501	20.1	4.47	910	272	n.m.
S09	3	14.05.2015	15:20	t	32.82013	131.0859	462	18.6	6.98	353	284	728
S10	3	14.05.2015	16:05	mrs	32.81911	131.0861	460	21.5	7.62	262	276	1077
S11	3	14.05.2015	16:40	t	32.81462	131.0838	461	19.0	7.88	129	273	920
S12	3	14.05.2015	13:35	t	32.82066	131.0635	429	17.7	6.57	348	264	569
S13	3	14.05.2015	13:45	d	32.81953	131.0638	426	19.6	7.49	266	274	785
S14	3	14.05.2015	14:20	mrs	32.81839	131.0635	427	20.0	7.98	211	288	935
S15	3	14.05.2015	17:10	t	32.82305	131.0323	408	18.1	7.84	141	278	848
S16	3	18.05.2015	14:00	cs	32.81393	131.1218	534	15.6	7.96	146	304	1265
S17	3	18.05.2015	14:25	t	32.80792	131.111	503	16.8	8.02	140	283	1202
S18	3	18.05.2015	15:00	t	32.80299	131.0202	671	14.4	7.68	48	293	366
S19	3	16.05.2015	14:20	cs	32.82995	131.0521	423	16.1	6.90	200	278	622
S20	3	14.05.2015	11:45	t	32.83241	131.0529	435	16.0	7.68	201	287	865
S21	3	16.05.2015	12:10	hs	32.86042	131.0358	712	42.3	2.15	3050	63	n.m.
S22	3	14.05.2015	10:25	t	32.85201	131.0059	337	17.5	7.52	183	295	831
S23	3	14.05.2015	11:00	mrs	32.84843	131.007	333	18.3	7.98	227	288	1237
S23	3	16.05.2015	10:30	mrs	32.84843	131.007	333	18.5	7.73	156	283	747
S24	3	17.05.2015	11:45	t	32.96167	131.1515	537	18.3	8.00	126	298	1016
S25	3	13.05.2015	17:50	mrn	32.97026	131.1307	495	19.3	7.55	285	210	1549
S26	3	13.05.2015	18:10	t	32.97094	131.1317	494	18.6	7.58	173	285	1163
S27	3	17.05.2015	13:55	t	32.95171	131.1058	506	27.0	7.73	292	244	1304
S28	3	17.05.2015	15:00	t	32.94277	131.083	509	22.7	7.43	792	211	2243
S29	3	13.05.2015	15:00	t	32.971	131.0576	478	22.5	7.48	630	266	822
S30	3	13.05.2015	15:30	mrn	32.97149	131.0578	480	20.2	7.71	232	280	1112
S31	3	18.05.2015	11:30	t	32.99326	131.0481	496	15.5	7.75	80	289	629
S32	3	13.05.2015	14:20	t	32.97377	131.0326	480	22.2	7.35	165	256	837
S33	3	18.05.2015	10:25	mr	32.87384	130.9597	197	18.1	7.98	263	278	1121
S34	3	13.05.2015	13:15	t	32.95227	131.0262	475	19.0	7.40	437	303	955
S35	3	13.05.2015	13:00	mrn	32.95455	131.0258	471	17.9	7.44	416	288	966

Appendix

N°	Campaign	Date (dd.mm.yyyy)	Time (hh:mm)	Type	Lat (°)	Lon (°)	Alt. (m.a.s.l.)	Temp. (°C ± 0.1)	pH (± 0.01)	Cond. (µS cm^{-1} ± 1)	DO (µM ± 5)	TA (µM ± 10)
S36	3	13.05.2015	17:15	mrn	32.96986	131.1072	494	16.2	7.60	156	283	1066
S37	3	12.05.2015	14:30	cs	32.82243	131.0732	449	14.7	6.30	324	250	542
S38	3	12.05.2015	13:30	cs	32.82367	131.0785	465	15.2	6.57	272	258	694
S39	3	12.05.2015	15:00	cs	32.83068	131.0447	410	15.7	6.48	226	252	876
S40	3	12.05.2015	15:20	cs	32.83333	131.0412	403	16.1	6.49	229	241	902
S41	3	12.05.2015	16:00	cs	32.84456	131.0378	421	16.0	6.87	268	280	918
S42	3	16.05.2015	13:45	hs	32.86009	131.0261	528	46.0	6.12	955	38	6717
S43	3	16.05.2015	12:45	hs	32.85854	131.038	762	66.2	2.42	1683	ND	n.m.
S44	3	18.05.2015	12:10	cs	32.99602	131.0636	738	13.9	7.63	66	296	564
S45	3	17.05.2015	11:05	cs	32.98022	131.0808	490	17.6	7.20	113	408	844
S46	3	17.05.2015	14:15	cs	32.95202	131.0948	507	15.6	7.20	310	282	821
S47	3	17.05.2015	10:20	cs	32.93916	131.0403	494	15.1	7.07	131	307	529
S48	3	13.05.2015	11:55	cs	32.93196	130.9912	490	14.7	7.11	100	313	892
S49	3	16.05.2015	11:30	hs	32.86238	131.036	682	41.0	3.44	591	46	n.m.
S49	3	16.05.2015	11:45	hs	32.86238	131.036	682	45.9	5.76	523	64	n.m.
S01	4	08.07.2015		mrn	32.90944	130.9843	463	23.3	7.60	264	n.m.	870
S01	4	15.07.2015		mrn				n.m.	n.m.	n.m.	n.m.	n.m.
S01	4	15.07.2015		mrn				n.m.	n.m.	n.m.	n.m.	n.m.
S03	4	15.07.2015		cc	32.89722	131.1027	938	23.3	5.15	280	n.m.	ND
S04	4	08.07.2015		t	32.96852	131.1068	494	21.6	7.92	263	n.m.	434
S07	4	15.07.2015		cs	32.82512	131.0951	485	16.5	6.95	241	n.m.	244
S19	4	15.07.2015		cs	32.82995	131.0521	423	17.2	6.54	222	n.m.	678
S22	4	29.06.2015		t	32.85201	131.0059	337	22.4	8.73	188	n.m.	666
S23	4	29.06.2015		mrs	32.84843	131.007	333	20.7	8.87	237	n.m.	326
S27	4	08.07.2015		t	32.95171	131.1058	506	27.3	8.39	282	n.m.	n.m.
S28	4	15.07.2015		t	32.94943	131.085	509	30.3	6.28	582	n.m.	600
S29	4	04.07.2015		t	32.971	131.0576	478	19.7	8.42	503	n.m.	1276
S30	4	04.07.2015		mrn	32.97149	131.0578	480	17.6	8.53	200	n.m.	1241
S33	4	29.06.2015		mr	32.87384	130.9597	197	21.3	8.54	249	n.m.	394
S34	4	08.07.2015		t	32.9512	131.0274	475	24.1	7.66	295	n.m.	655
S35	4	08.07.2015		mrn	32.9525	131.0264	471	21.7	7.72	213	n.m.	982
S36	4	08.07.2015		mrn	32.97029	131.1071	494	20.9	7.96	172	n.m.	1167
S46	4	08.07.2015		cs	32.95202	131.0948	507	16.3	8.32	315	n.m.	268
S03	5	20.09.2015	11:50	cc	32.89722	131.1027	938	18.3	4.08	610	250	n.m.
S18	5	19.09.2015	11:50	t	32.80308	131.0203	503	13.6	7.44	62	278	361
S50	5	20.09.2015	15:00	hs	32.87424	131.0311	751	33.6	7.55	533	n.m.	4900
S51	5	20.09.2015	15:30	hs	32.87322	131.0319		24.4	7.51	405	n.m.	ND
S01	6	03.07.2016	12:14	mrn	32.90894	130.9843		21.6	7.16	335	240	836
S07	6	04.07.2016	13:30	cs	32.82533	131.095		16.7	7.01	228	296	910
S23	6	04.07.2016	12:30	mrs	32.84857	131.007		24.1	7.83	192	268	1003
S28	6	03.07.2016	18:00	t	32.94198	131.084		23.0	7.00	403	238	738
S37	6	04.07.2016	15:30	cs	32.82238	131.0731		17.2	6.45	281	246	576
S46	6	03.07.2016	15:50	cs	32.95193	131.0948		15.4	7.09	311	279	831

Appendix

N°	Campaign	Date (dd.mm.yyyy)	Time (hh:mm)	Type	Lat (°)	Lon (°)	Alt. (m.a.s.l.)	Temp. (°C ± 0.1)	pH (± 0.01)	Cond. (µS cm^{-1} ± 1)	DO (µM ± 5)	TA (µM ± 10)
S52	6	03.07.2016	14:33	hs	32.95965	131.036		24.4	6.68	2130	38	759
S53	6	03.07.2016	18:28	t	32.93904	131.0855		24.4	6.19	120	234	64
S54	6	03.07.2016	18:30	t	32.93913	131.0852		23.0	6.91	304	215	886
S55	6	04.07.2016	11:40	hs	32.97772	131.0428		42.9	7.13	1073	30	2988
S07	7	06.10.2016	10:30	cs	32.82512	131.0951	485	14.5	6.92	225	302	889
S08	7	06.10.2016	11:00	t	32.82777	131.0894	501	20.9	3.99	762	266	n.m.
S16	7	06.10.2016	9:30	cs	32.81393	131.1218	534	16.2	7.78	166	310	1287
S19	7	06.10.2016	12:50	cs	32.82995	131.0521	423	15.2	6.46	193	294	611
S37	7	06.10.2016	11:50	cs	32.82243	131.0732	449	14.8	6.24	293	246	565
S38	7	06.10.2016	11:30	cs	32.82367	131.0785	465	15.4	6.36	259	241	791
S39	7	06.10.2016	13:55	cs	32.83068	131.0447	410	16.3	6.36	215	258	975
S40	7	06.10.2016	14:20	cs	32.83333	131.0412	403	16.7	6.39	225	272	954
S44	7	07.10.2016	14:45	cs	32.99602	131.0636	738	15.4	7.08	69	289	586
S45	7	07.10.2016	14:00	cs	32.98022	131.0808	490	17.5	6.82	116	420	828
S46	7	07.10.2016	10:40	cs	32.95202	131.0948	507	14.2	7.11	303	297	804
S47	7	07.10.2016	10:15	cs	32.93916	131.0403	494	14.7	6.97	122	291	631
S48	7	07.10.2016	8:55	cs	32.93196	130.9912	490	14.7	6.68	103	270	905
S50	7	08.10.2016	11:50	hs	32.87424	131.0311	751	39.8	6.49	635	148	5801
S50	7	08.10.2016	12:10	hs	32.87424	131.0311	750	45.5	7.18	285	112	n.m.
S51	7	08.10.2016	12:30	d	32.87322	131.0319	750	25.7	7.63	416	226	803
S52	7	09.10.2016	16:50	hs	32.95965	131.036		23.5	6.70	2150	87	722
S55	7	09.10.2016	16:10	hs	32.97772	131.0428		40.8	7.20	1049	42	2738
S56	7	06.10.2016	12:20	cs	32.82327	131.0701	449	16.2	5.98	352	256	510
S57	7	07.10.2016	10:50	cs	32.94715	131.0929	527	15.7	6.78	454	258	846
S58	7	07.10.2016	12:55	cs	32.94762	131.1166	524	15.9	6.96	296	270	1192
S59	7	07.10.2016	13:25	cs	32.95074	131.1169	516	15.7	6.87	293	263	1224
S60	7	09.10.2016	12:50	hs	32.84597	131.0053	338	26.5	7.02	474	60	3976
S61	7	09.10.2016	13:40	hs	32.87144	131.0059	435	43.4	7.33	1104	62	7330
S62	7	09.10.2016	14:40	hs	32.93373	131.0412	525	52.6	6.86	3770	68	5587
S63	7	09.10.2016	15:30	hs	32.92862	131.1097	563	19.8	7.20	676	165	1878
R1A	7	09.10.2016	8:30	r	32.81664	130.7287	27	19.5	5.74	3	276	n.m.
R1B	6	03.07.2016		r	32.95561	131.0368		n.m.	n.m.	n.m.	n.m.	n.m.
R2A	6	03.07.2016		r	32.93904	131.0855		n.m.	n.m.	n.m.	n.m.	n.m.
R2B	6	03.07.2016		r	32.93904	131.0855		n.m.	n.m.	n.m.	n.m.	n.m.
R2C	6	03.07.2016		r	32.93904	131.0855		n.m.	n.m.	n.m.	n.m.	n.m.

n.m. Not measured.

Water type: cold spring (cs), hot spring (hs), tributary (t), drainage (d), main river outlet (mr), main river north (mrn), main river south (mrs), center-cone drainage (cc) and rain (r).

Table A.2. Results of ionic chromatography, dissolved inorganic carbon (DIC) and dissolved silica (DSi) in natural waters.

N°	**DIC (µM ± 10)**	**DSi (mM ± 0.05)**	**F^- (µM ± 5)**	**Cl^- (µM ± 10)**	**Br^- (µM ± 0.1)**	**NO_3^- (µM ± 1)**	**PO_4^{3-} (µM ± 0.1)**	**SO_4^{2-} (µM ± 10)**	**Na^+ (µM ± 10)**	**K^+ (µM ± 5)**	**Ca^{2+} (µM ± 10)**	**Mg^{2+} (µM ± 10)**	**NH_4^+ (µM ± 0.01)**
S01	861	0.86	46	480	ND	63	ND	1052	720	144	667	507	n.m.
S02	970	0.84	13	685	ND	30	ND	1328	1571	186	509	633	n.m.
S03	134	0.46	394	1588	1.6	19	ND	905	333	68	403	265	n.m.
S04	561	0.97	41	399	ND	27	2.1	631	546	119	590	360	n.m.
S05	773	1.41	38	312	ND	75	5.1	949	711	136	676	372	n.m.
S06	993	1.20	22	201	ND	80	2.7	422	444	110	491	277	n.m.
S07	1070	1.26	26	205	ND	65	3.5	506	428	110	518	257	n.m.
S08	140	1.66	145	567	ND	16	ND	4289	786	197	2936	679	n.m.
S09	861	1.25	27	229	ND	66	3.1	572	451	117	551	273	n.m.
S10	910	1.23	25	210	ND	72	ND	480	432	118	511	260	n.m.
S11	1074	1.05	5	107	ND	31	1.6	54	278	93	275	193	n.m.
S12	727	1.42	21	330	ND	79	3.6	1116	641	117	745	437	n.m.
S13	916	1.22	39	279	ND	68	2.9	717	504	133	629	350	n.m.
S14	1004	1.21	23	192	ND	86	2.8	370	409	122	479	253	n.m.
S15	750	0.82	9	112	ND	48	ND	135	271	71	269	149	n.m.
S16	1256	1.15	5	86	ND	29	1.8	52	288	84	322	226	n.m.
S17	1204	1.11	5	89	ND	27	ND	53	289	86	317	227	n.m.
S18	362	0.35	2	54	ND	9	ND	21	113	18	98	42	n.m.
S19	973	1.39	29	189	ND	61	ND	470	447	115	393	220	n.m.
S20	817	1.27	25	185	ND	108	2.7	335	519	126	381	201	n.m.
S21	2739	2.18	14	200	ND	4	6.9	2762	758	215	598	381	n.m.
S22	607	1.28	15	153	ND	52	ND	489	412	119	384	210	n.m.
S23	978	1.10	18	189	ND	43	ND	361	500	109	417	252	n.m.
S24	989	0.94	9	166	ND	26	ND	56	267	126	261	172	n.m.
S25	1681	1.12	24	326	ND	67	ND	154	537	162	477	377	n.m.
S26	1253	1.19	8	149	ND	31	2.6	60	405	118	286	212	n.m.
S27	1238	0.81	36	414	ND	21	ND	570	616	161	644	440	n.m.
S28	1386	1.06	49	2270	1.4	30	ND	2381	1871	269	1513	1212	n.m.
S29	1121	0.83	56	2718	1.2	54	ND	2125	2234	250	1428	1119	n.m.
S30	1183	1.11	23	268	ND	74	1.8	339	488	122	449	315	n.m.
S31	602	0.74	3	115	ND	11	ND	21	179	53	152	84	n.m.
S32	724	0.68	7	129	ND	31	ND	67	282	62	163	100	n.m.
S33	1056	1.09	24	322	ND	61	1.7	603	699	127	498	369	n.m.
S34	810	0.90	32	867	ND	69	ND	1310	1710	172	620	519	n.m.
S35	1109	1.06	39	579	ND	57	ND	1074	881	150	737	579	n.m.
S36	1080	1.15	15	350	ND	66	2.6	143	548	120	356	263	n.m.
S01	n.m.	0.87	50	437	0.4	7	ND	837	863	146	642	490	n.m.
S02	n.m.	0.82	16	769	0.5	1	ND	1666	2222	186	658	804	n.m.
S03	n.m.	0.92	357	698	0.6	1	ND	1341	460	66	881	300	n.m.
S03	n.m.	n.m.	n.m.	n.m.	n.m.	n.m.	n.m.	n.m.	n.m.	n.m.	n.m.	n.m.	n.m.
S04	n.m.	0.78	44	359	ND	5	ND	567	668	166	639	398	n.m.
S05	n.m.	1.23	51	281	ND	8	1.8	964	802	146	752	392	n.m.

Appendix

N°	DIC (µM ± 10)	DSi (mM ± 0.05)	F^- (µM ± 5)	Cl^- (µM ± 10)	Br^- (µM ± 0.1)	NO_3^- (µM ± 1)	PO_4^{3-} (µM ± 0.1)	SO_4^{2-} (µM ± 10)	Na^+ (µM ± 10)	K^+ (µM ± 5)	Ca^{2+} (µM ± 10)	Mg^{2+} (µM ± 10)	NH_4^+ (µM ± 0.01)
S06	n.m.	1.05	26	195	ND	14	1.0	437	499	125	560	292	n.m.
S07	n.m.	1.06	32	190	ND	15	2.3	507	478	121	566	292	n.m.
S08	n.m.	1.52	185	459	ND	3	ND	3839	855	226	2841	651	n.m.
S09	n.m.	1.08	43	216	ND	10	0.9	813	493	130	770	321	n.m.
S10	n.m.	1.04	32	197	ND	15	1.4	507	503	122	589	286	n.m.
S11	n.m.	0.90	5	77	ND	0	ND	55	276	93	303	200	n.m.
S11	n.m.	n.m.	n.m.	n.m.	n.m.	n.m.	n.m.	n.m.	n.m.	n.m.	n.m.	n.m.	n.m.
S12	n.m.	1.08	32	226	ND	8	ND	686	550	126	635	334	n.m.
S13	n.m.	1.06	42	230	ND	13	ND	650	544	129	525	330	n.m.
S14	n.m.	1.04	23	191	ND	18	1.4	368	427	122	350	282	n.m.
S15	n.m.	0.97	14	136	ND	16	0.7	204	388	116	427	243	n.m.
S15	n.m.	n.m.	n.m.	n.m.	n.m.	n.m.	n.m.	n.m.	n.m.	n.m.	n.m.	n.m.	n.m.
S16	n.m.	0.97	5	83	ND	5	1.2	64	297	93	350	256	n.m.
S17	n.m.	0.90	6	89	ND	1	ND	63	311	101	416	239	n.m.
S19	n.m.	1.20	35	177	ND	13	3.9	496	504	119	520	234	n.m.
S20	n.m.	1.08	29	171	ND	22	ND	330	610	134	514	226	n.m.
S21	n.m.	1.46	13	119	ND	6	ND	1416	480	165	546	336	n.m.
S21	n.m.	1.81	22	175	ND	1	5.7	2697	711	213	711	355	n.m.
S22	n.m.	1.11	16	131	ND	9	ND	505	413	133	484	213	n.m.
S23	n.m.	0.99	32	183	ND	8	ND	379	682	132	568	306	n.m.
S24	n.m.	0.86	9	82	ND	3	ND	56	286	90	350	187	n.m.
S25	n.m.	0.94	27	241	0.2	22	ND	147	508	208	572	422	n.m.
S26	n.m.	0.99	9	135	ND	0	ND	60	431	142	364	274	n.m.
S27	n.m.	0.78	43	294	0.2	1	ND	531	584	181	789	455	n.m.
S28	n.m.	0.94	53	1363	1.0	15	ND	2228	1371	215	1552	1222	n.m.
S29	n.m.	0.90	44	909	0.5	13	ND	1774	1147	175	1346	991	n.m.
S30	n.m.	0.93	20	208	ND	16	ND	315	467	117	524	306	n.m.
S31	n.m.	0.79	2	53	ND	20	ND	25	221	63	116	74	n.m.
S32	n.m.	0.73	8	72	ND	36	ND	82	420	69	236	130	n.m.
S33	n.m.	1.01	17	266	ND	62	ND	601	743	113	644	394	n.m.
S34	n.m.	0.77	28	677	ND	1	ND	1378	1855	190	666	555	n.m.
S35	n.m.	0.90	52	435	ND	1	ND	944	846	171	739	554	n.m.
S36	n.m.	0.97	36	123	ND	1	ND	118	397	137	861	233	n.m.
S37	n.m.	1.20	44	282	ND	10	6.9	1126	612	97	959	423	n.m.
S38	n.m.	1.12	54	234	ND	15	6.3	748	505	127	774	394	n.m.
S39	n.m.	1.27	31	181	ND	20	4.9	452	528	129	557	317	n.m.
S40	n.m.	1.27	33	208	ND	24	5.3	527	552	133	573	357	n.m.
S41	n.m.	1.15	29	238	ND	11	3.4	661	861	115	529	354	n.m.
S42	n.m.	1.85	8	162	ND	1	ND	1779	2643	404	2387	1263	n.m.
S43	n.m.	1.20	9	74	ND	4	ND	956	230	104	378	232	n.m.
S44	n.m.	0.59	5	44	ND	1	ND	22	187	29	190	100	n.m.
S45	n.m.	0.88	6	93	ND	15	ND	52	289	81	245	188	n.m.
S46	n.m.	1.04	48	370	ND	10	3.8	867	670	98	792	432	n.m.

Appendix

N°	DIC (µM ± 10)	DSi (mM ± 0.05)	F^- (µM ± 5)	Cl^- (µM ± 10)	Br^- (µM ± 0.1)	NO_3^- (µM ± 1)	PO_4^{3-} (µM ± 0.1)	SO_4^{2-} (µM ± 10)	Na^+ (µM ± 10)	K^+ (µM ± 5)	Ca^{2+} (µM ± 10)	Mg^{2+} (µM ± 10)	NH_4^+ (µM ± 0.01)
S47	n.m.	0.65	40	147	ND	13	ND	140	302	69	268	158	n.m.
S48	n.m.	0.81	5	64	ND	1	ND	27	248	52	227	196	n.m.
S49	n.m.	2.75	22	174	ND	1	3.7	3209	1073	271	837	518	n.m.
S49	n.m.	2.76	22	213	ND	1	ND	1284	1283	283	1010	913	n.m.
S01	n.m.	0.59	68	547	ND	15	ND	1311	937	165	791	616	n.m.
S01	n.m.	0.52	52	448	ND	11	ND	1065	774	155	648	489	n.m.
S02	n.m.	0.59	5	88	ND	ND	ND	96	264	67	199	133	n.m.
S03	n.m.	0.80	724	1686	ND	4	ND	2500	731	117	1869	437	n.m.
S04	n.m.	0.50	44	260	ND	5	ND	457	452	139	542	358	n.m.
S05	n.m.	1.01	53	263	ND	12	ND	874	783	148	785	384	n.m.
S06	n.m.	0.83	39	217	ND	12	ND	651	524	123	576	311	n.m.
S07	n.m.	0.90	27	164	ND	13	ND	540	428	118	548	277	n.m.
S08	n.m.	1.30	180	496	ND	3	ND	4934	846	229	ND	737	n.m.
S09	n.m.	0.87	43	858	ND	13	ND	797	1013	136	736	305	n.m.
S10	n.m.	0.87	42	191	ND	17	ND	556	462	132	625	300	n.m.
S11	n.m.	0.70	15	90	ND	5	ND	97	270	96	277	255	n.m.
S12	n.m.	0.99	24	274	ND	16	ND	1150	614	119	799	422	n.m.
S13	n.m.	0.81	42	289	ND	15	ND	685	514	140	608	333	n.m.
S14	n.m.	0.81	27	170	ND	14	ND	408	402	117	489	262	n.m.
S15	n.m.	0.61	9	121	ND	12	ND	162	287	79	326	171	n.m.
S16	n.m.	0.82	6	86	ND	6	ND	58	298	89	331	231	n.m.
S17	n.m.	0.81	9	83	ND	4	ND	60	274	92	326	222	n.m.
S18	n.m.	0.29	ND	45	ND	3	ND	24	112	22	127	42	n.m.
S19	n.m.	1.01	34	155	ND	14	ND	504	452	122	418	225	n.m.
S20	n.m.	0.94	30	154	ND	22	ND	350	503	139	400	215	n.m.
S21	n.m.	1.74	31	145	ND	5	15.5	9499	784	269	897	492	n.m.
S22	n.m.	0.69	13	142	ND	13	ND	330	378	132	380	218	n.m.
S23	n.m.	0.80	24	186	ND	8	ND	378	680	133	410	292	n.m.
S23	n.m.	0.50	29	121	ND	9	ND	274	397	102	300	178	n.m.
S24	n.m.	0.71	9	91	ND	2	ND	52	277	94	268	181	n.m.
S25	n.m.	0.65	34	314	ND	73	ND	254	561	260	483	399	n.m.
S26	n.m.	0.69	n.m.	n.m.	n.m.	n.m.	n.m.	n.m.	n.m.	n.m.	n.m.	n.m.	n.m.
S27	n.m.	0.62	n.m.	n.m.	n.m.	n.m.	n.m.	n.m.	n.m.	n.m.	n.m.	n.m.	n.m.
S28	n.m.	0.74	124	894	ND	ND	ND	2675	1470	330	2174	1348	n.m.
S29	n.m.	0.66	52	895	ND	19	ND	2193	1385	280	1412	1088	n.m.
S30	n.m.	0.65	n.m.	n.m.	n.m.	n.m.	n.m.	n.m.	n.m.	n.m.	n.m.	n.m.	n.m.
S31	n.m.	0.61	3	89	ND	2	ND	24	205	58	173	98	n.m.
S32	n.m.	2.28	26	213	ND	15	ND	205	502	114	287	188	n.m.
S33	n.m.	0.77	n.m.	n.m.	n.m.	n.m.	n.m.	n.m.	n.m.	n.m.	n.m.	n.m.	n.m.
S34	n.m.	0.63	38	584	ND	ND	ND	1206	1766	222	1014	651	n.m.
S35	n.m.	0.66	45	550	ND	13	ND	1169	950	175	789	618	n.m.
S36	n.m.	0.79	20	138	ND	13	ND	90	360	144	293	215	n.m.
S37	n.m.	1.04	44	251	ND	11	ND	1096	556	125	778	387	n.m.

Appendix

N°	DIC (µM ± 10)	DSi (mM ± 0.05)	F^- (µM ± 5)	Cl^- (µM ± 10)	Br^- (µM ± 0.1)	NO_3^- (µM ± 1)	PO_4^{3-} (µM ± 0.1)	SO_4^{2-} (µM ± 10)	Na^+ (µM ± 10)	K^+ (µM ± 5)	Ca^{2+} (µM ± 10)	Mg^{2+} (µM ± 10)	NH_4^+ (µM ± 0.01)
S38	n.m.	0.98	62	207	ND	18	ND	743	465	124	643	324	n.m.
S39	n.m.	1.11	25	165	ND	21	ND	482	501	157	470	259	n.m.
S40	n.m.	1.10	40	185	ND	15	ND	499	529	167	460	269	n.m.
S41	n.m.	1.00	40	234	ND	9	ND	667	799	139	450	334	n.m.
S42	n.m.	2.49	8	152	ND	1	ND	1688	2495	506	2340	1216	n.m.
S43	n.m.	1.69	36	78	ND	ND	12.8	8014	439	176	659	453	n.m.
S44	n.m.	0.52	2	44	ND	ND	3.3	20	166	32	209	87	n.m.
S45	n.m.	0.83	6	83	ND	15	ND	45	300	103	207	153	n.m.
S46	n.m.	0.91	45	360	ND	9	ND	837	642	131	677	406	n.m.
S47	n.m.	0.55	24	179	ND	17	ND	189	344	85	250	153	n.m.
S48	n.m.	0.71	5	54	ND	ND	ND	25	238	67	217	151	n.m.
S49	n.m.	2.16	25	149	ND	ND	ND	2590	927	284	662	491	n.m.
S49	n.m.	2.60	22	191	ND	333	ND	1302	1269	436	916	805	n.m.
S01	n.m.	n.m.	30	287	ND	13	ND	652	609	132	508	394	ND
S01	n.m.	n.m.	33	324	ND	13	ND	738	676	144	567	448	ND
S01	n.m.	n.m.	15	105	0.7	5	ND	307	240	52	297	156	ND
S03	n.m.	n.m.	154	599	1.5	1	ND	940	335	71	663	185	ND
S04	n.m.	n.m.	10	21	ND	2	ND	49	60	18	194	53	ND
S07	n.m.	n.m.	13	15	1.6	1	ND	85	36	13	164	35	8.39
S19	n.m.	n.m.	24	142	0.3	19	1.4	427	434	120	405	221	ND
S22	n.m.	n.m.	12	120	1.4	16	ND	362	374	125	351	195	ND
S23	n.m.	n.m.	6	14	ND	2	ND	49	69	17	152	36	ND
S27	n.m.	n.m.	n.m.	n.m.	n.m.	n.m.	n.m.	n.m.	n.m.	n.m.	n.m.	n.m.	n.m.
S28	n.m.	n.m.	33	219	ND	3	ND	915	312	86	810	303	ND
S29	n.m.	n.m.	43	724	ND	10	ND	1560	938	222	1109	861	ND
S30	n.m.	n.m.	17	169	ND	13	ND	233	417	140	418	305	ND
S33	n.m.	n.m.	13	52	ND	3	ND	151	162	35	212	100	ND
S34	n.m.	n.m.	22	304	ND	15	ND	440	674	118	334	226	10.94
S35	n.m.	n.m.	26	316	ND	14	ND	694	656	147	559	427	ND
S36	n.m.	n.m.	9	115	0.8	13	ND	80	326	125	305	220	8.85
S46	n.m.	n.m.	16	56	ND	2	ND	196	128	27	221	90	ND
S03	n.m.	n.m.	255	610	n.m.	1	n.m.	1832	407	84	1964	299	n.m.
S18	n.m.	n.m.	n.m.	38	n.m.	0	n.m.	19	108	28	100	40	n.m.
S50	n.m.	n.m.	n.m.	n.m.	n.m.	n.m.	n.m.	n.m.	n.m.	n.m.	n.m.	n.m.	n.m.
S51	n.m.	n.m.	n.m.	n.m.	n.m.	n.m.	n.m.	n.m.	n.m.	n.m.	n.m.	n.m.	n.m.
S01	870	n.m.	39	377	1.6	10	n.m.	844	797	151	570	493	14.69
S07	955	n.m.	28	152	2.1	17	1.8	420	419	114	546	270	n.m.
S23	n.m.	n.m.	21	127	0.8	29	n.m.	247	459	106	386	230	n.m.
S28	830	n.m.	40	519	0.9	29	n.m.	992	699	165	922	554	9.01
S37	n.m.	n.m.	46	205	n.m.	14	3.0	681	494	109	640	329	n.m.
S46	890	n.m.	51	342	1.0	13	1.0	719	634	125	653	411	5.07
S52	n.m.	n.m.	313	3368	5.5	40	n.m.	8577	5222	527	4043	3695	355.04
S53	n.m.	n.m.	19	126	2.4	15	n.m.	288	169	45	213	81	12.93

Appendix

N°	DIC (µM ± 10)	DSi (mM ± 0.05)	F^- (µM ± 5)	Cl^- (µM ± 10)	Br^- (µM ± 0.1)	NO_3^- (µM ± 1)	PO_4^{3-} (µM ± 0.1)	SO_4^{2-} (µM ± 10)	Na^+ (µM ± 10)	K^+ (µM ± 5)	Ca^{2+} (µM ± 10)	Mg^{2+} (µM ± 10)	NH_4^+ (µM ± 0.01)
S54	n.m.	n.m.	33	292	1.6	11	n.m.	646	471	138	592	444	8.12
S55	n.m.	n.m.	65	1267	2.1	2	1.6	2972	6374	575	793	1052	90.50
S07	1115	1.15	24	156	n.m.	14	1.6	475	398	101	509	257	n.m.
S08	n.m.	1.50	100	381	1.2	3	n.m.	2896	644	194	2332	591	n.m.
S16	1381	1.01	4	65	n.m.	5	n.m.	47	257	81	334	222	n.m.
S19	964	1.24	28	137	n.m.	10	2.3	428	387	105	374	204	n.m.
S37	1045	1.22	39	211	n.m.	10	2.4	857	472	103	702	331	n.m.
S38	1326	1.21	33	182	n.m.	18	2.2	614	409	115	572	294	n.m.
S39	1663	1.23	23	144	n.m.	24	2.1	350	450	135	426	237	n.m.
S40	1773	1.26	31	157	n.m.	23	2.5	393	472	146	424	256	n.m.
S44	670	0.57	1	36	n.m.	1	n.m.	17	160	32	156	74	n.m.
S45	1089	0.95	4	81	n.m.	19	n.m.	41	274	84	287	158	n.m.
S46	1000	1.13	42	330	n.m.	7	n.m.	753	572	109	604	372	n.m.
S47	769	0.68	17	138	n.m.	11	n.m.	113	268	66	236	128	n.m.
S48	992	0.85	3	46	n.m.	5	n.m.	19	222	54	199	147	n.m.
S50	9690	2.48	2	69	2.2	7	n.m.	570	447	158	2019	931	22.78
S50	n.m.	n.m.	n.m.	n.m.	n.m.	n.m.	n.m.	n.m.	n.m.	n.m.	n.m.	n.m.	n.m.
S51	1006	1.80	25	75	0.9	185	n.m.	1149	738	272	461	362	746.05
S52	2181	1.29	274	3225	3.7	3	n.m.	5853	6040	538	4148	3477	354.03
S55	3344	2.00	53	1187	1.7	0	n.m.	2606	5826	523	723	953	71.99
S56	1660	1.46	21	243	n.m.	24	2.6	1119	577	108	844	411	n.m.
S57	1179	1.18	80	610	0.9	14	n.m.	1265	897	147	874	651	n.m.
S58	1605	1.16	27	253	n.m.	36	n.m.	552	497	125	631	376	n.m.
S59	1524	1.16	35	306	n.m.	43	n.m.	646	590	155	737	442	n.m.
S60	4860	1.51	28	229	n.m.	3	n.m.	494	2671	304	570	719	n.m.
S61	8007	2.29	24	906	1.7	0	n.m.	1836	8390	960	672	949	n.m.
S62	6718	2.67	20	762	2.8	0	n.m.	1606	7136	819	623	824	n.m.
S63	n.m.	1.33	48	846	1.0	5	n.m.	2060	2825	224	932	1195	n.m.
R1A	n.m.	n.m.	n.m.	5	n.m.	1	n.m.	2	10	6	n.m.	n.m.	n.m.
R1B	n.m.	n.m.	n.m.	n.m.	n.m.	n.m.	n.m.	n.m.	n.m.	n.m.	n.m.	n.m.	n.m.
R2A	n.m.	n.m.	n.m.	n.m.	n.m.	n.m.	n.m.	n.m.	n.m.	n.m.	n.m.	n.m.	n.m.
R2B	n.m.	n.m.	n.m.	n.m.	n.m.	n.m.	n.m.	n.m.	n.m.	n.m.	n.m.	n.m.	n.m.
R2C	n.m.	n.m.	n.m.	n.m.	n.m.	n.m.	n.m.	n.m.	n.m.	n.m.	n.m.	n.m.	n.m.

n.m. Not measured.

ND. Not detected.

Table A.3. Results of stable isotope ratios, fractions of sulphate (F) from mixing model and fraction of magmatic carbon (FC_{magma}). Charge balance error (CBE) and ratio of magmatic carbon over magmatic sulphur (C_m:S_m) for water samples in Aso caldera.

N°	$\delta^{13}C_{DIC}$ (‰ ± 0.01)	$\delta^{18}O_{H2O}$ (‰ ± 0.5)	$\delta^{2}H_{H2O}$ (‰ ± 0.05)	$\delta^{18}O_{SO4}$ (‰ ± 0.3)	$\delta^{34}S_{SO4}$ (‰ ± 0.2)	F_{soil} (± 0.1)	$F_{H\text{-}I}$ (± 0.1)	$F_{H\text{-}II}$ (± 0.1)	FC_{magma} (±0.1)	CBE (%)	C_m:S_m
S01	-11.31	-6.9	-42.16	8.8	5.2	0.14	0.72	0.15	0.3	2.7	n.c.
S02	-11.18	-7.4	-45.29	13.4	15.1	0.05	0.12	0.83	0.3	3.1	n.c.
S03	n.m.	-5.7	-27.59	9.5	7.2	0.28	0.47	0.25	n.c.	11.0	n.c.
S04	-11.10	-7.6	-48.44	6.2	6.3	0.74	0.18	0.08	0.3	2.4	n.c.
S05	-6.95	-8.1	-52.53	7.6	8.1	0.37	0.35	0.29	0.6	2.5	n.c.
S06	-10.82	-8.2	-52.63	5.9	6.0	0.57	0.33	0.10	0.3	1.9	n.c.
S07	-13.95	-8.4	-53.90	5.2	5.7	0.11	0.71	0.18	0.4	2.6	0.42
S08	n.m.	-8.4	-53.53	9.2	9.4	0.04	0.51	0.45	n.c.	6.7	n.c.
S09	-11.45	-8.4	-53.65	5.9	6.2	0.78	0.15	0.06	0.3	2.4	1.27
S10	-11.28	-8.3	-53.62	5.7	5.7	1.00	0.00	0.00	0.3	1.9	n.c.
S11	-12.74	-8.3	-53.19	3.7	5.2	0.63	0.33	0.03	0.2	1.7	0.50
S12	-7.93	-8.1	-52.26	7.6	7.4	0.16	0.55	0.29	0.5	3.2	0.62
S13	-10.78	-8.0	-51.76	7.4	6.5	0.53	0.33	0.14	0.3	2.2	0.68
S14	-11.85	-8.2	-53.06	5.8	5.4	1.00	0.00	0.00	0.2	1.8	n.c.
S15	-10.59	-7.7	-50.70	5.6	5.6	0.90	0.10	n.c.	0.3	1.0	3.24
S16	-15.28	-8.4	-53.46	2.6	5.5	0.39	0.50	0.11	0.3	1.5	0.47
S17	-13.89	-8.4	-53.21	3.1	5.2	1.00	0.00	0.00	0.1	1.9	n.c.
S18	-7.06	-8.3	-51.52	3.7	7.9	n.c.	n.c.	n.c.	0.6	0.7	n.c.
S19	-10.46	-8.4	-53.69	5.6	6.3	1.00	0.00	0.02	0.6	2.0	25.71
S20	-10.23	-8.0	-51.52	6.4	6.0	0.72	0.21	0.07	0.4	1.7	1.30
S21	-6.67	-8.1	-53.34	-2.8	2.6	0.00	0.99	0.01	0.9	17.8	0.89
S22	-8.99	-8.0	-50.81	3.8	4.8	0.29	0.63	0.08	0.4	1.7	0.63
S23	-9.81	-8.1	-51.94	7.1	8.5	0.50	0.22	0.29	0.4	0.9	0.77
S24	-10.36	-8.1	-51.67	5.6	7.2	0.74	0.12	0.14	0.4	1.5	1.37
S25	-11.11	-7.9	-51.24	7.6	8.1	1.00	0.00	0.00	0.3	2.1	n.c.
S26	-10.75	-8.0	-51.10	6.3	9.6	0.57	0.09	0.34	0.3	2.1	0.74
S27	-12.99	-7.6	-49.66	6.9	5.9	0.68	0.26	0.07	0.2	2.6	0.52
S28	-13.72	-7.5	-49.12	7.8	2.5	n.c.	1.00	0.00	0.1	4.8	n.c.
S29	-11.00	-7.6	-49.53	9.5	8.7	0.11	0.51	0.39	0.3	5.0	0.34
S30	-11.13	-7.8	-50.50	6.9	6.8	0.23	0.53	0.23	0.3	3.7	0.39
S31	-9.95	-7.9	-50.28	9.7	6.2	0.18	0.62	0.20	0.4	1.1	0.46
S32	-12.70	-7.2	-45.91	10.0	14.3	0.22	0.04	0.74	0.2	3.5	0.24
S33	-8.44	-7.9	-51.31	9.3	9.5	0.25	0.34	0.41	0.5	2.7	0.65
S34	-7.47	-8.0	-52.06	11.5	13.5	0.15	0.15	0.70	0.6	3.1	0.65
S35	-10.87	-7.8	-51.11	9.6	9.3	0.16	0.42	0.41	0.3	3.4	0.38
S36	-10.90	-7.9	-51.79	6.8	7.1	1.00	0.00	0.00	0.3	2.2	n.c.
S01	n.m.	-7.8	-49.66	n.m.	n.m.	n.c.	n.c.	n.c.	n.c.	2.3	n.c.
S02	n.m.	-7.9	-49.53	n.m.	n.m.	n.c.	n.c.	n.c.	n.c.	1.7	n.c.
S03	n.m.	-8.3	-52.85	n.m.	n.m.	n.c.	n.c.	n.c.	n.c.	23.4	n.c.
S03	n.m.	n.m.	n.m.	n.m.	n.m.	n.c.	n.c.	n.c.	n.c.	100.0	n.c.

N°	$\delta^{13}C_{DIC}$ (‰ ± 0.01)	$\delta^{18}O_{H2O}$ (‰ ± 0.5)	$\delta^{2}H_{H2O}$ (‰ ± 0.05)	$\delta^{18}O_{SO4}$ (‰ ± 0.3)	$\delta^{34}S_{SO4}$ (‰ ± 0.2)	F_{soil} (± 0.1)	F_{H-I} (± 0.1)	F_{H-II} (± 0.1)	FC_{magma} (±0.1)	CBE (%)	C_m:S_m
S04	n.m.	-7.8	-50.05	n.m.	n.m.	n.c.	n.c.	n.c.	n.c.	3.9	n.c.
S05	n.m.	-8.2	-52.73	n.m.	n.m.	n.c.	n.c.	n.c.	n.c.	3.5	n.c.
S06	n.m.	-8.2	-52.75	n.m.	n.m.	n.c.	n.c.	n.c.	n.c.	5.0	n.c.
S07	n.m.	-8.4	-53.78	n.m.	n.m.	n.c.	n.c.	n.c.	n.c.	4.7	n.c.
S08	n.m.	-8.6	-54.74	n.m.	n.m.	n.c.	n.c.	n.c.	n.c.	6.3	n.c.
S09	n.m.	n.m.	n.m.	n.m.	n.m.	n.c.	n.c.	n.c.	n.c.	3.2	n.c.
S10	n.m.	-8.3	-53.25	n.m.	n.m.	n.c.	n.c.	n.c.	n.c.	3.5	n.c.
S11	n.m.	-8.0	-52.03	n.m.	n.m.	n.c.	n.c.	n.c.	n.c.	4.1	n.c.
S11	n.m.	n.m.	n.m.	n.m.	n.m.	n.c.	n.c.	n.c.	n.c.	100.0	n.c.
S12	n.m.	-8.2	-52.91	n.m.	n.m.	n.c.	n.c.	n.c.	n.c.	2.9	n.c.
S13	n.m.	n.m.	n.m.	n.m.	n.m.	n.c.	n.c.	n.c.	n.c.	1.6	n.c.
S14	n.m.	-8.2	-53.24	n.m.	n.m.	n.c.	n.c.	n.c.	n.c.	5.3	n.c.
S15	n.m.	-8.2	-52.96	n.m.	n.m.	n.c.	n.c.	n.c.	n.c.	6.1	n.c.
S15	n.m.	-8.2	-52.99	n.m.	n.m.	n.c.	n.c.	n.c.	n.c.	100.0	n.c.
S16	n.m.	-8.5	-53.98	n.m.	n.m.	n.c.	n.c.	n.c.	n.c.	2.7	n.c.
S17	n.m.	-8.4	-53.52	n.m.	n.m.	n.c.	n.c.	n.c.	n.c.	8.0	n.c.
S19	n.m.	-8.4	-53.86	n.m.	n.m.	n.c.	n.c.	n.c.	n.c.	5.9	n.c.
S20	n.m.	n.m.	n.m.	n.m.	n.m.	n.c.	n.c.	n.c.	n.c.	10.9	n.c.
S21	n.m.	-8.5	-55.04	n.m.	n.m.	n.c.	n.c.	n.c.	n.c.	22.4	n.c.
S21	n.m.	-7.8	-55.12	n.m.	n.m.	n.c.	n.c.	n.c.	n.c.	17.2	n.c.
S22	n.m.	-7.9	-53.53	n.m.	n.m.	n.c.	n.c.	n.c.	n.c.	3.8	n.c.
S23	n.m.	-7.9	-53.87	n.m.	n.m.	n.c.	n.c.	n.c.	n.c.	8.9	n.c.
S24	n.m.	-8.0	-54.02	n.m.	n.m.	n.c.	n.c.	n.c.	n.c.	7.7	n.c.
S25	n.m.	-7.7	-52.57	n.m.	n.m.	n.c.	n.c.	n.c.	n.c.	9.9	n.c.
S26	n.m.	-7.7	-52.79	n.m.	n.m.	n.c.	n.c.	n.c.	n.c.	9.7	n.c.
S27	n.m.	-7.4	-51.79	n.m.	n.m.	n.c.	n.c.	n.c.	n.c.	5.3	n.c.
S28	n.m.	-7.3	-50.72	n.m.	n.m.	n.c.	n.c.	n.c.	n.c.	0.3	n.c.
S29	n.m.	-7.7	-52.85	n.m.	n.m.	n.c.	n.c.	n.c.	n.c.	1.2	n.c.
S30	n.m.	-7.5	-51.89	n.m.	n.m.	n.c.	n.c.	n.c.	n.c.	6.2	n.c.
S31	n.m.	-7.8	-53.41	n.m.	n.m.	n.c.	n.c.	n.c.	n.c.	7.0	n.c.
S32	n.m.	-7.7	-52.88	n.m.	n.m.	n.c.	n.c.	n.c.	n.c.	7.5	n.c.
S33	n.m.	-7.7	-53.12	n.m.	n.m.	0.3	0.5	0.2	n.c.	4.4	n.c.
S34	n.m.	-7.9	-54.82	n.m.	n.m.	n.c.	n.c.	n.c.	n.c.	1.7	n.c.
S35	n.m.	-7.7	-52.93	n.m.	n.m.	n.c.	n.c.	n.c.	n.c.	2.8	n.c.
S36	n.m.	-7.7	-53.04	n.m.	n.m.	n.c.	n.c.	n.c.	n.c.	28.0	n.c.
S37	n.m.	-8.1	-55.86	n.m.	n.m.	n.c.	n.c.	n.c.	n.c.	5.2	n.c.
S38	n.m.	-8.2	-52.68	n.m.	n.m.	n.c.	n.c.	n.c.	n.c.	9.3	n.c.
S39	n.m.	-8.1	-52.14	n.m.	n.m.	n.c.	n.c.	n.c.	n.c.	8.3	n.c.
S40	n.m.	-8.0	-51.69	n.m.	n.m.	n.c.	n.c.	n.c.	n.c.	6.6	n.c.
S41	n.m.	-8.3	-52.44	n.m.	n.m.	n.c.	n.c.	n.c.	n.c.	4.4	n.c.
S42	n.m.	-7.7	-52.22	n.m.	n.m.	n.c.	n.c.	n.c.	n.c.	11.7	n.c.
S43	n.m.	-8.0	-53.42	n.m.	n.m.	n.c.	n.c.	n.c.	n.c.	60.8	n.c.
S44	n.m.	-8.2	-51.38	n.m.	n.m.	n.c.	n.c.	n.c.	n.c.	9.8	n.c.

N°	$\delta^{13}C_{DIC}$ (‰ ± 0.01)	$\delta^{18}O_{H2O}$ (‰ ± 0.5)	$\delta^{2}H_{H2O}$ (‰ ± 0.05)	$\delta^{18}O_{SO4}$ (‰ ± 0.3)	$\delta^{34}S_{SO4}$ (‰ ± 0.2)	F_{soil} (± 0.1)	F_{H-I} (± 0.1)	F_{H-II} (± 0.1)	FC_{magma} (±0.1)	CBE (%)	C_m:S_m
S45	n.m.	-7.9	-50.29	n.m.	n.m.	n.c.	n.c.	n.c.	n.c.	9.0	n.c.
S46	n.m.	-8.5	-54.07	n.m.	n.m.	n.c.	n.c.	n.c.	n.c.	4.0	n.c.
S47	n.m.	-8.2	-52.89	n.m.	n.m.	n.c.	n.c.	n.c.	n.c.	6.4	n.c.
S48	n.m.	-8.1	-50.48	n.m.	n.m.	n.c.	n.c.	n.c.	n.c.	6.7	n.c.
S49	n.m.	-8.2	-54.77	n.m.	n.m.	n.c.	n.c.	n.c.	n.c.	32.1	n.c.
S49	n.m.	n.m.	n.m.	n.m.	n.m.	n.c.	n.c.	n.c.	n.c.	2.6	n.c.
S01	n.m.	-6.7	-41.70	n.m.	n.m.	n.c.	n.c.	n.c.	n.c.	1.8	n.c.
S01	n.m.	-6.6	-39.94	n.m.	n.m.	n.c.	n.c.	n.c.	n.c.	1.4	n.c.
S02	n.m.	-7.8	-48.54	n.m.	n.m.	n.c.	n.c.	n.c.	n.c.	1.2	n.c.
S03	n.m.	-6.7	-39.74	n.m.	n.m.	n.c.	n.c.	n.c.	n.c.	14.7	n.c.
S04	n.m.	-6.5	-41.20	n.m.	n.m.	n.c.	n.c.	n.c.	n.c.	0.5	n.c.
S05	n.m.	-7.7	-49.40	n.m.	n.m.	n.c.	n.c.	n.c.	n.c.	5.8	n.c.
S06	n.m.	-7.7	-49.37	n.m.	n.m.	n.c.	n.c.	n.c.	n.c.	0.4	n.c.
S07	n.m.	-8.4	-53.50	n.m.	n.m.	n.c.	n.c.	n.c.	n.c.	0.6	n.c.
S08	n.m.	-8.4	-53.46	n.m.	n.m.	n.c.	n.c.	n.c.	n.c.	60.7	n.c.
S09	n.m.	-8.2	-51.82	n.m.	n.m.	n.c.	n.c.	n.c.	n.c.	0.1	n.c.
S10	n.m.	-7.9	-50.21	n.m.	n.m.	n.c.	n.c.	n.c.	n.c.	0.1	n.c.
S11	n.m.	-8.1	-51.11	n.m.	n.m.	n.c.	n.c.	n.c.	n.c.	7.7	n.c.
S12	n.m.	-8.0	-50.72	n.m.	n.m.	n.c.	n.c.	n.c.	n.c.	0.1	n.c.
S13	n.m.	-7.5	-48.04	n.m.	n.m.	n.c.	n.c.	n.c.	n.c.	0.7	n.c.
S14	n.m.	-7.9	-50.26	n.m.	n.m.	n.c.	n.c.	n.c.	n.c.	1.4	n.c.
S15	n.m.	-8.1	-51.08	n.m.	n.m.	n.c.	n.c.	n.c.	n.c.	1.7	n.c.
S16	n.m.	-8.5	-53.40	n.m.	n.m.	n.c.	n.c.	n.c.	n.c.	1.1	n.c.
S17	n.m.	-8.1	-50.93	n.m.	n.m.	n.c.	n.c.	n.c.	n.c.	1.5	n.c.
S18	n.m.	-7.8	-47.30	n.m.	n.m.	n.c.	n.c.	n.c.	n.c.	1.4	n.c.
S19	n.m.	-8.4	-53.63	n.m.	n.m.	n.c.	n.c.	n.c.	n.c.	0.7	n.c.
S20	n.m.	-7.9	-50.46	n.m.	n.m.	n.c.	n.c.	n.c.	n.c.	2.7	n.c.
S21	n.m.	-8.0	-52.34	n.m.	n.m.	n.c.	n.c.	n.c.	n.c.	27.4	n.c.
S22	n.m.	-6.9	-44.33	n.m.	n.m.	n.c.	n.c.	n.c.	n.c.	1.4	n.c.
S23	n.m.	-7.6	-48.60	n.m.	n.m.	n.c.	n.c.	n.c.	n.c.	0.1	n.c.
S23	n.m.	-6.9	-41.79	n.m.	n.m.	n.c.	n.c.	n.c.	n.c.	0.0	n.c.
S24	n.m.	-7.9	-49.68	n.m.	n.m.	n.c.	n.c.	n.c.	n.c.	1.9	n.c.
S25	n.m.	-6.3	-40.93	n.m.	n.m.	n.c.	n.c.	n.c.	n.c.	2.1	n.c.
S26	n.m.	-7.1	-44.33	n.m.	n.m.	n.c.	n.c.	n.c.	n.c.	100.0	n.c.
S27	n.m.	-6.7	-43.61	n.m.	n.m.	n.c.	n.c.	n.c.	n.c.	100.0	n.c.
S28	n.m.	-7.2	-47.08	n.m.	n.m.	n.c.	n.c.	n.c.	n.c.	1.3	n.c.
S29	n.m.	-6.2	-39.12	n.m.	n.m.	n.c.	n.c.	n.c.	n.c.	3.8	n.c.
S30	n.m.	-6.9	-43.85	n.m.	n.m.	n.c.	n.c.	n.c.	n.c.	100.0	n.c.
S31	n.m.	-7.8	-48.98	n.m.	n.m.	n.c.	n.c.	n.c.	n.c.	2.2	n.c.
S32	n.m.	-6.6	-41.54	n.m.	n.m.	n.c.	n.c.	n.c.	n.c.	2.1	n.c.
S33	n.m.	-7.5	-47.54	n.m.	n.m.	n.c.	n.c.	n.c.	n.c.	100.0	n.c.
S34	n.m.	-7.4	-46.55	n.m.	n.m.	n.c.	n.c.	n.c.	n.c.	14.3	n.c.
S35	n.m.	-6.8	-42.80	n.m.	n.m.	n.c.	n.c.	n.c.	n.c.	0.3	n.c.

N°	$\delta^{13}C_{DIC}$ (‰ ± 0.01)	$\delta^{18}O_{H2O}$ (‰ ± 0.5)	$\delta^{2}H_{H2O}$ (‰ ± 0.05)	$\delta^{18}O_{SO4}$ (‰ ± 0.3)	$\delta^{34}S_{SO4}$ (‰ ± 0.2)	F_{soil} (± 0.1)	F_{H-I} (± 0.1)	F_{H-II} (± 0.1)	FC_{magma} (±0.1)	CBE (%)	C_m:S_m
S36	n.m.	-7.4	-47.18	n.m.	n.m.	n.c.	n.c.	n.c.	n.c.	3.5	n.c.
S37	n.m.	-8.5	-53.79	n.m.	n.m.	n.c.	n.c.	n.c.	n.c.	0.5	n.c.
S38	n.m.	n.m.	n.m.	n.m.	n.m.	n.c.	n.c.	n.c.	n.c.	1.1	n.c.
S39	n.m.	n.m.	n.m.	n.m.	n.m.	n.c.	n.c.	n.c.	n.c.	1.6	n.c.
S40	n.m.	n.m.	n.m.	n.m.	n.m.	n.c.	n.c.	n.c.	n.c.	0.3	n.c.
S41	n.m.	n.m.	n.m.	n.m.	n.m.	n.c.	n.c.	n.c.	n.c.	0.6	n.c.
S42	n.m.	n.m.	n.m.	n.m.	n.m.	n.c.	n.c.	n.c.	n.c.	0.7	n.c.
S43	n.m.	n.m.	n.m.	n.m.	n.m.	n.c.	n.c.	n.c.	n.c.	41.6	n.c.
S44	n.m.	n.m.	n.m.	n.m.	n.m.	n.c.	n.c.	n.c.	n.c.	9.0	n.c.
S45	n.m.	n.m.	n.m.	n.m.	n.m.	n.c.	n.c.	n.c.	n.c.	4.0	n.c.
S46	n.m.	n.m.	n.m.	n.m.	n.m.	n.c.	n.c.	n.c.	n.c.	0.5	n.c.
S47	n.m.	n.m.	n.m.	n.m.	n.m.	n.c.	n.c.	n.c.	n.c.	4.6	n.c.
S48	n.m.	n.m.	n.m.	n.m.	n.m.	n.c.	n.c.	n.c.	n.c.	2.0	n.c.
S49	n.m.	n.m.	n.m.	n.m.	n.m.	n.c.	n.c.	n.c.	n.c.	15.9	n.c.
S49	n.m.	n.m.	n.m.	n.m.	n.m.	n.c.	n.c.	n.c.	n.c.	24.1	n.c.
S01	n.m.	-7.5	-49.71	n.m.	n.m.	n.c.	n.c.	n.c.	n.c.	0.8	n.c.
S01	n.m.	n.m.	n.m.	n.m.	n.m.	n.c.	n.c.	n.c.	n.c.	21.4	n.c.
S01	n.m.	n.m.	n.m.	n.m.	n.m.	n.c.	n.c.	n.c.	n.c.	23.7	n.c.
S03	n.m.	-8.3	-55.71	n.m.	n.m.	n.c.	n.c.	n.c.	n.c.	11.1	n.c.
S04	n.m.	-7.7	-51.85	n.m.	n.m.	n.c.	n.c.	n.c.	n.c.	0.6	n.c.
S07	n.m.	-8.4	-54.94	n.m.	n.m.	n.c.	n.c.	n.c.	n.c.	1.1	n.c.
S19	n.m.	-8.3	-55.02	n.m.	n.m.	n.c.	n.c.	n.c.	n.c.	2.4	n.c.
S22	n.m.	-8.1	-53.09	n.m.	n.m.	n.c.	n.c.	n.c.	n.c.	1.5	n.c.
S23	n.m.	-8.0	-52.46	n.m.	n.m.	n.c.	n.c.	n.c.	n.c.	2.0	n.c.
S27	n.m.	-7.4	-50.32	n.m.	n.m.	n.c.	n.c.	n.c.	n.c.	99.9	n.c.
S28	n.m.	-7.2	-48.28	n.m.	n.m.	n.c.	n.c.	n.c.	n.c.	1.1	n.c.
S29	n.m.	-7.0	-47.45	n.m.	n.m.	n.c.	n.c.	n.c.	n.c.	0.7	n.c.
S30	n.m.	-7.6	-50.44	n.m.	n.m.	n.c.	n.c.	n.c.	n.c.	2.5	n.c.
S33	n.m.	-7.8	-51.30	n.m.	n.m.	0.85	0.12	0.04	n.c.	3.4	n.c.
S34	n.m.	-7.7	-49.51	n.m.	n.m.	n.c.	n.c.	n.c.	n.c.	1.2	n.c.
S35	n.m.	-7.7	-50.62	n.m.	n.m.	n.c.	n.c.	n.c.	n.c.	1.0	n.c.
S36	n.m.	-8.0	-52.33	n.m.	n.m.	n.c.	n.c.	n.c.	n.c.	1.6	n.c.
S46	n.m.	-8.5	-55.90	n.m.	n.m.	n.c.	n.c.	n.c.	n.c.	2.8	n.c.
S03	n.m.	n.m.	n.m.	n.m.	n.m.	n.c.	n.c.	n.c.	n.c.	5.9	n.c.
S18	n.m.	n.m.	n.m.	n.m.	n.m.	n.c.	n.c.	n.c.	n.c.	2.4	n.c.
S50	n.m.	n.m.	n.m.	n.m.	n.m.	n.c.	n.c.	n.c.	n.c.	100.0	n.c.
S51	n.m.	n.m.	n.m.	n.m.	n.m.	n.c.	n.c.	n.c.	n.c.	100.0	n.c.
S01	-11.10	n.m.	n.m.	n.m.	n.m.	n.c.	n.c.	n.c.	0.3	2.3	0.36
S07	-11.35	n.m.	n.m.	n.m.	n.m.	n.c.	n.c.	n.c.	0.6	5.1	n.c.
S23	n.m.	n.m.	n.m.	n.m.	n.m.	n.c.	n.c.	n.c.	n.c.	3.5	n.c.
S28	-11.10	n.m.	n.m.	n.m.	n.m.	n.c.	n.c.	n.c.	0.3	7.2	0.41
S37	n.m.	n.m.	n.m.	n.m.	n.m.	n.c.	n.c.	n.c.	n.c.	6.9	n.c.
S46	-10.20	n.m.	n.m.	n.m.	n.m.	n.c.	n.c.	n.c.	0.6	3.8	n.c.

N°	**$\delta^{13}C_{DIC}$ (‰ ± 0.01)**	**$\delta^{18}O_{H2O}$ (‰ ± 0.5)**	**$\delta^{2}H_{H2O}$ (‰ ± 0.05)**	**$\delta^{18}O_{SO4}$ (‰ ± 0.3)**	**$\delta^{34}S_{SO4}$ (‰ ± 0.2)**	**F_{soil} (± 0.1)**	**F_{H-I} (± 0.1)**	**F_{H-II} (± 0.1)**	**FC_{magma} (±0.1)**	**CBE (%)**	**C_m:S_m**
S52	n.m.	n.m.	n.m.	n.m.	n.m.	n.c.	n.c.	n.c.	n.c.	0.1	n.c.
S53	n.m.	n.m.	n.m.	n.m.	n.m.	n.c.	n.c.	n.c.	n.c.	0.8	n.c.
S54	n.m.	n.m.	n.m.	n.m.	n.m.	n.c.	n.c.	n.c.	n.c.	3.3	n.c.
S55	n.m.	n.m.	n.m.	n.m.	n.m.	n.c.	n.c.	n.c.	n.c.	2.2	n.c.
S07	-14.00	n.m.	n.m.	n.m.	n.m.	n.c.	n.c.	n.c.	0.4	0.2	n.c.
S08	n.m.	n.m.	n.m.	n.m.	n.m.	n.c.	n.c.	n.c.	n.c.	3.9	n.c.
S16	-15.41	n.m.	n.m.	n.m.	n.m.	n.c.	n.c.	n.c.	0.3	0.1	0.40
S19	-10.14	n.m.	n.m.	n.m.	n.m.	n.c.	n.c.	n.c.	0.6	0.0	n.c.
S37	-12.91	n.m.	n.m.	n.m.	n.m.	n.c.	n.c.	n.c.	0.5	1.8	n.c.
S38	-15.52	n.m.	n.m.	n.m.	n.m.	n.c.	n.c.	n.c.	0.3	0.0	2.89
S39	-16.03	n.m.	n.m.	n.m.	n.m.	n.c.	n.c.	n.c.	0.2	1.1	n.c.
S40	-16.08	n.m.	n.m.	n.m.	n.m.	n.c.	n.c.	n.c.	0.2	0.5	1.21
S44	-12.64	n.m.	n.m.	n.m.	n.m.	n.c.	n.c.	n.c.	0.5	0.4	n.c.
S45	-16.48	n.m.	n.m.	n.m.	n.m.	n.c.	n.c.	n.c.	0.2	10.3	0.21
S46	-11.54	n.m.	n.m.	n.m.	n.m.	n.c.	n.c.	n.c.	0.5	1.1	28.98
S47	-13.91	n.m.	n.m.	n.m.	n.m.	n.c.	n.c.	n.c.	0.4	1.9	n.c.
S48	-17.32	n.m.	n.m.	n.m.	n.m.	n.c.	n.c.	n.c.	0.1	1.4	0.41
S50	-4.77	n.m.	n.m.	n.m.	n.m.	n.c.	n.c.	n.c.	1.0	3.6	n.c.
S50	n.m.	n.m.	n.m.	n.m.	n.m.	n.c.	n.c.	n.c.	n.c.	100.0	n.c.
S51	-1.02	n.m.	n.m.	n.m.	n.m.	n.c.	n.c.	n.c.	1.0	0.3	1.00
S52	-6.82	n.m.	n.m.	13.5	17.5	0	0	1	0.9	16.4	0.88
S55	-8.02	n.m.	n.m.	n.m.	n.m.	n.c.	n.c.	n.c.	0.8	3.1	n.c.
S56	-10.90	n.m.	n.m.	n.m.	n.m.	n.c.	n.c.	n.c.	0.6	2.5	0.81
S57	-10.43	n.m.	n.m.	n.m.	n.m.	n.c.	n.c.	n.c.	0.6	0.2	1.18
S58	-13.49	n.m.	n.m.	n.m.	n.m.	n.c.	n.c.	n.c.	0.4	0.5	n.c.
S59	-13.63	n.m.	n.m.	n.m.	n.m.	n.c.	n.c.	n.c.	0.4	3.4	n.c.
S60	-7.52	n.m.	n.m.	n.m.	n.m.	n.c.	n.c.	n.c.	0.8	3.1	n.c.
S61	-5.85	n.m.	n.m.	n.m.	n.m.	n.c.	n.c.	n.c.	0.9	2.7	n.c.
S62	-6.22	n.m.	n.m.	n.m.	n.m.	n.c.	n.c.	n.c.	0.9	6.2	n.c.
S63	n.m.	n.m.	n.m.	n.m.	n.m.	n.c.	n.c.	n.c.	n.c.	2.9	n.c.
R1A	n.m.	n.m.	n.m.	n.m.	n.m.	n.c.	n.c.	n.c.	n.c.	31.5	n.c.
R1B	n.m.	n.m.	n.m.	n.m.	n.m.	n.c.	n.c.	n.c.	n.c.	n.c.	n.c.
R2A	n.m.	n.m.	n.m.	n.m.	n.m.	n.c.	n.c.	n.c.	n.c.	n.c.	n.c.
R2B	n.m.	n.m.	n.m.	n.m.	n.m.	n.c.	n.c.	n.c.	n.c.	n.c.	n.c.
R2C	n.m.	n.m.	n.m.	n.m.	n.m.	n.c.	n.c.	n.c.	n.c.	n.c.	n.c.

n.m. not measured.
n.c. not calculated.

Table A.4. Concentration of trace elements by ICP-MS for water samples in Aso caldera.

N°	Sc (nM ± 1)	V (nM ± 5)	Cr (nM ± 0.2)	Mn (nM ± 5)	Fe (nM ± 5)	Co (nM ± 0.2)	Ni (nM ± 0.2)	Cu (nM ± 0.2)	Zn (nM ± 0.2)	As (nM ± 0.1)	Se (nM ± 0.1)	Sr (nM ± 0.1)	Al (nM ± 10)
S01	14	36	0.7	8288	9838	44.2	13.5	18.5	24.9	4.0	7.2	1665.4	3179
S02	99	69	0.3	2475	66	14.2	0.3	11.3	8.7	14.7	4.8	168.9	444
S03	666	53	8.7	3879	2636	43.9	27.9	669.8	325.9	19.2	11.3	1389.6	111369
S04	193	263	0.6	172	347	16.2	1.4	2.4	7.0	1.2	19.0	1386.9	4864
S05	164	199	0.4	487	279	2.2	1.7	6.5	53.3	5.9	14.9	1296.4	3645
S06	1385	236	0.4	4	45	13.3	0.9	12.5	7.6	3.9	10.0	122.4	250
S07	1443	33	1.0	2	n.m.	15.2	0.9	2.8	71.2	8.2	2.9	1264.8	295
S08	1995	1	0.2	11374	673	125.3	18.7	58.4	191.6	1.3	13.4	2781.8	232943
S09	1466	37	1.7	85	5	15.6	27.0	1.3	149.2	7.7	18.1	1282.4	3554
S10	147	316	0.4	88	4	13.6	0.6	6.0	65.0	7.5	24.5	1144.4	1859
S11	1133	126	0.4	38	35	7.5	2.4	4.0	33.3	4.5	1.4	856.5	997
S12	1642	137	0.4	5	22	3.0	1.0	6.7	52.1	3.2	8.9	1262.0	521
S13	1396	223	0.2	9	47	17.2	0.5	16.5	67.3	6.5	15.6	1369.8	8
S14	15	274	0.3	35	-3	12.9	0.2	1.5	52.6	6.9	15.9	1253.5	2393
S15	875	124	0.6	54	42	7.6	n.m.	5.7	27.9	3.4	4.9	712.6	382
S16	1292	149	0.8	1	13	8.9	n.m.	1.9	25.9	3.9	0.9	1194.8	522
S17	123	144	0.8	32	36	8.5	0.1	7.1	145.9	3.4	2.6	113.6	122
S18	377	13	0.1	2	17	2.6	n.m.	1.2	1.9	0.3	n.m.	299.5	3827
S19	157	193	0.7	1	11	1.6	n.m.	2.4	37.0	14.8	18.7	911.4	1979
S20	1389	160	0.6	2	28	1.3	1.0	8.9	35.3	6.9	9.8	98.3	821
S21	2853	233	19.7	7678	45346	19.7	4.9	91.2	177.7	4.3	4.7	1959.9	277199
S22	1394	75	0.6	64	10	9.9	0.3	2.3	15.9	3.7	6.3	977.8	1647
S23	127	164	0.6	40	25	1.8	0.5	3.0	38.7	13.5	7.5	15.5	1382
S24	18	35	0.3	729	58	7.3	1.3	6.3	9.1	4.3	1.7	859.1	888
S25	1291	17	0.5	1338	190	14.5	0.9	3.3	21.1	5.6	6.5	149.9	3946
S26	1274	87	1.0	83	43	7.4	0.1	6.0	2.5	8.5	1.4	935.6	1729
S27	948	185	0.7	186	323	19.1	2.6	1.6	39.8	9.3	15.8	1499.9	2539
S28	1265	6	0.5	4543	4235	53.4	6.3	5.5	468.8	4.2	3.7	3117.5	2938
S29	1214	63	0.2	2569	75	45.4	4.6	26.2	23.9	3.4	12.3	363.3	493
S30	1241	154	0.4	563	158	13.2	0.9	8.8	46.8	7.4	3.6	126.8	139
S31	86	37	1.7	10	23	3.7	0.3	3.6	11.7	2.8	0.2	523.5	752
S32	727	35	1.2	552	149	5.2	0.8	9.3	135.6	3.8	0.7	5.4	856
S33	1258	120	0.4	175	54	13.7	2.0	1.1	78.6	19.8	6.8	1281.4	218
S34	147	157	0.4	1266	294	18.3	1.8	34.6	165.1	17.8	9.8	1821.8	823
S35	1426	84	0.3	886	126	2.3	1.7	2.6	34.5	4.9	8.5	1855.8	4889
S36	1356	14	0.3	712	187	1.5	0.7	33.5	55.0	9.0	6.6	1148.3	34
S01	182	89	0.2	2916	1154	14.6	2.0	4.2	29.5	5.0	5.3	1457.0	729
S02	148	89	1.5	3819	829	17.4	1.2	93.3	138.0	21.9	5.6	1344.5	986
S03	1161	4	2.0	288	170	55.3	29.4	416.5	195.9	3.4	15.5	2126.7	15286
S03	n.m.	n.m.	n.m.	n.m.	n.m.	n.m.	n.m.	n.m.	n.m.	n.m.	n.m.	n.m.	n.m.
S04	948	187	0.5	363	1925	14.8	3.1	72.2	135.0	8.8	19.1	14.5	517
S05	1543	198	0.4	589	486	17.5	1.2	58.3	259.4	7.5	14.0	132.5	574

Appendix

N°	Sc (nM ± 1)	V (nM ± 5)	Cr (nM ± 0.2)	Mn (nM ± 5)	Fe (nM ± 5)	Co (nM ± 0.2)	Ni (nM ± 0.2)	Cu (nM ± 0.2)	Zn (nM ± 0.2)	As (nM ± 0.1)	Se (nM ± 0.1)	Sr (nM ± 0.1)	Al (nM ± 10)
S06	1312	239	0.3	272	232	12.4	0.8	45.3	111.9	2.8	4.7	123.4	170
S07	1352	339	0.5	2	1	11.8	1.9	53.7	78.3	7.4	22.2	117.9	164
S08	1628	7	0.9	8764	686	1.4	19.3	281.9	1859.4	1.6	18.2	2179.8	152285
S09	1389	286	0.3	738	173	18.6	1.8	38.0	216.2	7.2	24.2	1323.7	35
S10	132	35	0.4	62	1	11.9	4.3	47.4	77.1	4.5	23.2	1224.2	457
S11	168	128	0.4	67	242	6.9	1.4	27.0	22.0	4.7	1.0	85.0	18
S11	n.m.	n.m.	n.m.	n.m.	n.m.	n.m.	n.m.	n.m.	n.m.	n.m.	n.m.	n.m.	n.m.
S12	148	253	0.3	168	170	13.9	0.4	25.7	232.2	6.9	15.8	1276.2	442
S13	134	29	0.3	36	529	14.4	0.9	6.3	359.6	6.3	26.3	1325.6	1214
S14	1275	26	0.4	139	145	2.0	0.6	79.3	236.5	7.7	12.4	122.5	911
S15	1186	200	0.6	99	186	9.6	0.9	43.5	226.4	5.5	6.2	18.6	864
S15	1184	199	1.7	160	225	1.4	2.0	47.1	66.4	6.0	8.3	15.7	149
S16	1152	154	0.9	82	13	8.3	0.8	46.2	55.3	3.4	2.4	115.2	1290
S17	192	155	0.5	64	199	8.2	6.2	58.8	26.5	4.2	2.0	145.5	217
S19	1426	24	0.5	8	23	9.1	0.2	4.2	55.7	15.0	17.0	93.3	559
S20	1380	168	1.4	1352	85	11.2	1.4	36.3	211.3	8.4	11.2	948.2	1991
S21	n.m.	n.m.	n.m.	n.m.	n.m.	n.m.	n.m.	n.m.	n.m.	n.m.	n.m.	n.m.	n.m.
S21	2260	212	14.2	5659	4300	3.0	6.8	31.4	253.6	4.3	16.6	1745.7	15497
S22	1382	88	2.0	133	1525	1.2	1.5	25.4	149.8	5.9	7.5	98.6	465
S23	123	164	0.3	236	533	9.9	0.2	12.7	7.2	21.6	6.8	18.6	134
S24	153	72	0.9	2745	6112	9.6	2.6	53.8	378.4	6.5	1.2	917.4	166
S25	1178	98	0.6	2130	5683	13.1	2.8	58.7	155.3	5.6	5.2	1319.4	327
S26	117	83	0.4	1424	1335	10.0	3.5	41.3	226.2	8.0	0.1	991.1	834
S27	115	155	0.5	395	3780	16.8	2.2	82.4	23.9	8.3	15.5	1464.6	896
S28	1248	14	0.7	3735	15758	48.6	9.2	181.9	365.9	5.0	9.8	335.4	235
S29	124	16	0.4	1485	1400	34.3	2.4	22.2	15.3	3.5	17.4	399.2	884
S30	1185	149	0.4	461	1559	1.6	1.0	37.9	38.3	9.0	9.9	1225.4	385
S31	899	54	0.5	16	90	3.7	0.2	51.1	29.6	3.6	0.5	61.3	152
S32	878	48	0.3	26	1238	4.6	0.6	38.6	245.8	4.4	1.2	69.2	960
S33	1285	157	0.7	55	567	12.0	0.6	56.8	142.3	26.8	8.9	1313.8	1143
S34	122	191	1.4	447	694	17.2	2.2	19.4	169.6	19.9	11.5	1977.3	1222
S35	1160	116	0.4	2749	228	17.9	1.9	5.7	49.5	8.2	1.8	1718.8	911
S36	125	137	0.6	50	168	8.9	1.4	86.9	59.6	1.6	4.0	161.6	84
S37	1497	33	1.2	60	117	16.4	0.8	52.0	95.6	1.3	23.5	1276.7	994
S38	1365	332	0.7	3	35	12.9	0.5	71.5	99.5	1.6	24.3	1216.2	10
S39	1565	200	1.2	3	5	9.5	0.4	42.1	53.4	1.2	16.2	114.3	581
S40	1568	198	1.3	7	32	9.9	0.4	58.4	62.4	25.4	13.5	121.2	199
S41	147	188	0.6	9	72	9.0	1.8	95.6	75.5	47.2	13.8	12.9	662
S42	422	5	0.1	14470	13914	56.1	3.2	36.6	5.7	31.8	0.7	8562.2	483
S43	148	78	3.4	489	15268	9.7	2.5	72.8	76.5	3.2	7.4	121.3	1752
S44	717	28	0.4	3	29	4.0	1.7	37.8	41.9	1.3	1.5	636.3	84
S45	189	97	1.2	1	123	4.5	0.4	29.2	36.8	7.6	1.4	796.3	363
S46	132	322	0.4	6	38	13.1	0.9	57.6	96.2	1.1	27.3	1685.9	382

Appendix

N°	Sc (nM ± 1)	V (nM ± 5)	Cr (nM ± 0.2)	Mn (nM ± 5)	Fe (nM ± 5)	Co (nM ± 0.2)	Ni (nM ± 0.2)	Cu (nM ± 0.2)	Zn (nM ± 0.2)	As (nM ± 0.1)	Se (nM ± 0.1)	Sr (nM ± 0.1)	Al (nM ± 10)
S47	12	85	0.7	10	33	4.7	2.1	47.2	47.2	9.2	0.7	673.8	392
S48	783	317	0.5	3	36	5.2	0.3	39.4	64.3	5.5	1.4	687.7	493
S49	356	178	6.5	14844	45452	27.2	7.7	125.9	355.7	3.6	13.2	2931.5	388651
S49	379	6	2.3	2156	718	23.7	0.8	71.5	77.8	1.9	4.4	3126.2	2683
S01	1234	35	1.0	6938	93	77.5	6.8	21.7	318.4	4.2	11.7	1987.9	861
S01	48	18	1.0	635	35	51.8	41.7	15.9	1464.2	2.6	7.9	1454.9	526
S02	15	56	1.8	14	640	1.3	0.5	6.0	159.5	7.0	n.m.	461.4	27
S03	89	3	1.5	7746	274	31.4	65.6	1372.1	338.3	7.2	29.2	539.5	521158
S04	932	59	0.6	137	18	28.7	0.9	13.8	3.6	14.6	22.0	139.3	544
S05	436	112	0.5	624	82	3.4	1.3	9.4	34.5	4.9	9.2	1122.0	186
S06	n.m.	n.m.	n.m.	n.m.	n.m.	n.m.	n.m.	n.m.	n.m.	n.m.	n.m.	n.m.	n.m.
S07	1637	320	1.2	2	0	28.9	2.8	5.0	47.8	7.8	18.3	1387.6	29
S08	244	2	1.5	1177	2237	229.2	25.3	29.9	223.6	3.0	23.5	249.8	178831
S09	n.m.	n.m.	n.m.	n.m.	n.m.	n.m.	n.m.	n.m.	n.m.	n.m.	n.m.	n.m.	n.m.
S10	449	235	0.8	55	3	29.4	1.4	2.2	42.7	7.6	19.0	1321.9	75
S11	587	131	1.9	2	26	12.6	0.5	6.0	25.9	5.5	1.9	74.0	18
S12	364	87	0.5	23	42	39.4	0.2	7.4	37.5	3.5	15.4	1215.0	39
S13	260	133	0.4	44	56	25.0	1.4	11.5	35.6	3.9	18.9	933.5	447
S14	55	222	0.6	256	23	23.2	1.6	11.2	4.8	6.2	1.8	193.9	69
S15	28	113	0.5	8	4	12.3	0.3	5.8	62.2	3.8	1.6	635.2	33
S16	149	142	3.3	3	134	16.4	1.7	15.4	26.5	4.0	1.9	1157.8	195
S17	133	143	1.2	7	45	16.2	0.7	38.9	58.0	3.4	2.7	137.5	347
S18	54	14	0.9	3	24	6.2	0.7	1.6	23.7	0.5	n.m.	395.2	237
S19	162	12	0.8	8	19	17.8	0.9	15.8	197.8	14.4	12.9	767.3	18
S20	n.m.	n.m.	n.m.	n.m.	n.m.	n.m.	n.m.	n.m.	n.m.	n.m.	n.m.	n.m.	n.m.
S21	n.m.	n.m.	n.m.	n.m.	n.m.	n.m.	n.m.	n.m.	n.m.	n.m.	n.m.	n.m.	n.m.
S22	636	54	0.6	24	93	18.3	1.3	13.3	57.6	3.7	5.7	974.8	255
S23	811	126	0.6	344	68	21.9	1.3	11.3	25.1	25.0	3.3	138.2	184
S23	341	116	0.7	112	63	14.3	3.0	16.5	19.2	14.8	3.3	641.5	113
S24	539	53	0.4	216	134	14.7	0.7	12.6	9.5	4.5	1.2	85.8	47
S25	1176	76	1.7	7	22	27.0	3.3	17.4	8.9	3.8	2.3	143.9	450
S26	1215	66	1.2	9	95	16.8	1.2	11.8	18.8	4.4	1.0	998.3	231
S27	399	82	0.5	1875	84	33.3	2.5	17.7	16.5	9.6	19.7	1378.5	939
S28	52	82	0.7	3854	1241	15.9	5.0	28.8	23.5	6.0	2.6	4643.4	74
S29	122	53	1.3	184	214	69.4	6.5	16.9	96.9	2.6	1.4	3631.1	927
S30	1214	14	0.9	68	56	24.8	1.6	5.4	19.2	4.4	1.5	145.5	279
S31	1126	44	1.7	15	22	8.4	1.2	6.9	3.9	3.9	0.9	648.7	500
S32	954	73	1.6	999	248	15.6	2.1	15.7	257.6	4.2	3.4	8.6	423
S33	1323	112	0.9	651	147	27.2	2.4	11.2	144.3	23.2	4.7	1319.3	368
S34	178	133	1.0	137	39	32.2	1.2	12.4	64.0	21.4	1.6	2136.6	225
S35	1128	56	0.8	22	45	39.9	0.8	15.4	1.9	3.7	7.2	1929.2	426
S36	1371	8	0.7	115	452	18.4	1.9	18.4	79.6	8.3	2.6	975.4	274
S37	1767	35	1.8	8	1	39.0	1.3	9.7	63.7	9.4	15.3	1356.4	189

Appendix

N°	**Sc (nM ± 1)**	**V (nM ± 5)**	**Cr (nM ± 0.2)**	**Mn (nM ± 5)**	**Fe (nM ± 5)**	**Co (nM ± 0.2)**	**Ni (nM ± 0.2)**	**Cu (nM ± 0.2)**	**Zn (nM ± 0.2)**	**As (nM ± 0.1)**	**Se (nM ± 0.1)**	**Sr (nM ± 0.1)**	**Al (nM ± 10)**
S38	1688	284	1.2	4	4	34.2	2.8	29.6	64.3	11.8	19.8	1261.3	134
S39	1871	179	1.6	11	1	25.6	0.9	6.9	77.2	1.8	13.9	1239.4	16
S40	1896	186	1.5	85	48	25.4	0.6	4.6	58.1	32.2	18.7	1263.6	19
S41	1769	172	1.0	3	1	25.6	0.8	15.0	26.7	53.9	1.9	1162.3	10
S42	48	1	1.5	174	953	97.4	1.7	9.7	39.3	24.7	1.0	752.5	44
S43	1883	1434	38.7	4762	24256	68.9	25.3	73.6	661.4	9.7	n.m.	2177.8	141146
S44	882	20	0.6	1	5	7.5	0.3	5.2	9.3	1.1	n.m.	69.4	45
S45	448	82	0.9	123	68	1.4	0.3	4.2	13.8	7.3	2.6	828.8	44
S46	58	244	1.0	50	3	38.2	0.7	21.6	32.5	12.0	27.0	1752.6	26
S47	400	4	0.4	16	4	13.0	0.7	16.4	38.4	5.7	1.8	736.2	17
S48	1218	76	1.2	17	34	1.6	0.3	2.9	22.5	9.0	0.2	715.7	141
S49	177	15	6.4	1347	24398	33.8	4.7	29.5	264.0	1.1	4.8	219.6	259121
S49	269	7	0.7	15982	52	39.4	0.9	2.4	1.5	0.8	n.m.	247.6	57
S01	0	37	0.4	1	1	0.5	0.2	3.8	4.2	2.6	1.4	131.8	19
S01	n.m.	n.m.	n.m.	n.m.	n.m.	n.m.	n.m.	n.m.	n.m.	n.m.	n.m.	n.m.	n.m.
S01	n.m.	n.m.	n.m.	n.m.	n.m.	n.m.	n.m.	n.m.	n.m.	n.m.	n.m.	n.m.	n.m.
S03	0	0	0.9	1133	26	2.7	13.9	367.9	3166.9	2.2	8.6	1288.7	88653
S04	0	67	0.1	66	2	0.2	1.1	6.6	24.2	2.9	7.0	143.6	13
S07	0	235	0.5	1	n.m.	n.m.	0.5	1.1	452.7	5.8	18.6	921.7	4
S19	0	148	0.6	n.m.	n.m.	n.m.	0.5	1.0	224.2	11.2	1.7	716.5	n.m.
S22	0	58	0.4	0	70	0.3	1.0	5.2	39.3	2.8	4.7	719.3	534
S23	0	89	0.4	170	48	0.4	1.1	3.7	325.9	12.8	3.6	762.5	52
S27	0	92	0.3	2	8	0.3	0.5	2.3	1.6	5.9	17.6	159.6	17
S28	0	20	0.3	1	11	0.2	1.4	7.5	12.8	4.3	9.7	228.5	2
S29	0	43	0.5	5	7	0.4	1.8	11.5	83.7	3.2	7.5	278.6	3
S30	0	75	0.3	1	35	0.2	6.6	4.6	5.4	4.5	5.4	944.0	45
S33	0	65	0.6	4	n.m.	0.2	1.3	3.6	345.0	12.3	5.2	883.3	56
S34	0	157	0.5	1	n.m.	0.1	0.9	5.0	289.5	8.3	1.4	778.9	34
S35	0	52	0.2	1495	26	0.4	1.6	5.0	248.2	3.2	5.2	13.8	73
S36	0	65	0.4	2	17	0.1	1.4	8.0	14.5	6.4	n.m.	738.9	26
S46	0	239	0.5	5	17	1.0	0.5	1.2	178.5	8.2	18.6	1262.5	19
S03	n.m.	n.m.	n.m.	n.m.	n.m.	n.m.	n.m.	n.m.	n.m.	n.m.	n.m.	n.m.	n.m.
S18	n.m.	n.m.	n.m.	n.m.	n.m.	n.m.	n.m.	n.m.	n.m.	n.m.	n.m.	n.m.	n.m.
S50	1	6	0.2	22	16	0.4	1.5	0.5	n.m.	2.5	0.8	6864.8	238
S51	2	36	0.3	7429	n.m.	25.5	28.9	25.9	6.3	19.8	2.1	1697.7	1182
S01	0	42	0.3	41	33	0.3	0.7	6.4	2.9	6.0	6.8	14.0	89
S07	1	362	0.7	1	n.m.	0.8	0.4	1.2	62.5	8.3	36.9	1251.9	62
S23	1	133	0.5	5	55	1.0	0.3	3.8	n.m.	12.5	9.4	13.3	268
S28	0	3	0.2	1176	71	64.6	14.4	8.7	32.5	2.9	11.7	275.9	21
S37	1	355	0.5	1	n.m.	0.3	0.5	1.2	19.3	5.1	27.8	142.4	57
S46	1	333	0.6	2	n.m.	0.2	0.9	4.6	n.m.	9.8	29.6	166.1	43
S52	1	1	0.8	8529	6377	0.2	1.5	1.5	n.m.	0.6	n.m.	1442.4	28
S53	0	0	0.6	4339	12	15.8	8.7	13.3	27.2	1.3	1.7	541.5	86

Appendix

N°	Sc (nM ± 1)	V (nM ± 5)	Cr (nM ± 0.2)	Mn (nM ± 5)	Fe (nM ± 5)	Co (nM ± 0.2)	Ni (nM ± 0.2)	Cu (nM ± 0.2)	Zn (nM ± 0.2)	As (nM ± 0.1)	Se (nM ± 0.1)	Sr (nM ± 0.1)	Al (nM ± 10)
S54	0	4	0.4	164	313	1.5	4.7	8.8	28.3	1.7	6.6	1331.3	72
S55	1	1	0.5	3576	2243	0.2	0.9	3.7	17.3	332.9	0.2	183.8	147
S07	1	36	0.6	2	14	0.9	1.4	4.3	29.2	8.7	33.7	1266.7	48
S08	6	1	0.7	128	725	63.1	24.7	152.6	339.9	1.6	16.5	2486.4	152975
S16	1	159	0.9	2	9	0.5	1.0	3.1	17.5	3.6	0.6	124.4	46
S19	1	23	0.3	5	14	0.6	0.8	1.9	33.2	14.5	24.2	917.5	36
S37	1	348	0.9	0	16	0.5	1.5	1.5	33.0	1.2	n.m.	1111.4	149
S38	1	292	1.4	13	119	0.1	0.9	1.5	65.8	8.6	22.4	1225.3	26
S39	1	28	0.9	1	9	0.7	0.2	1.6	9.3	2.0	15.9	165.6	17
S40	1	29	0.9	62	1	1.0	0.5	2.7	14.8	23.3	12.8	175.1	27
S44	0	22	0.4	1	14	1.0	1.5	2.8	11.8	0.9	n.m.	593.6	316
S45	1	19	1.4	0	13	0.4	0.3	1.4	8.9	8.8	0.1	82.3	46
S46	1	336	0.4	0	12	0.6	1.2	3.2	29.6	11.3	29.6	1618.7	13
S47	0	349	0.4	1	6	0.1	0.8	3.8	9.8	6.7	18.1	751.5	69
S48	1	83	0.6	1	10	0.3	0.1	0.7	8.5	9.2	0.5	71.8	8
S50	2	1	n.m.	120	52	0.4	2.2	1.5	1.2	1.9	n.m.	7938.9	n.m.
S50	n.m.	n.m.	n.m.	n.m.	n.m.	n.m.	n.m.	n.m.	n.m.	n.m.	n.m.	n.m.	n.m.
S51	1	176	0.7	5264	9	3.7	13.7	12.5	3.8	15.4	1.0	1486.7	117
S52	1	0	n.m.	875	84	0.3	0.7	0.8	1.8	0.2	n.m.	1449.1	n.m.
S55	1	1	n.m.	3685	2595	0.2	0.7	3.0	3.3	343.4	n.m.	1769.8	70
S56	1	30	0.9	7	19	0.8	0.9	1.5	24.7	4.2	13.5	162.9	338
S57	1	35	0.2	1	19	0.5	1.5	2.4	32.9	11.9	24.9	2139.1	53
S58	1	344	0.3	2	14	0.1	1.8	7.9	35.2	8.6	n.m.	1624.4	25
S59	1	353	0.3	0	12	0.1	0.7	3.7	20.0	9.3	28.3	1719.6	1
S60	1	113	0.9	1	16	0.2	0.5	1.2	1.3	145.8	n.m.	274.1	3
S61	2	1	n.m.	139	6126	1.0	0.9	1.4	26.7	1232.6	n.m.	237.6	128
S62	2	1	n.m.	747	112	0.4	4.4	61.5	55.7	82.8	n.m.	1754.7	n.m.
S63	1	112	n.m.	70	29	0.9	3.4	0.8	124.9	94.6	16.8	1848.8	0
R1A	n.m.	2	0.2	73	n.m.	0.4	1.8	3.9	34.3	2.6	n.m.	5.9	24
R1B	n.m.	0	0.8	6	n.m.	0.1	2.4	2.9	9.7	0.7	0.2	0.9	30
R2A	n.m.	4	3.6	3	n.m.	1.2	16.9	46.2	47.5	0.4	n.m.	13.7	154
R2B	n.m.	5	2.5	11	n.m.	0.9	14.8	36.3	351.7	0.4	0.9	12.4	138
R2C	n.m.	1	0.4	15	36	0.3	3.6	13.8	47.4	0.3	0.7	6.3	552

n.m. not measured.

Appendix E. Author's individual contribution to publications

The contribution to each publication is stated below. However, it is imperative to understand that each author has contributed in the development of each publication. The weight of the sections listed in author's contribution was usually shared with more than one co-author.

Romero-Mujalli, G., Hartmann, J., Börker, J., Gaillardet, J. & Calmels, D., 2018. Ecosystem controlled soil-rock pCO_2 and carbonate weathering – Constraints by temperature and soil water content. Chemical Geology. Author's contribution: Idea, data acquisition, methodology, results and discussion.

Romero-Mujalli, G., Hartmann, J. & Börker, J., 2018. Temperature and CO_2 dependency of global carbonate weathering fluxes – Implications for future carbonate weathering research. Chemical Geology. Author's contribution: Idea, methodology, results and discussion.

Börker, J., Hartmann, J., Romero-Mujalli, G. & Amann, T., 2018. Terrestrial Sediments of the Earth: Development of a Global Unconsolidated Sediments Map Database (GUM). Geochemistry, Geophysics, Geosystems. Author's contribution: results and discussion.

Gaillardet, J., Calmels, D., Romero-Mujalli, G., Zakharova, E. & Hartmann, J., 2018. Global climate control on carbonate weathering intensity. Chemical Geology. Author's contribution: data acquisition, methodology, results and discussion.

Börker, J., Hartmann, J., Romero-Mujalli, G. & Li, G., 2018. Short Communication: Aging of basalt volcanic systems and decreasing CO_2 consumption by weathering. E-Surf. Author's contribution: methodology, results and discussion.

Romero-Mujalli, G., Hartmann, J., Hosono, T., Amann, T., Louvat, P. and Böttcher, M.E., Evaluating the contribution of high temperature fluids to surface waters using Se:SO_4^{2-} molar ratios for the Aso caldera, Japan: Implications for weathering rates of volcanic areas. Author's contribution: Idea, methodology, results and discussion.

Acknowledgements

I would like to thank all the persons that have been part of my professional and personal development. It would be impossible to name them all in this text because some of them and I were not acquainted. Excuse me if your name is not explicitly mentioned in these acknowledgements.

First, I would like to thank my family and my friends; they gave me their constant support and each step I made is for them. Prof. Dr. Jens Hartmann, thank you for your support and for believing in my scientific criteria. Prof. Dr. Ari Roisenberg, more than a supervisor you were a friend and a second father while I was living in Brazil, *estou com saudade de vocês*. Prof. Dr. Milton Formoso, thank you for sharing with me the secret of a long and prosper life. Williams Meléndez, thank you for your advice and the opportunity to work with mangrove forests. Prof. Dr. Laura Piñero, thank you for the “push” that you gave me to pursue geophysics and to learn programming by myself. Prof. Jhonny Tapia, thank you for teaching me how to be a good scientist, I owe you most of my professional development.

I would like to thank Prof. Dr. Victor Brovkin, Prof. Dr. Jörn Peckmann and Dr. Thorben Amann for being part of my doctoral committee and for their critics to my work, which will help me in my future academic work. Prof. Dr. Lars Kutzbach, thank you for being part of my advisory panel and for your support along my doctoral studies. I would like to thank all the professors in Venezuela, Brazil and Germany that shared their knowledge with me. Special thanks to the School of Integrated Climate System Sciences (SICSS).

Finally, funding for this work has been provided by German Research Foundation (DFG) through the Cluster of Excellence CLISAP2 (DFG Exce177, Universität Hamburg), and BMBF-project PALMOD (Ref. 01LP1506C) through the German Federal Ministry of Education and Research (BMBF) as Research for Sustainability initiative (FONA). Thanks to the editors and all anonymous reviewers for their constructive critics.

Eidesstattliche Versicherung

Hiermit versichere ich an Eides statt, dass ich die vorliegende Dissertation mit dem Titel: „The role of temperature in processes controlling weathering rates of carbonate lithologies and volcanic systems“ selbstständig verfasst und keine anderen als die angegebenen Hilfsmittel – insbesondere keine im Quellenverzeichnis nicht benannten Internet-Quellen – benutzt habe. Alle Stellen, die wörtlich oder sinngemäß aus Veröffentlichungen entnommen wurden, sind als solche kenntlich gemacht. Ich versichere weiterhin, dass ich die Dissertation oder Teile davon vorher weder im In- noch im Ausland in einem anderen Prüfungsverfahren eingereicht habe und die eingereichte schriftliche Fassung der auf dem elektronischen Speichermedium entspricht.

Hamburg, 31.01.2019

Gibran Romero Mujalli